

**Development of Embedded Readout
and
Design Optimization of PIN Diodes for Radiation
Detection**

By
G.PRASANNA
(ENGG02201004014)

Indira Gandhi Centre for Atomic Research, Kalpakkam

*A thesis submitted to the
Board of Studies in Engineering Sciences
In partial fulfillment of requirements
For the Degree of*
DOCTOR OF PHILOSOPHY
Of
HOMI BHABHA NATIONAL INSTITUTE


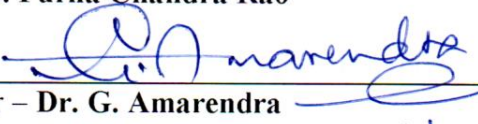
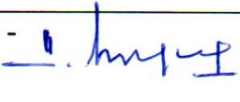

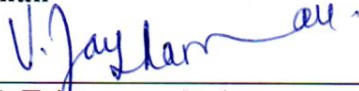



July, 2017

Homi Bhabha National Institute

Recommendations of the Viva Voce Committee

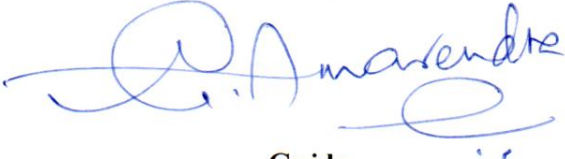
As members of the Viva Voce Committee, we certify that we have read the dissertation prepared by **G. Prasanna** entitled "**Development of Embedded Readout and Design Optimization of PIN diodes for Radiation Detection**" and recommend that it may be accepted as fulfilling the thesis requirement for the award of Degree of Doctor of Philosophy.

 Chairman – Dr. B. Purna Chandra Rao	Date: 7/3/2019
 Guide / Convener – Dr. G. Amarendra	Date: March 7, 2019
Examiner -  Dr. M. UMAPATHY	Date: 7-3-2019
Member 1- Dr. M. Kamruddin 	Date: 07/3/19
Member 2- Dr. V. Jayaraman 	Date: 07/03/2019
Technology Adviser- Dr. S. Tripurasundari 	Date: 7/3/2019

Final approval and acceptance of this thesis is contingent upon the candidate's submission of the final copies of the thesis to HBNI.

I/We hereby certify that I/we have read this thesis prepared under my/our direction and recommend that it may be accepted as fulfilling the thesis requirement.

Date: March 7, 2019
Place: Kalpakam


Guide

STATEMENT BY AUTHOR

This dissertation has been submitted in partial fulfillment of requirements for an advanced degree at Homi Bhabha National Institute (HBNI) and is deposited in the Library to be made available to borrowers under rules of the HBNI.

Brief quotations from this dissertation are allowable without special permission, provided that accurate acknowledgement of source is made. Requests for permission for extended quotation from or reproduction of this manuscript in whole or in part may be granted by the Competent Authority of HBNI when in his or her judgment the proposed use of the material is in the interests of scholarship. In all other instances, however, permission must be obtained from the author.



(G. Prasanna)

DECLARATION

I, hereby declare that the investigation presented in the thesis has been carried out by me.

The work is original and has not been submitted earlier as a whole or in part for a degree / diploma at this or any other Institution / University.



(G. Prasanna)

List of Publications

Journals

1. **G. Prasanna**, & J. Jayapandian, "An Embedded Readout for GM-counter", International Journal of Instrumentation Technology, **2014**, Vol-1, No-3, pp 228-240.
2. **Prasanna Gandhiraj**, Manoj Kumar Parida, Krishnamurthi Prabakar, Raghuramaiah Manchi, Sankaran Tripura Sundari, Jayaseelan Jayapandian & Chakram Sampathkumar Sundar, "Effect of dead layer on the efficiency of planar semiconductor neutron detectors", IETE Technical Review, **2016**, Vol-33, No-1, pp 45-49.
3. **G. Prasanna**, J. Jayapandian, O.K. Sheela, S. Tripurasundari and G. Amarendra, "A low cost portable alpha spectrometer using embedded pulsed reset preamplifier stage", Nuclear Instruments and Methods in Physics Research Section A (Under Review) Jan **2019**.

Conferences

1. **G. Prasanna**, J. Jayapandian, O.K. Sheela & G. Amarendra, "A virtual instrument user interface for multi channel analyzer", presented at **40th National Symposium on Instrumentation (NSI-40)**, held at Kumaraguru College of Technology, Coimbatore, Tamil Nadu, during October 30th and 31st, **2015**.
2. **G. Prasanna**, J. Jayapandian, R. Usharani Ravi & G. Amarendra, "PSoC Based portable high voltage source with programmable ramping control", presented at **40th National Symposium on Instrumentation (NSI-40)**, held at Kumaraguru College of Technology, Coimbatore, Tamil Nadu, during October 30th and 31st, **2015**.
3. **G. Prasanna**, J. Jayapandian, O.K. Sheela & G. Amarendra, "A novel pulse processing scheme using embedded pulsed reset charge sensitive preamplifier", presented at **60th DAE Solid State Physics Symposium**, held at Amity University UP, Noida, Uttar Pradesh, India, during December 21-25, **2015**.


(G. PRASANNA)

...what is the kind of education that science offers to man. It teaches us to be neglectful of nothing, not to despise the *small* beginnings, for they precede of necessity *all great things*...

Michael Faraday

The life and letters of Faraday, (1870), vol 2. P. 403

Dedicated
to my
grandparents,
Shri. P. Venkatarayappa
and
Smt. V. Nagarathna

ACKNOWLEDGEMENTS

Firstly, I would like to express my sincere gratitude to my former technology adviser and mentor Dr. J. Jayapandian former head, EIS, SND, MSG, for being a source of immense motivation, inspiration and encouragement in carrying out my research work.

Besides my mentor, I would like to express my deep sense of gratitude to my research supervisor Dr. G. Amarendra, Chairman of my Doctoral Committee, Dr. B. Purna Chandra Rao, my technology adviser Dr. S. Tripurasundari and members of my doctoral committee; Dr. V. Jayaraman and Dr. M. Kamruddin. Their insightful comments, encouragement and hard questions have incited me to widen my research from various perspectives. I am especially grateful to Dr. S. Tripurasundari for her sincere efforts and patience in going through the entire thesis meticulously.

I am also grateful to my seniors in the laboratory, Dr. K. Prabakar, Smt. O. K. Sheela, Smt. K. Usha Rani, Shri. M. Raghuramaiah for their willingness to share their knowledge and helping me in carrying out experiments. I also thank my lab-mates and fellow research scholars Mr. Manoj Kumar Parida and Mr. S. Balasubramanian for the wonderful time spent in the lab discussing anything from science to sports. I would like to record my sincere thanks to members of EIRSG, IGCAR, particularly Dr. R. Venkatesan and Dr. B. Venkatraman. Special thanks to Dr. S. Kalavathi, Head, HPPS, MSG, for meticulously reviewing the final draft of this thesis.

I express my to Dr. Steven L. Bellinger of Kansas State University for sharing the MATLAB codes used in this work and for the insightful discussions he has had with our group.

I thank Dr. M. Sai Baba for providing me encouragement and support. I am especially grateful to him for the accommodation provided at the enclave during my research tenure.

I sincerely thank the Department of Atomic Energy, India, for providing me necessary financial support throughout my research tenure. I am grateful to Dr. Baldev Raj, former director, IGCAR, for allowing me to carry out my research work in Materials Science Group and also the subsequent directors Shri S. C. Chetal, Dr. P. Vasudeva Rao, Dr. S. A. V. Sathyamurthy. I wish to place on record my sincere gratitude to the Director, IGCAR, Dr. Arun Kumar Bhaduri for allowing me to continue my research work in this esteemed institute.

Special thanks to Mr. Muffazal Badshahwala, Dr. Kalyan Phani Makkuva and Mr. N. S. Baskaran for being accommodating and wonderful room-mates and batch-mates during my stay in the enclave. Last, but not the least, words are insufficient to thank my dear friends at the enclave - Dr. N. Srinivasan, Dr. K. Benadict Rakesh, Mr. M. Thangam, Mr. Naveen Raj, Mr. Hari Prasad. Warm thanks to my batch-mates Dr. Avinash Patsha, Dr. Anbumozhi Angayarkanni, Dr. Bonu Venkatramana, Dr. Devidas. T. Raghavendran, Dr. K. Kamali, Dr. Leona. J. Felicia, Dr. V. Mahendran, Dr. Mahendra Chintala, Smt. Meera A. V., Mr. Nanda Gopan, Dr. Rasmi K. R., Dr. Sadu Venkatesh, and Dr. M. Sabeena.

I take this opportunity to thank my grandparents late Shri. P. Venkatarayappa and Smt. V. Nagarathna for their blessings. I am especially indebted to my loving parents for bestowing me with their unconditional love and encouragement, and for having been there at every step of the journey without which this thesis would not be possible.



(G. Prasanna)

Table of contents:

Synopsis.....*i*

List of figures.....*ix*

List of tables.....*xv*

CHAPTER 1	Portable radiation instruments –trends and scope for design improvements	1
1.1	Radioactivity for mankind	1
1.2	Radiation	2
1.3	Design principles of radiation instruments	4
1.3.1	Charge collection mechanism and detector electronics	4
1.4	Categories of Radiation Instruments	5
1.4.1	Factors affecting design choices for portable instruments	7
1.4.2	Evolution of instrument designs	8
1.5	Motivation for the thesis	11
1.5.1	State-of-the-art gamma survey meters - Limitations	11
1.5.2	Portable alpha spectrometers – State of the art and challenges	13
1.5.3	Planar Neutron detectors and design optimization.	15
1.6	Organization of the thesis	19

CHAPTER 2	PSoC Embedded design for Geiger Mueller survey meter – bias control and readout.....	21
2.1	Introduction.....	21
2.2	PSoC based enhancements inGM counter building blocks.....	22
2.2.1	Regulated HV power supply.....	22
2.2.2	Raw analog pulses from GM tube: input protectioncircuitry using PSoC.....	29
2.2.3	Pulse conditioning, dose rate measurement and user interface.....	34
2.2.4	PSoC Design and programming	35
2.3	Results and discussion	37
2.3.1	System level specifications of the application board	41
2.4	Conclusions.....	42
CHAPTER 3	PSoC Embedded read-out design for PIN diode based portable alpha particle spectrometer	43
3.1	Introduction.....	43
3.2	Overview of the system level modular design	45
3.3	The front-end design.....	45
3.3.1	Detector and its mount.....	46
3.3.2	The detector bias.....	47
3.3.3	The preamplifierdesign.....	49
3.4	Embedded pulsed reset function	52
3.4.1	PSoC- 5 platform features	60
3.4.2	Reset device.....	63

3.4.3 Switch control signal characteristics	65
3.5 PC based User interface	67
3.6 Experimental results	68
3.7 Conclusions.....	73
CHAPTER 4 Design simulations of planar semiconductor neutron detectors.....	75
4.1 Introduction.....	75
4.2 Design evolution of neutron detectors	75
4.2.1 Detector configurations	78
4.3 Motivation for Monte Carlo simulation	80
4.4 Simulation methodology.....	82
4.4.1 The unit cell.....	83
4.4.2 Important assumptions in the simulation model	84
4.4.3 Particle tracking methodology inside the unit cell.....	85
4.4.4 Estimation of $\bar{E}_m^i(X)$ and the $\bar{X}_m^i(E)$ functions.....	88
4.4.5 MATLAB code for particle tracking.....	89
4.4.6 Summary of the simulation methodology.....	91
4.5 Benchmarking simulations in trench detectors	92
4.6 Estimated Efficiencies for planar detectors.....	93
4.6.1 Efficiency variation with respect to the LLD	95
4.7 Effect of dead layer on neutron detector efficiency	96
4.7.1 Introduction	96

4.7.2 MATLAB® code for dead layer simulation	97
4.8 $\bar{E}_m^i(\mathbf{X})$ and $\bar{X}_m^i(\mathbf{E})$ estimation in gold dead layer medium.....	100
4.8.1 Empirical fits for B ¹⁰ and Li ⁶ conversion ions in gold (Au) medium	100
4.8.2 Simulation of detector efficiency.....	104
4.9 Conclusions.....	107
CHAPTER 5 Summary, conclusions and future scope.	108
5.1 Summary	108
5.2 Suggestions for future work.....	109

Appendices:

Appendix A: List of embedded C- Programs.....	108
Appendix B: Mixed signal PSoC platform for auxiliary lab applications.....	115
Bibliography:.....	130

SYNOPSIS

Over a century since the discovery of x-rays and radioactivity in 1895 and 1896, respectively, a wide variety of radiation instruments have been designed, developed and successfully implemented to cater to the application of radioactivity in various fields. The diverse range of instruments are broadly categorized into lab-scale and portable ones based on their design and implementation [1, 2]. Biomedical imagers, radiotherapy monitoring instruments, composite high energy physics detectors, industrial radiography equipments etc., that are permanently installed in nuclear facilities and hospitals to perform high precision, time critical measurements of parameters like energy, intensity and spatial location are classified as lab scale instruments. Area gamma monitors, environmental radioactivity survey meters and portal monitors, which are operated in handheld / remote mode, are classified as portable radiation instruments.

Portable instruments have been in existence from the early days of radiation related instrumentation. The context and motivation for the present thesis can be better drawn by tracing the evolution of instrumentation for radiation applications. From the initial stages when instrument designs used excessive power consuming vacuum tubes, they have graduated through discrete electronics based implementations using transistors to the relatively recent low power microprocessor based platforms. The microprocessor based platforms are characterized by their powerful architecture and higher clock rates in the 100s of MHz range [3]. Though cost effective for lab-scale applications [4], these are expensive design options in the realm of portable radiation instruments which are generally used for gross measurement applications such as environmental contamination survey.

In the recent past, numerous technological advancements have taken place in two important fields, viz. Integrated Circuits (IC) and semiconductor radiation detectors.

Advances in IC technology have led to the development of high performance commercial Operational Amplifiers (Op-Amp) and emergence of numerous reconfigurable mixed signal hardware platforms. They offer generic support for a wide range of applications [5, 6], with shorter development times. Apart from these features, they offer near zero non-recurring costs thereby being competitive and reducing overall cost of the system design [7-9]. This potential is realized when system designs exploit novel semiconductor detectors in addition to the reconfigurable mixed signal platforms and recent Op-Amps.

This provides a motivation to design and implement low cost embedded readout electronics for portable radiation instruments employing the recent components reaping the added benefits like ultra-low power operation, real time data analysis, advanced graphical user interfaces (GUI), micro-miniaturization and long term stability [10].

This thesis describes research carried out in two important aspects of portable radiation instruments namely, implementation of readout electronics using a recent reconfigurable mixed signal hardware platform along with detector design and optimization. The first part of the thesis gives a detailed description of design and implementation of the embedded readout electronics of two portable radiation instruments - a GM counter and an alpha particle spectrometer- using the PSoC platform. The second part of the thesis describes the design optimization of planar semiconductor neutron detectors using Monte Carlo simulations. Auxiliary works related to automation of creation of trenches in substrates for fabrication of neutron detectors, high voltage bias control for an ion mobility spectrometer and a PSoC based hand tremor monitor are also described in this thesis.

This thesis is organized into five chapters and two appendices and the details of each chapter and appendix are summarized below.

Chapter 1 Introduces the historical evolution of radiation detection and measurement, its importance in various areas of science, technology and medicine. The classification of existing radiation instruments in terms of their design implementation, into either lab-scale or portable instruments is discussed. The evolution of portable radiation instruments and their recent implementations [4, 11, 12] with specific attention on their design challenges are listed. The subsequent part of this chapter discusses about the development of novel detectors and some attempts at exploring low cost alternatives in detectors [13, 14] followed by recent advances in the integrated circuits. A detailed description of the recent emergence of various reconfigurable hardware platforms in the embedded systems domain is presented. A brief [15, 16] survey of these platforms along with a representative reconfigurable mixed signal platform –the PSoC platform [17, 18], its capabilities, design methodologies and its limitations are described in detail. The relevance and adaptability of reconfigurable mixed signal platforms in meeting the challenges [19] posed by portable applications are presented. The motivation for the present research is the need for cost effective designs to be employed in portable radiation measurement applications using recent advanced reconfigurable platforms such as PSoC. The chapter concludes with the objectives which the present work hopes to attain in terms of the implementation of embedded readout and design optimization of novel detectors followed by the description of the thesis organization.

Chapter 2 describes the implementation of an embedded design for bias control and readout for Geiger Muller (GM) counter application. As is well known, GM counters are the simplest radiation detectors widely used in the environmental radiation monitoring applications, where the main requirement is gross counting of environmental gamma radiation [20]. The signal generation in the GM tube occurs by Geiger discharge whereby

an avalanche of electron-ion pairs is produced in a gaseous environment when subjected to a high electric field upon radiation interaction. The high electric field is produced at a bias of 500 V. The design and implementation of proportional- integral (PI) high voltage bias controller using on-chip analog modules of the programmable system on chip (PSoC) reconfigurable mixed signal platform, for an external DC-DC boost converter [5] is discussed. Other general functional requirements in a GM counter namely, signal conditioning to convert 25 V analog signal swings from the GM tube to 5V TTL levels for counting, engineering conversions through firmware programming, and communication with a PC through UART are discussed followed by the description of single chip implementation of these functions on the PSoC platform. The details of calibration procedure for GM counters are also discussed. This design achieves a sensitivity of $0.01451 \text{ CPS/nSvh}^{-1}$. This value is comparable to that of commercial systems, establishing its cost effective implementation using the single chip approach for a general portable radiation survey meter application.

Chapter 3 describes the use of commercially available large area planar PIN diodes as low cost alternatives to implement alpha particle spectrometry. PIN diodes have been reported to have performance comparable to that of high quality surface barrier detectors for direct detection of ionizing radiation [21]. They have been explored as low cost alternatives in alpha particle spectroscopy [22]. This chapter describes the design and implementation of a cost effective, portable high energy resolution alpha spectrometer using a modified feedback network at the preamplifier stage. A novel embedded pulsed reset technique utilizing a CMOS analog switch as reset element in the preamplifier feedback with a firmware generated control signal is used for improving the energy resolution. The detailed description of the design and implementation of the charge

sensitive preamplifier and the CMOS analog switch selection are given in this chapter. The special feature of this design is ultimately in the reduction of thermal noise and pile-up event errors using a novel technique. While thermal noise error contribution to the preamplifier output is greatly reduced by the very high open-state resistance ($\sim 7\text{G}\Omega$) of the switch, the pile-up event error contribution are eliminated by running a special sequential circuit (A state machine) in parallel with the digitizer and the firmware. This chapter describes the implementation of both the firmware and the state machine on a single chip reconfigurable mixed signal PSoC platform. The Pulse height digitization and pile up elimination functions are also discussed. In addition to these basic functions this single chip solution also provides compact high voltage bias regulation and ramping functions (0V to 500V) essential for input protection of the preamplifier stage in a portable spectrometry system. The design and implementation of the high voltage ramping subsystem along with the implementation of a PC based virtual instrument graphical user interface developed using National Instruments Lab VIEW to which the digitized pulse heights are communicated is also described in detail. Finally the experimental results obtained for alpha spectrometry with this system are presented. The experimentally observed spectrum using this system for a standard mixed nuclide alpha source shows a resolution of 29.1 KeV FWHM (Full width between half maximum) at the alpha energy peak of 5.155 MeV corresponding to the Plutonium source.

Chapter 4 discusses the design optimization of semiconductor neutron detectors in planar configuration using Monte Carlo simulations. A brief introduction to neutron detection followed by recent challenges in neutron detector design is discussed, followed by an introduction to trench structured neutron detectors [23, 24]. These detectors are a

promising low cost, low power and rugged alternative for the conventional He-3 gas filled proportional counters in neutron detection. Currently various alternative designs of trench structured detectors are being explored [25-27]. The simulation methodology known as the Shultis-Mc-Gregor methodology originally developed for three dimensional straight trench patterned detectors is described in detail. Preliminary benchmarking simulations for efficiency estimation on trench pattern detectors and the results with two types of converter materials, boron-10 and Li^6F , in terms of determination of intrinsic neutron detection efficiency variation with converter material dimensions and low level discrimination (LLD) energy are described.

The adaptation of the trench detector code for the planar detector [28-30] case is described in detail. Further, simulation results for determination of the converter material thickness for maximum intrinsic neutron detection efficiency are discussed. An optimum converter thickness of 2.5 μm and 25 μm for boron-10 and Li^6F converter material respectively have been observed for a maximum intrinsic neutron detection efficiency of 4% in both the cases. The variation in intrinsic neutron detection efficiency with the thickness of a gold dead layer is also simulated using the modified code. A decrease in efficiency from 4% to 3% was observed when a dead layer of 1 μm thickness is introduced near the top of the detector. The description of the code for the inclusion of the dead layer is given for both boron-10 and Li^6F converter materials in this chapter.

Chapter 5 provides a brief summary of the work presented in this thesis with suggestions for future directions.

Appendices

Appendix A Lists out two embedded C programs used in this work.

Appendix A.1 Lists the C program used in the GM counter application

Appendix A.2 Lists the C program used in the alpha spectrometer application.

Appendix B discusses auxiliary lab applications developed using the PSoC platform

Appendix B.1 describes the implementation of an X-Y table control system for creating straight trench patterns in substrates using the PSoC platform. As a part of fabrication study for neutron detectors there was a necessity for creating straight trench patterns on silicon substrates using direct laser ablation technique. To automate the process for creating straight trench patterns with varying width between lines and various side lengths an X-Y table control system based on the PSoC platform was developed and successfully implemented. A PC based user interface was developed in LabVIEW with an USB interface for PSoC drive module. This appendix describes the detailed implementation of the PSoC design and the LabVIEW GUI design.

Appendix B.2 describes a compact high voltage system with pulsing control for an ion mobility spectrometer. The ion mobility spectrometer is used in chemical detection applications that require high selectivity. The gate electrode in an Ion mobility spectrometer is required to be biased in a pulsed fashion using a high voltage of -3.5KV which momentarily should rise to -3KV and should remain at this value for ~1.5 ms. The rise time requirement is that it should be less than 100 μ s. Various existing design options for pulsed HV operation were studied and were found to fall short of either the requirement in rise time characteristics or in HV level. A compact HV pulsing system using commercially available regulated 3.5 KV HV module and a PSoC based pulsing

system was implemented. This appendix describes the detailed design and implementation of this system.

Appendix B.3 describes the design and implementation of an electronic hand tremor monitoring system to assist in diagnosis and treatment of Parkinson's disease. The system consists of two sub systems- a handheld, wireless-enabled electronic glove and a PC based user interface for data acquisition. The electronic glove sub-system consists of a MEMS based 3-axis accelerometer sensor, a PSoC based application board and a 2.4 GHz ISM band Zigbee RF transceiver. All the modules are mounted on an ordinary hand glove. The interface to the PC is done through the RS-232 port. The data from the handheld glove is received through another ZigBee wireless module connected to the PC. This module demodulates and converts the data from RF to UART format. The formatted serial data received through the R232 are fed to a LabVIEW based user interface for display, analysis and file storage.

List of figures:

Figure 1-1 General block diagram of an electronic radiation measurement system.....	4
Figure 1-2 A rack mountable NIM crate with various sub modules and a PC based user interface.....	6
Figure 1-3 A typical handheld radiation survey meter.....	6
Figure 1-4 A collection of portable survey meters.....	7
Figure 1-5 Internal architecture of a PSoC 1 chip.....	10
Figure 1-6 Neutron detection using semiconductor detectors.....	17
Figure 1-7 Schematic showing the location of dead layers in a PIN diode detector...	19
Figure 2-1 Simple boost converter showing the current variation in inductor with respect to time.....	23
Figure 2-2 Schematic of a practical high voltage generation circuit with closed loop regulation.....	24
Figure 2-3 Configuration of PSoC analog blocks for GM-counter application. The ACB 00 comparator block produces TTL pulses, ASD 11 implements an integrator for HV regulation along with the oscillator ASC 01 and the buffer ACB 01. ACB 02 and ACB 03 generate the clamp voltages.....	26
Figure 2-4 Schematic of the GM survey meter application board centered around the PSoC 1 chip with external passive networks for implementing HV generation, Oscillator timing and clamping.....	28

Figure 2-5 Pulse generation in GM tube.....	29
Figure 2-6 Photograph of a GM pulse captured on an oscilloscope.....	30
Figure 2-7 Typical time profile of a GM tube output voltage pulse showing a fast 60 μ s rise time. Typical decay time of pulse for the RC components used is 300 μ s with a 5 V positive overshoot.....	30
Figure 2-8 General clamping circuit with overshoot protection and high voltage isolation.....	31
Figure 2-9 On-chip analog PSoC blocks aid in integration of HV regulation modules and the core counting functions on to a single chip.....	33
Figure 2-10 Configuration of PSoC digital blocks for GM-counter application.....	36
Figure 2-11 Application board mechanical assembly for testing.....	36
Figure 2-12 Complete test setup with PC communication accessories and 0.1799 mCi cobalt-60 gamma source.....	37
Figure 2-13 Calibration graph with Co ⁶⁰ source of 0.1799mCi. Observed counts are plotted against calculated dose rates.....	38
Figure 3-1 General alpha spectroscopy system block diagram showing the detector, preamplifier, the pulse shaping filter and the peak sensing circuits.....	42
Figure 3-2 Block diagram of embedded pulsed reset alpha spectrometer. The PC with GUI, the mixed signal embedded platform, the front-end comprising a pre-amplifier, a reset device, a HV bias block and the dominant noise sources are shown.....	44

Figure 3-3 Structure of a planar PIN diode with all the important parts being shown..	46
Figure 3-4 The vacuum chamber used in this work and the PIN diode (inset).....	46
Figure 3-5 C-V characteristics of the M/S BEL PIN diode.....	48
Figure 3-6 (a) The pre-amplifier configuration with the dominant noise sources and (b) a typical tail pulse output with the resistive reset scheme.....	49
Figure 3-7 Preamplifier output with standard resistive reset scheme with a feedback resistor of 10M Ω . The pulse decays to ground level within 30 μ s.....	50
Figure 3-8 The basic preamplifier circuit with the feedback replaced by an analog switch.....	52
Figure 3-9 Output staircase waveform of pulsed reset pre-amplifier. The corresponding pulse shaper output and inhibit-logic waveforms are also shown.....	53
Figure 3-10 Flow chart of the Firmware operation running in parallel with a state machine in the embedded pulsed reset scheme.....	54
Figure 3-11 State machine for detection of pulse pile up during digitization.....	55
Figure 3-12 The timing constraint on the PE signal.....	58
Figure 3-13 The PSoC creator schematic for the on chip high voltage ramping and regulation module.....	60
Figure 3-14 PSoC creator schematic for the on-chip State machine module.....	61
Figure 3-15 PSoC schematic for the on chip digitizer and UART communication modules.....	62

Figure 3-16 Preamplifier output (c) shown along with the Pulse Edge signal (a) and the burst mode reset signal (b).....	65
Figure 3-17 Effect of slow ramping in the falling edge of the switch control waveform (b) on the preamplifier output (c).....	65
Figure 3-18 Switch control waveform generated using on chip PSoC blocks.....	66
Figure 3-19 The detailed alpha spectrum of Cm-224 from a mixed nuclide source along with the real-time Gaussian fit.....	68
Figure 3-20 Combined alpha spectrum of the mixed nuclide source plotted off-line from stored data. Energy calibration is done using the Cm-224 peak....	68
Figure 3-21 The detailed alpha spectrum of Am-241 from a mixed nuclide source along with the real-time Gaussian fit.....	69
Figure 3-22 The detailed alpha spectrum of Pu-239 from a mixed nuclide source along with the real-time Gaussian fit.....	69
Figure 4-1 Construction details of a planar neutron detector along with the neutron beam direction and capture product ion tracks.....	76
Figure 4-2 Evolution of the trench design from planar neutron detector (a).....	77
Figure 4-3 Effect of capture event location and ion emission direction on ion path length in semiconductor region.....	78
Figure 4-4 The concept of a unit cell. The complete detector shown in (a) is formed by the periodic repetition of the structure (b). (c) shows the front view of (b) along the positive y-axis.....	81

Figure 4-5 Initialization of the simulation by assigning random depths of interaction for neutrons and random assignment of direction cosines for the emitted ions in space.....	83
Figure 4-6 Ion energy deposition in different regions of a detector by one of the ions.....	83
Figure 4-7 Ions born in a converter region traverse multiple unit cells. Their path can be tracked inside a single unit cell using specular reflection at the boundary of their original unit cell.....	84
Figure 4-8 Flow chart showing the algorithm for estimation of energy deposited in silicon for a simple planar neutron detector.....	87
Figure 4-9 Flow chart showing the complete sequence of operations for estimating neutron detector efficiency.....	88
Figure 4-10 Variation of ϵ_{int} of a planar neutron detector with the thickness of the B^{10} converter layer.....	91
Figure 4-11 Variation of ϵ_{int} of a planar neutron detector with the thickness of the Li^6F converter layer.....	91
Figure 4-12 Variation of ϵ_{int} of a B^{10} coated planar neutron detector with LLD setting. The B^{10} thickness is fixed at $2.5\mu m$	93
Figure 4-13 Inclusion of dead layer at the bottom of the converter trench.....	95

Figure 4-14 Flow chart showing the algorithm for estimation of energy deposited in silicon for a simple planar neutron detector with the inclusion of a dead layer.....	96
Figure 4-15 Interpolated residual energy versus path length data for transport of Boron (B-10) neutron conversion ions in Gold (Au).....	98
Figure 4-16 Interpolated path length versus residual energy data for transport of Boron (B-10) neutron conversion ions in Gold (Au).....	99
Figure 4-17 Interpolated residual energy versus path length data for transport of Lithium-6 neutron conversion ions in Gold (Au).....	100
Figure 4-18 Interpolated path length versus residual energy data for transport of Lithium-6 neutron conversion ions in Gold (Au).....	101
Figure 4-19 Variation of the intrinsic neutron detection efficiency as the thickness of the dead layer is varied. Efficiency variation for both Boron and LiF converter materials are shown.....	102

List of tables:

Table 2-1 Calibration data of the designed GM counter.	38
Table 2-2 Comparison of design parameters of various brands of gamma survey meters.	40
Table 2-3 System parameters and corresponding values for Portable GM counter.....	41
Table 3-1 State variables and their corresponding state descriptions	57
Table 3-2 CMOS analog switches with design parameters considered for the reset function	64
Table 4-1 Estimated efficiencies for trench neutron detectors for different fractional converter trench widths. The unit cell width and the trench depth are kept at 4 μm and 10 μm , respectively.....	92
Table 4-2 Empirical fit of residual energy $\bar{E}_{im}(X)$ after a path length 'X' in gold (Au) for B10 conversion ions	101
Table 4-3 Empirical fit of path length $\bar{X}_{im}(E)$ to reach a residual energy 'E' in gold (Au) for B10 conversion ions.....	102
Table 4-4 Empirical fit of residual energy $\bar{E}_{im}(X)$ after a path length 'X' in gold (Au) for Li6 conversion ions.	103
Table 4-5 Empirical fit of path length $\bar{X}_{im}(E)$ to reach a residual energy 'E' in gold (Au) for Li6 conversion ions.....	104

List of figures in appendices:

Figure B.1-1 Photograph of the X-Y micro positioning stage with its PSoC based stepper motor controller.....	117
Figure B.1-2 Complete set up for laser patterning process with the X-Y micro positioning stage attached to a vacuum chamber.....	118
Figure B.1-3 User interface with real-time monitoring of the patterning process.....	118
Figure B.1-4 User interface while patterning 10 lines within a distance of 400 μm	119
Figure B.2-1 Structure of the drift chamber in an Ion Mobility Spectrometer Courtesy (https://www.smithsdetection.com , M/S Smiths detection, USA).....	120
Figure B.2-2 Block diagram of the HVPPS with PSoC based pulsing control.....	122
Figure B.2-3 Switching signal feed through in the HV output.....	123
Figure B.2-4 Reduction in switching ripple with the inclusion of HV passive filter.....	123
Figure B.2-5 Compact assembly for the IMS HVPPS with the PSoC application board shown.....	124
Figure B.2-6 The final filtered waveform with the pulsing operation shown.....	124
Figure B.2-7 The output of the trans-impedance amplifier connected to the collector plate of the IMS chamber. The initial dip indicates the presence of oxygen molecules.....	125
Figure B.3-1 Schematic blocks of the electronic glove.....	126
Figure B.3-2 Photograph of the handheld subsystem with the sensor mounting on the finger shown.....	128
Figure B.3-3 Schematic of the PC based module.....	129
Figure B.3-4 LabVIEW GUI screen shot.....	129

CHAPTER 1 Portable radiation instruments –trends and scope for design improvements

1.1 Radioactivity for mankind

The birth of the field of radiation science and technology was marked by two consecutive serendipitous discoveries, namely x-rays by Wilhelm Roentgen in the year 1895 and spontaneous radioactivity from uranium salts by Henri Becquerel in 1896. Over a century since these discoveries, the use of radioactivity and radio-isotopes in various other fields like science, engineering and medicine has seen rapid advances. In fields such as earth sciences, the technique of radiometric dating is used to determine the geologic ages of various rocks and rock formations. Radio-isotopic tracers are used in environmental sciences to assess water pollution and to survey ground water resources. In the biological sciences, the radio-isotopic tracer technique is used to study complex metabolic cycles; while in astronomy, observations in the gamma energy range of the electromagnetic spectrum are increasingly utilized to augment our understanding of cosmic phenomena. The food and agriculture industry utilizes ionizing radiation for developing high yielding crop varieties through radiation induced mutations in plant breeding. Low doses of ionizing radiation are also used for sterilization of food. Radiation induced cross linking of polymers is a recent technique to produce special quality plastic and rubber insulation materials for industrial applications.

Another major area of application of ionizing radiation is in medical imaging, especially for cancer diagnosis. Medical imaging techniques such as x-ray radiography, x-ray computed tomography, Single Photon Emission Computed Tomography (SPECT) and

Positron Emission Tomography (PET) all use ionizing radiation to probe the inaccessible interior tissues of the human body. Radiation oncology is a major area utilizing ionizing radiation in techniques such as external beam radiotherapy and brachytherapy for the treatment of cancer.

The foremost engineering and industrial application of radioactivity is in power generation, based on the neutron induced fission reactions. The material penetration capability of nuclear radiation is utilized in techniques such as neutron radiography for non-destructive testing and evaluation of steel structures and non-contact thickness measurements of metal / plastic sheets [31].

All the above applications have been made possible due to our increasing scientific understanding and technological advances in the field of radiation physics and engineering.

1.2 Radiation

Energetic radiation of nuclear origin is broadly categorized into four general types, namely

- (a) fast electrons, such as beta particles and positrons
- (b) energetic heavy nuclei such as alpha and heavy ions
- (c) high energy electromagnetic radiation such as gamma rays and
- (d) Neutrons.

A major part of the technological work in the application of radiation science is concerned with generation, detection and measurement of nuclear radiation of all the types mentioned above. The controlled generation of nuclear radiation is achieved either

through natural means or through artificial means. Spontaneous nuclear processes like beta or alpha decay, internal conversion and spontaneous fission constitute natural sources. Synchrotrons, decay induced neutron generation and fission induced radiation generation from reactors constitute artificial sources. In addition to these, the list of artificial sources also includes accelerator based sources which employ techniques like bremsstrahlung generation, characteristic x-ray generation and photo-neutron generation [32].

Energetic heavy nuclei and fast electrons comprise different particles from a wide variety of sources, both natural as well as artificial. However, the most widely encountered of these in the nuclear industry are the nuclei of helium atoms which are spontaneously emitted from isotopic sources and fast electrons. These are known as alpha and beta particles, respectively. Alpha particles have higher energies which typically fall between 3 to 7 MeV. In terms of penetration into matter, the heavier alpha particles are least penetrating and can be stopped by a thin sheet of paper. On the other hand, the typical energies of beta particles lie in the range of tens to hundreds of keV, but are more penetrative than alpha particles. They can be stopped only by a denser medium such as a thin sheet of aluminum.

Energetic electromagnetic radiation accompanying a spontaneous alpha or beta decay in nuclei that undergo transition to low energy states is known as gamma radiation. This is the most prominent natural source of ionizing electromagnetic radiation. Typical gamma energies lie in the tens of MeV range. These are capable of penetrating many centimeters of lead or many meters of concrete. Neutrons are another major uncharged radiation in addition to gamma. A variety of sources like spontaneous fission, alpha induced nuclear reactions, gamma induced nuclear reactions and accelerator based sources produce neutrons with energies typically ranging from 0.025 eV to tens of MeV.

Neutrons are the most penetrating radiation of all the categories. They can penetrate meters of concrete.

The detection of these nuclear radiations and the measurement of various physical parameters associated with them is the concern of the field of radiation instrumentation.

1.3 Design principles of radiation instruments

1.3.1 Charge collection mechanism and detector electronics

As shown in figure 1-1, the core of a typical electronic radiation instrument consists of a detector, its associated electronic circuits and a human interface for reading the measurements. The individual quanta of radiation interact with the detector by

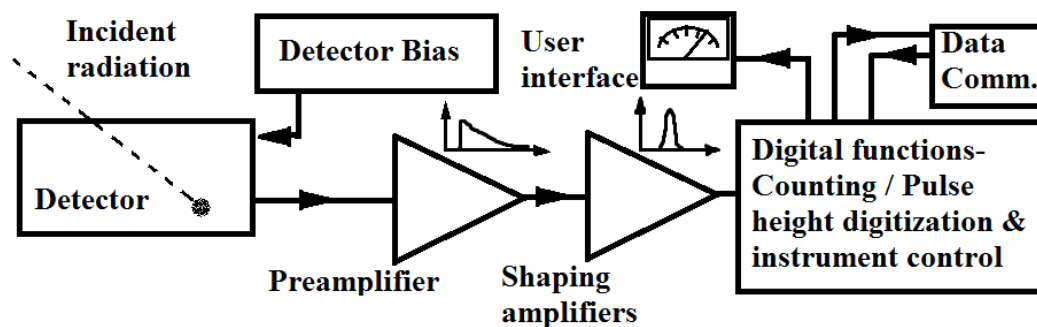


Figure 1-1 General block diagram of an electronic radiation measurement system showing important components

different mechanisms [32], which in turn dictates the mode of instrument operation. The net result of any such interactions is the formation of a finite amount of electric charge inside the detector volume. An imposed electric field inside this active volume sweeps these charges to external electrodes typically enclosing the volume. Thus, each quanta of radiation produces a primary signal which is a momentary pulse of current resulting from the motion of the swept charges. The typical order of magnitude of this current signal is 10^{-12} A and hence, it needs to be amplified for further processing and driving the dial

based user interfaces. This function, known as the front-end signal processing is typically performed by either a charge sensitive preamplifier or a trans-impedance amplifier. The subsequent signal processing chain consists of analog filter circuits, digital counters / pulse height analyzers. The user interface controllers also perform important functions in the instrument in conjunction with the circuits for driving the analog/ digital meters [32]. In addition to the signal processing circuits, the systems employ high voltage generation circuits for generating the imposed electric field. All the electronic circuits associated with the detector are collectively termed as the detector read-out electronics.

1.4 Categories of Radiation Instruments

Right from the early days of research pertaining to application of radioactivity for the welfare of mankind, two distinct categories [2] of instruments have emerged namely,

- (a) Laboratory based instruments and
- (b) Portable instruments.

Laboratory based radiation instruments are generally systems which are installed in nuclear facilities like reactors and high energy physics laboratories. Typically, they employ custom-made detectors and large detector arrays in conjunction with high performance electronics for unique research applications and cater to a specific type of radiation. A common laboratory based radiation instrumentation system is a NIM (Nuclear Instrumentation Module) crate based system shown in figure 1-2. A NIM crate system is a large rack mounted system consisting of multiple high performance electronic sub modules in various standardized slots, each performing specific functions such as signal processing, detector biasing, pulse counting, digital pulse height analysis and digital communication for remote user control.

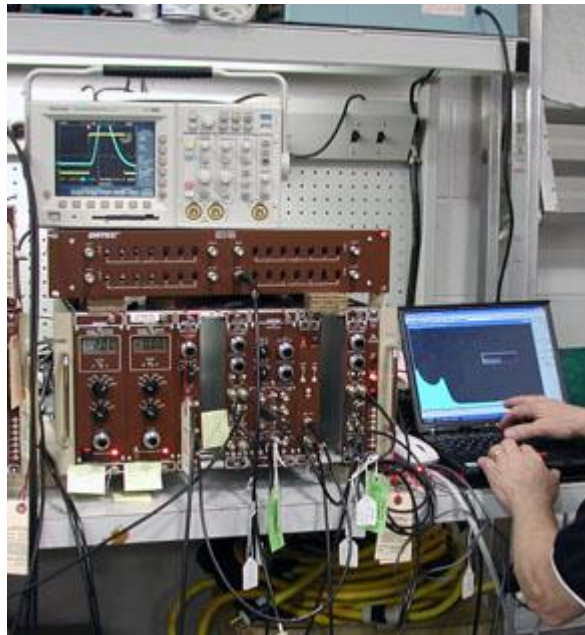


Figure 1-2 A rack mountable NIM crate with various sub modules and a PC based user interface (courtesy ortec-online.com, M/s Ortec, USA)

On the other hand, portable instruments are generally handheld systems which can be carried by a human user for on-field measurements (figure 1-3). These are generally employed for applications like environmental gamma dose survey, on-field energy spectroscopy etc. Typically, these are single detector systems as shown in figure 1-4, with miniaturized low power electronics for signal processing and user interface.



Figure 1-3 A typical handheld radiation survey meter (courtesy mirion.com, M/s Mirion Technologies, USA)



Figure 1-4 A collection of portable survey meters
(Courtesy <http://www.spss.com.sa>, M/s Tracerco, UK)

1.4.1 Factors affecting design choices for portable instruments

The context and motivation for the present thesis can be better drawn by tracing the evolution of electronic read-out design for radiation applications. Over the years, a variety of designs for portable instruments have evolved, motivated by a need to meet challenges in different applications on field. One such application pertains to area monitoring and personnel dosimetry measurements in large nuclear facilities [33]. Although diverse platforms have emerged for implementing detector read-out electronics for portable systems, there are difficulties in using them for instrument designs in a straightforward manner. The optimization of system level design of portable radiation instruments is affected by various constraints on field like

- a) Severe limitations in available power, resulting from the use of electrochemical batteries
- b) Use of lower supply voltages in the range of less than 12 V, necessitating the use of power converters.

- c) Extreme variations in temperature and moisture.
- d) Presence of electromagnetic interference.
- e) Accidental mechanical shocks.
- f) Likelihood of instrument operation by semi-skilled users.
- g) Space constraints in human- machine interface.
- h) Constraints in weight, size and shape.

In addition to these, the design choice also depends intricately on parameters like mechanisms of interaction of radiation with the detector media and the corresponding signal characteristics. A brief account of the evolution of the portable instrument designs influenced by the design constraints stated above is given in the next section.

1.4.2 Evolution of instrument designs

One of the earliest portable instruments for detection and measurement of nuclear radiation was the gold leaf electroscope, which worked on the principles of electrostatics. Further design of instruments with improved sensitivity and accuracy for portable radiation measurements was made possible in the 1920s, with the widespread availability of rugged detectors and precision electronic amplification. Gas filled detectors like ionization chambers, proportional counters and Geiger Mueller tubes utilizing vacuum tube thermionic valves for electronic signal processing dominated the portable instrument domain. Although the electronic read-out designs for detectors were implemented using vacuum tubes in the initial stages, they graduated later on to using discrete electronics based on transistors. Issues such as non-miniaturization and power consumption associated with transistors, together with the emergence of the microprocessor during the 1980s, led to an exodus of design implementations to the new platform. The new microprocessor based platforms had the added advantage of in-built features such as digital signal processing, data storage/ retrieval and communication. During the last three

decades, platforms like microprocessors, Field Programmable Gate Arrays (FPGAs) and Application Specific Integrated Circuits (ASICs) reigned supreme as a preferred choice of the design community [4], in spite of their high costs. The cost of these platforms is attributed to their powerful architecture and higher clock rates in the hundreds of MHz range, which have enabled high speed complex digital operations.

In the recent past, numerous technological advancements have taken place in two important fields, viz. Integrated Circuits (IC) and semiconductor radiation detectors. Advances in IC technology have led to the emergence of numerous reconfigurable mixed signal hardware platforms, in addition to the development of high performance commercial Operational Amplifiers (Op-Amp). Owing to their generic support for a wide range of applications, reconfigurable mixed signal platforms are available at a substantially lower cost compared to microprocessors and other high performance digital platforms [3, 5, 6].

Advanced Design platforms

Recent platforms such as Programmable System-on-Chip (PSoC) are software-configured mixed signal arrays with built-in MCU core. A PSoC IC has a CPU core, configurable analog and digital blocks, PLD based programmable logic all integrated on a single chip. Three different families of PSoC ICs are in widespread use in the embedded design community. The first is the PSoC 1 family with an M8C microprocessor core and a limited number of analog and digital resources (figure 1-5). It has a maximum clock rate of 24 MHz. PSoC 3 is an intermediate version with clock rates reaching upto 67MHz. PSoC 5 LP is the latest version and has a 32 bit ARM cortex M3 processor core with upto 80 MHz clock speed. The supply voltage of this particular IC can be as low as 3.3 V. The PSoC architecture allows the user to create customized

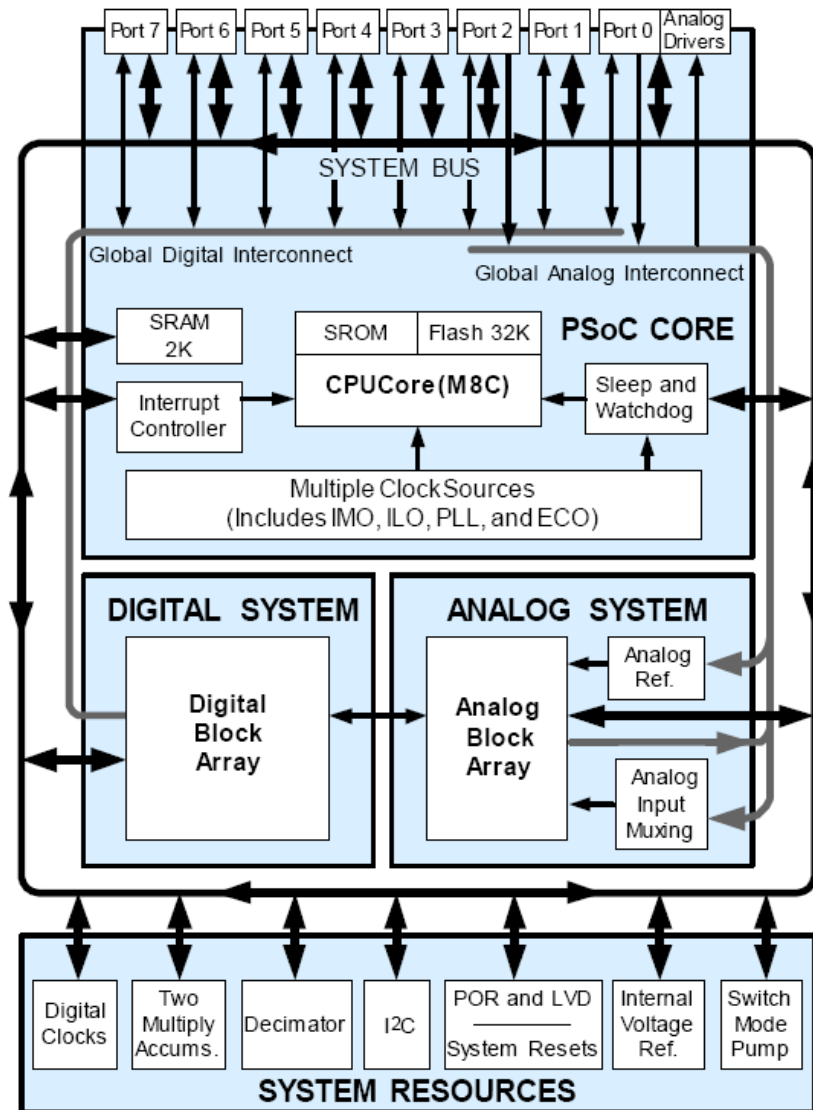


Figure 1-5 Internal architecture of a PSoC 1 chip

peripheral configurations, to match the requirements of each individual application. Their moderate clock rates in the range of tens of MHz make them incapable for direct implementation of high speed digital functions. However, the presence of features such as on-chip programmable analog array and dynamic reconfiguration [7] enable indirect implementation of conventional digital functions. These features combined with availability of systematic embedded design methodologies [8-10] result in shorter application development times. Apart from these, the near-zero non recurrent engineering

costs endow these platforms with the potential to reduce the overall cost of system design in portable embedded applications.

Developments in detectors

Planar technology, originally developed for integrated circuit fabrication on silicon wafers, was successfully applied to detector fabrication in the year 1984 by J. Kemmer [34, 35]. This has led to the development of novel light converter devices like Avalanche Photo Diodes (APDs) and Charge Coupled Devices (CCD) used in conjunction with scintillation detectors. A byproduct of this technology, is the development of fabrication processes for fine pixilated and compound semiconductor detectors [1]. Planar technology has also been applied for conventional devices to improve their performance characteristics. For example, in planar PIN diodes, ultra-low dark currents and substantial reduction in surface leakage currents have been achieved by the use of guard rings [36]. These are now available at an attractive cost as a result of continuous process improvements motivated by their increased demands in optical communications and high energy physics experiments. The following sections motivate the aim of the current thesis, with a description of current state of the art instruments and the challenges thereof. A prescription is laid based on PSoC platform as applied to gamma survey meters and portable alpha spectrometers. In addition to this, improved simulations for planar semiconductor neutron detectors are performed in this work.

1.5 Motivation for the thesis

1.5.1 State-of-the-art gamma survey meters - Limitations

Gamma radiation survey forms the basis of various operational aspects of nuclear industry such as mineral exploration, routine monitoring of activity in and around nuclear

facilities, risk assessment during nuclear emergencies etc. This application demands portable instruments which aid health physics workers in measuring and recording the radiation dose rates at various locations in the field. Over the years, numerous portable instrument designs for gamma survey have been developed [37, 38]. Some of the detectors used in commercially available portable systems [37] include, ion chambers, Geiger- Mueller (GM) tubes and scintillation based detectors like NaI, CsI, LaBr₃ etc. coupled with photo-detectors.

Although many types of detectors are available, the detector that finds the most widespread use is the GM tube. This is due to its simple construction and large signal output which aids in implementing cost effective designs. The large signals in the GM tube are the result of a gas avalanche phenomenon known as Geiger discharge which occurs at high voltages (~500V) in a gas filled tube. The avalanche is started by a secondary electron which originally is generated by a gamma interaction either in the solid wall or the gaseous interior of the detector. This original interaction of gamma radiation is by photo-electric absorption, Compton scattering or pair production, which results in transfer of a major portion of gamma energy to the electron in a single interaction. The presence of large signals (> 1V) eliminates the need for precision amplification in the front-end while designing counting and read-out systems. However, the requirements for a stable HV bias, data processing and user interfaces slightly increase the complexity in this system design.

State-of-the-art portable instrument designs for gamma survey such as DSM-500 of M/s WB Johnson Instruments [39], Model-2242 of M/s Ludlum Instruments [38] and PRSM-1 of M/s Para Electronics [40] are centered around the conventional platforms like microprocessors or microcontrollers. Although these designs are extensively used and standardized, they require peripheral ICs and associated modules to implement the

various functions required for GM tube operation and user interface. The addition of peripheral circuits has increased the cost of the systems, complexity as well as their size cumulatively.

In the present work, a novel scheme for implementing the GM tube read-out functions is designed, in order to overcome the drawbacks of microprocessor based designs. This scheme integrates the implementation of the signal processing, HV biasing, data processing and user interface functions onto a single-chip mixed-signal PSoC platform.

1.5.2 Portable alpha spectrometers – State of the art and challenges

In the nuclear industry, the importance of alpha spectrometry cannot be undermined as it plays a key role in environmental site characterization and radiation protection. Accurate and precise measurements of alpha radiation in field applications demand commensurate high sensitivity and selectivity. The quality of the data / spectrum acquired, is invariably dictated by the detector and associated signal processing electronics.

The detection of alpha particles and / or the measurement of their energies are based on their columbic interaction with the electrons of any absorber media. The absorber medium can be a solid, liquid or a gas. The positive charge of an energetic alpha particle provides an attractive impulse of the Coulomb force to the electrons of an absorber medium as it passes through their vicinity. This impulse either excites the electrons of absorber atoms to a higher-lying shell or completely removes them. In this process, the kinetic energy of the interacting alpha particle is incrementally reduced. In the case of interactions resulting in excited atoms, an alpha particle is detected through the collection of scintillation photons inside a light sensor such as a photo-multiplier or a photodiode. The scintillation photons are emitted when the atoms de-excite. For

interactions resulting in ion pairs, the collection of electrons and ions in the electrodes enclosing the detection volume enables the detection of alpha particles. Detection of alpha particles in liquid media mainly utilizes the scintillation phenomena, while its detection in solids and gases is enabled by the collection of ionization charges. In applications where the alpha particle energy is measured, the volume of the absorber is chosen such that the alpha particle completely deposits its kinetic energy inside the absorber.

As far as portable alpha spectrometry is concerned, many designs based on high quality solid state detectors such as Silicon Surface Barrier (SSB) detectors and Passivated Ion Implanted Planar Silicon (PIPS) detectors that are commercially available have been explored. Recent designs for rapid in-situ determination of radiation contamination utilizing PIPS detector for alpha particle energy measurement have been reported by S.W. Kwak *et al.*, Y.Cheng *et al.* and A. Martin Sanchez *et al.* in refs.[41, 42] and [43], respectively. These designs are based either on commercially available microcontroller platforms [42] or general purpose multichannel analyzers (MCAs) [43]. The digital functions have been implemented with high cost commercial components in these designs. Further, the analog processing design utilizes precision discrete Op-Amp circuits [42] or crate based NIM circuits rendering them less portable and more expensive. Moreover, the use of the expensive PIPS detectors increase the system cost many folds. There is therefore, a concerted research effort to substitute the expensive detectors and analog front-end electronics with inexpensive ones. A possible choice for the detector and analog front end electronics are low cost PIN diodes and Commercial-Off-The-Shelf (COTS) Op-Amp based circuits, respectively.

Some recent attempts employing low cost planar PIN diode based alpha detection systems with widely available cheap electronic components and PC technologies have

been reported in literature [44]. But this design by D. Vujo *et al.* implements a conventional signal chain and employs several Op-Amps for shaping, peak detection, linear gating, pulse stretching, pulse discrimination, timing and control functions. This design with several discrete Op-Amps has shortcomings in terms of increased cost, in spite of the use of low cost detectors. In addition to this, multiple stand-alone modules are used for functions like HV bias and analog processing in the front-end. This makes the design less reliable, susceptible to interference / noise and inefficient in terms of board real estate. In the present thesis, a low cost front-end design based on a novel embedded pulsed reset technique, utilizing the PSoC platform is explored. This design successfully overcomes the above stated shortcomings of existing designs. Moreover, the design is more compact and reliable as it uses a single PSoC chip for precision analog processing in the front-end, regulation of HV bias and data communication to a PC.

1.5.3 Planar Neutron detectors and design optimization.

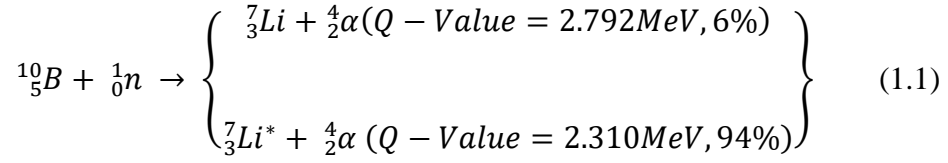
Portable neutron detection and dosimetry is a typical application, where semiconductor based detection has the potential to drastically improve system reliability and efficiency in a cost effective manner [45]. This improvement is realized by replacing conventional detectors like proportional gas counters (He^3 or B^{10}F_3 gas filled tubes) and photo multiplier tube (PMT) coupled scintillators [46] with semiconductor neutron detectors. The deficiencies of conventional gas filled neutron detectors include, requirement of expensive high-voltage bias modules, sensitivity to micro-phonics[32] and high cost of production due to recent shortages of He^3 gas [47, 48]. Similarly, the scintillator based neutron detectors suffer from drawbacks like, poor gamma-ray discrimination and involve high-cost of production. Moreover, the most vital component in these detectors which is the PMT, is fragile, power intensive and sensitive to external

magnetic fields. The drawbacks of both gas filled detectors and scintillation detectors are overcome by the employment of semiconductor based detectors.

The operation of neutron detectors – gas filled He3, scintillator and semiconductor based-in general, is based on the indirect detection of product ions generated as a result of capture reaction of neutrons with a neutron sensitive converter material [48]. For example, in PIN diode based planar neutron detectors, the choice of the converter material and its geometry is driven by the detector efficiency solicited for neutron detection. The intrinsic neutron detection efficiency (ϵ_{int}), which is defined as the probability that a neutron entering the detector volume gets registered, is a decisive factor in the design of the detectors [49]. While its value depends on many parameters, the type of converter material and its relative dimensions vis-a-vis the semiconductor regions are the most important ones. As these parameters are interdependent, for practical production of neutron detectors, their optimization is imperative. Therefore, to aid in detector fabrication, simulations of the operation of planar PIN diode neutron detectors coated with thin films are investigated as part of this research work. The optimization methods adopted are intricately related to its principle of operation.

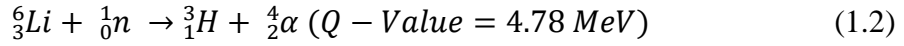
The neutron being a sub-atomic particle with no net electric charge, cannot be detected by direct interactions by the coulomb force with electrons of a detection medium. The only interactions of a neutron with any media which aid in its detection are the neutron capture and the neutron scatter interactions. The capture interaction results in charged particles with large kinetic energies independent of the energy of the neutron causing it. It is also characterized by a higher interaction cross section (i.e. probability of interaction) for the thermal energy range (≤ 0.025 eV) of neutrons, prompting its use for detection of slow neutrons. The two most important capture interactions used for detection of slow neutrons are

(a) The $^{10}\text{B}(\text{n}, \alpha)$ reaction



and,

(b) The $^6\text{Li}(\text{n}, \alpha)$ reaction.



The energy released in these reactions, known as the Q-value is sufficiently large, making the kinetic energy of the products assume prominence in the detection mechanism compared to the small energy of the incident neutron. The schematic design of a neutron detection instrument utilizing semiconductor detectors is shown in the figure 1-6.

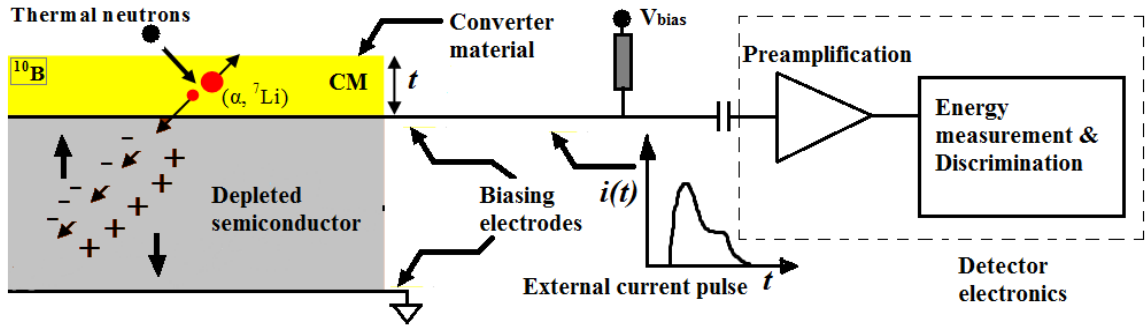


Figure 1-6 Neutron detection using semiconductor detectors

The converter material (CM) consists of materials with either Li^6 or B^{10} . These detectors are constructed such that, the energetic product ions that are generated inside the CM indicated by equations (1.1) and (1.2), travel to a depleted semiconductor region placed adjacent to it. *It should be noted that henceforth the product ions will be referred to as ions in the ensuing chapters.* These energetic ions in turn, undergo energy loss through coulombic interactions and generate electron–hole (e-h) pairs in the bulk of the depleted semiconductor region. The e-h pairs thus generated are swept to the electrodes biasing the

semiconductor region, thereby contributing to an external current pulse. This current pulse is further processed by the detector electronics for energy measurement, which aids in registering the neutron event. Usually, the simple stacked configuration with the converter layer deposited over a semiconductor wafer is widely employed. However, many other complex configurations of arranging the CM relative to the semiconductor bulk are also being explored for neutron detection [23]. In planar geometry detectors, there exists a critical thickness ' t_c ' that is decided by the probability of neutron interaction, range of the generated charge particles in CM and their probability of reaching the semiconductor detection volume. Therefore, there is a need to optimize various parameters and t_c in particular, through probabilistic methods, to achieve maximum ϵ_{int} .

In practical detectors containing semiconductors and metals, the ions see varied electric field depending on the material of interaction. The energetic ions travel through semiconductor regions with a high electric field as well as through regions with very weak or zero electric field such as heavily doped P⁺ regions and the bulk of metal electrodes. They undergo energy loss in these regions also by coulombic interactions. These interactions generate charged particles which cannot be swept to the electrodes because of the weak or zero electric field. Hence, the ion energy lost in these regions generally known as 'dead layers' is not accounted for in the external signal. Therefore, it is important to consider the effect of this energy loss in the determination of ϵ_{int} . It is to be noted that the magnitude of ϵ_{int} , critically hinges on the accurate measurement of energy deposited inside the detector [50]. In a planar neutron detector, the metal electrode layers on top and bottom of the depletion region along with the heavily doped p⁺ and n⁺ regions as shown in the schematic (figure 1-7) act as dead layers.

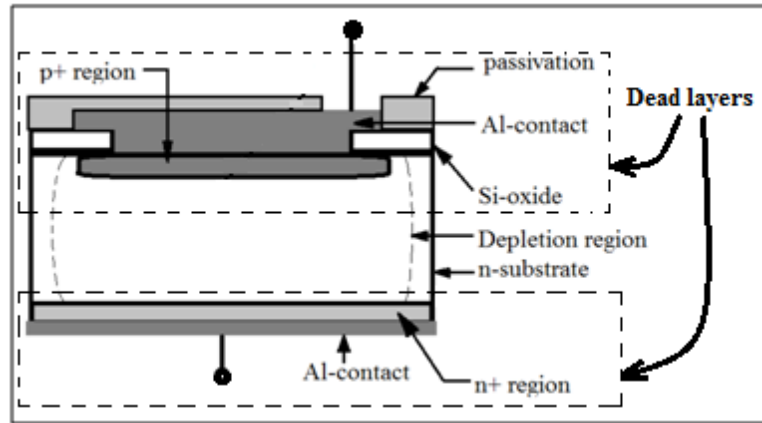


Figure 1-7 Schematic showing the location of dead layers in a PIN diode detector

The estimation of ϵ_{int} by simulations has been extensively studied by Bellinger *et al*[26]. However, these studies have limited themselves with a Lithium based converter layer in a simplified detector model, wherein the dead layer effects are excluded. These shortcomings in [26] have been addressed in this thesis by the inclusion of the dead layer. Specifically, this thesis describes the effect of a gold (Au) dead layer on the magnitude of ϵ_{int} , since the electrodes that are generally used in the planar PIN diode based devices are made of gold or aluminum.

1.6 Organization of the thesis

This thesis is organized into five chapters. The first chapter being introduction, the second chapter describes the implementation of an embedded design for bias control and readout in GM counter application. The third chapter describes the execution of a low cost alpha spectrometer design using commercially available large area planar PIN diode detectors in conjunction with a PSoC based embedded pulsed reset readout system. The fourth chapter dwells in detail, the design optimization of semiconductor neutron detectors in planar configuration using Monte Carlo simulations. The fifth and the final chapter provides a brief summary of the design objectives achieved and briefly touches

upon the future scope. For the sake of completion, the PSoC programs relevant to the thesis work are listed in appendix A.

Although the central theme of the thesis is on application of PSoC to radiation detection, PSoC based applications have also been developed for non radiation detection. These miscellaneous applications include design of PSoC based systems for X-Y table control, compact High Voltage Pulsed Power Supply (HVPPS) and wireless electronic hand tremor monitoring. These are described in the appendix B of this thesis.

CHAPTER 2 PSoC Embedded design for Geiger Mueller survey meter – bias control and readout

2.1 Introduction

GM counter is a very versatile particle detector that is widely used in the area of detection of nuclear occurrences[32] such as alpha, beta and gamma rays. This counter is basically gas based and works on the principle of ionization. The working and performance of GM counters critically hinges on functions like generation and regulation of high voltage, signal conditioning, pulse discrimination and digital counting. GM counters by their nature of construction are simple [51] and generate large output signals which obviate the need to use any precision amplification in the front end [32]. This feature makes it an ideal detector for gamma survey meters, where simple and economical counting is of paramount necessity [52]. However, the survey meters need to be portable, lightweight, operator friendly and cost effective. The current design of portable systems such as DSM-500 of M/s WB Johnson Instruments [39], Model-2242 of M/s Ludlum Instruments [38] and PRSM-1 of M/s Para Electronics [40] are microprocessor based. These require external, peripheral Integrated Circuits (ICs) and associated modules to implement the essential survey meter functions stated above, which eventually increase their weight and cost in a cumulative manner.

The present chapter discusses an electronic design for GM tube readout which is based on a reconfigurable single-chip mixed-signal platform- the PSoC platform. All the essential functions are designed and executed on a single PSoC IC. This implementation circumvents the need for external peripheral components which add to the weight and Bill

of Materials (BoM) [53]. Moreover, the multi-feature capabilities of PSoC, like the inbuilt power line digital communication support and a large memory endow the design to be either expandable as an area gamma monitor and converted into a compact personal dosimeter, respectively.

2.2 PSoC based enhancements in GM counter building blocks

The current design appends modular features such as those listed below, in such a manner that the performance of portable GM counter is achieved at a competitive cost.

- (a) Generation of High Voltage (HV) and biasing of the GM tube.
- (b) Acquisition of raw analog pulses from GM tube.
- (c) Conditioning the raw pulses to form logic pulses.
- (d) Counting the logic pulses with time gating.
- (e) Operator interfacing for dose information.

The following sections describe in detail, the existing designs of each of the above listed functions in the commercial systems, their limitations and methods of overcoming them by using PSoC based single chip design.

2.2.1 Regulated HV power supply

2.2.1.1 Existing commercial system design

The generation and regulation of high voltage (~500 V) for biasing the GM tube is a basic design necessity in the GM survey meter. For portable applications, the only source of power supply is from a battery (Typically 9V), from which other higher voltages have to be derived. In general, voltages higher than the battery level are generated using the DC-DC boost converter circuit in portable applications. This circuit works on the principle of generation of pulsed high voltage by the fast switching of

magnitude of an inductor current between two different values. This method has also been adopted in the past for applications in GM counters [38, 39]. Figure 2-1 shows a conceptual schematic of a simple boost converter explaining the current switching principle.

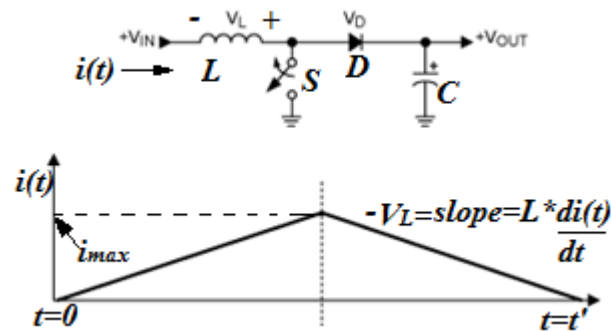


Figure 2-1 Simple boost converter showing the current variation in inductor with respect to time (Courtesy: <https://www.maximintegrated.com/en/app-notes/index.mvp/id/2031>, M/s Maxim integrated, USA)

In the schematic shown, the switch S is initially closed for a long time and a constant current i_{max} is established in the inductor L . When the current $i(t)$ is suddenly switched from the established constant value i_{max} to zero by opening the switch, a momentary high voltage is generated on the pole side of the switch (marked '+'). This momentary high voltage V_L is stored in a capacitor C by a momentary current pulse, passed through the forward biased diode D . The stored pulse voltage is further processed to act as a source. It is to be noted here that the capacitor charge is constantly replenished by repetition of the switching action, since any resistive load connected to the capacitor C discharges it. This repetitive switching is practically accomplished by replacing the mechanical switch in figure 2-1 with a transistor/ MOSFET switch as shown in figure 2-2. While the transistor/ MOSFET switch **Q1** is controlled by a pulse train in its base/ gate terminal, its collector/ source terminal and the emitter/drain terminal emulate the pole

side and the free contact side of the mechanical switch, respectively. In practical circuits, the inductor **L** in figure 2-1 is often replaced by a transformer **T1** as shown in figure 2-2.

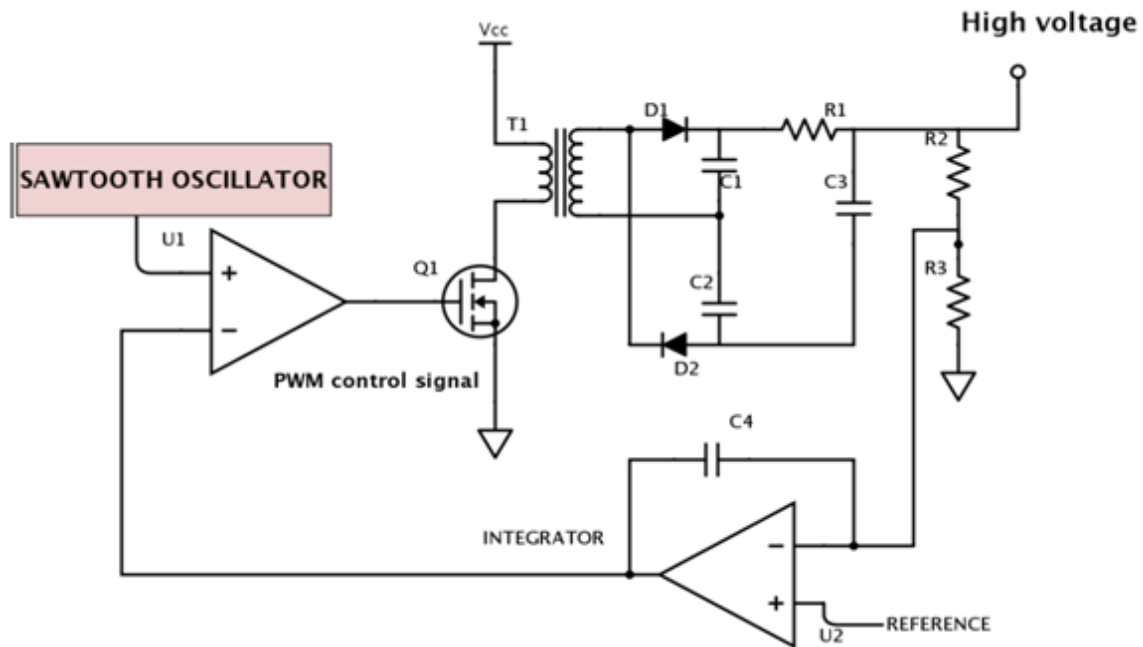


Figure 2-2 Schematic of a practical high voltage generation circuit with closed loop regulation

The use of a transformer serves two purposes, namely

- 1) limiting the maximum voltage developed across the switching element **Q1** to safe levels and
- 2) Providing galvanic isolation between its primary and secondary side circuits.

In addition to these, the transformer also enables the utilization of the high voltage developed during both the turn-on and turn-off cycles of the primary coil, in conjunction with the diode-capacitor based voltage-doubler network (**D1, D2, C1, C2**).

A simple relation (equation (2.1)) between the input voltage V_{in} and the output voltage V_{out} of a boost converter in terms of the duty cycle D of the pulse train is given by [54] .

$$V_{out} = \frac{V_{in}}{(1-D)} \quad (2.1)$$

where,

$$\textbf{Duty Cycle (D)} = \frac{T_{on}}{(T_{on} + T_{off})} \quad (2.2)$$

The duty cycle as defined in the above relation of equation (2.2), is the ratio of the time for which the switch is kept closed (T_{on}), to enable a current to pass through the inductor L , to the total cycle time ($T_{on} + T_{off}$), where T_{off} is the time for which the switch is open. Thus, as the duty cycle D approaches unity, an output voltage V_{out} , greater than the input V_{in} can be generated. It should be noted that the duty cycle D cannot take the values of zero or unity. Both these cases correspond to a situation where the switching waveform itself is a constant DC value, either at zero or at a finite positive value below the supply voltage of the switching circuitry. This prevents any change in the inductor current $i(t)$. This relationship of equation (2.1) establishes that a constant high voltage source with a wide voltage range can be realized using duty cycle control of the signal fed to the base of the switching transistor (**Q1**). This is also known as the Pulse Width Modulation (PWM) technique. But, high voltage fluctuations have to be corrected for, using a feedback system [55]. This correction is achieved by closed loop control of the duty cycle using a simple proportional- integral (PI) principle [56] as shown in figure 2-2. The feedback chain in this closed loop system consists of a sensing network (**R2** and **R3**), an integrator, a relaxation saw tooth oscillator and a comparator (**U1**) in sequence.

Existing designs in commercial GM survey meters utilize discrete OPAmps [38, 39, 57] for the three functions listed above, namely integrator, relaxation saw tooth oscillator and the comparator. The high voltage generation and regulation relying on the above design increases both the board space as well as the cost of the system. In order to overcome these limitations, a compact and reliable alternative design is adopted in this

work. The present design utilizes on-chip components of a single PSoC-1 integrated circuit for implementing the feedback chain for HV regulation.

2.2.1.2 PSoC based HV design

In the present design based on PSoC-1 chip, a high voltage of 500 V generated using the external circuit consisting of the switching transistor (**Q1**), the transformer (**T1**)(figure 2-2) and the voltage-doubler network, is regulated using feedback components internal to the PSoC chip. This design utilizes the generic internal switched capacitor user modules (**ASC** and **ASD** blocks) of a PSoC- 1 chip to perform the PWM function as shown in figure 2-3.

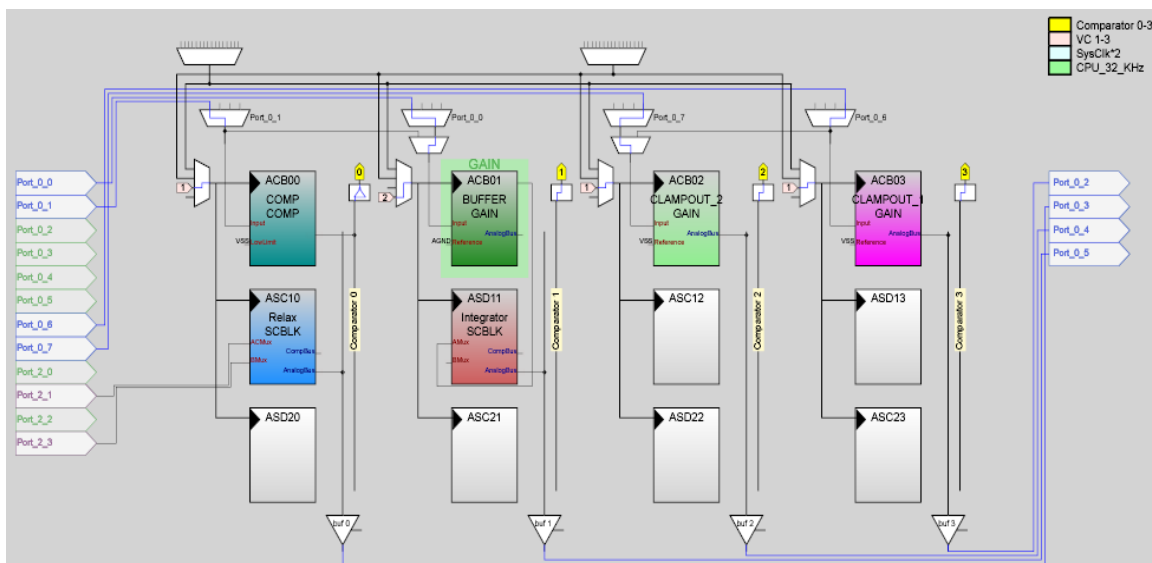


Figure 2-3 Configuration of PSoC analog blocks for GM-counter application. The ACB 00 comparator block produces TTL pulses, ASD 11 implements an integrator for HV regulation along with the oscillator ASC 01 and the buffer ACB 01. ACB 02 and ACB 03 generate the clamp voltages

The regulation is done by a feedback technique, wherein the output is sampled at the voltage divider network (**R2** and **R3** in figure 2-2). This feedback voltage is integrated by a PSoC internal Op-Amp (**ASD 11** in figure 2-3) configured as an integrator [58]

provided with an internal reference voltage of 2.6 V. This internal reference voltage is generated using on-chip band-gap diode and its associated stabilization circuit. The temperature stabilized band-gap reference [59] voltage endows this design with improved reliability compared to other designs. In other designs such as [38], the reference voltage is generated either through a simple voltage divider or by employing discrete zener diodes, both of which are sensitive to variations in ambient temperature.

When the sampled voltage is less than or greater than the reference voltage, the integrator produces a positive ramp or a negative ramp, respectively. In general designs, the ramp signal so obtained is either compared with the output of a sawtooth oscillator or is used to control the base current of a blocking oscillator to produce a PWM signal [38, 39]. In this design, this ramp signal is directly fed at the threshold point connected to the non-inverting input of an on-chip PSoC Op-Amp (**ASC 10** in figure 2-3) configured as a relaxation oscillator. An external RC-network (**VR5** and **C11** in schematic figure 2-4), fixes the frequency of the relaxation oscillator at 400Hz. The output of this setup is a PWM signal which controls the opening and closing of the external switching transistor (**Q1**) in figure 2-4, ensuring a regulated voltage of 500 V for the GM tube. Once a high voltage of ~500V is generated and connected to the central conductor of the GM tube with its chassis (which is grounded) as reference, the GM tube produces pulses for the passing nuclear occurrences. The merits of the present design can be better appreciated when the HV features are compared and contrasted with those of other systems. For example, Model 2242, DSM-500 and PRSM-1 use a blocking oscillator based topology. Whereas, the present design implements a topology where, an on-chip DMA based waveform generation from PSoC is used. The choice of the present topology provides advantages in terms of programmability and conversion efficiency.



2.2.2 Raw analog pulses from GM tube: input protection circuitry using PSoC

Figures 2-5 (a) and (b) illustrate the behavior of a GM tube with and without particle interaction, respectively. In principle, it depicts two situations in a GM tube output namely, the central anode wire **A** at 1) high voltage and 2) resistive pull-down to zero voltage or ground. Under normal circumstances as shown in figure 2-5 (a), the central wire is left floating and hence the output at the junction of the quenching resistor **R1** [60] and the central conductor **A** is at a high voltage (500 V).

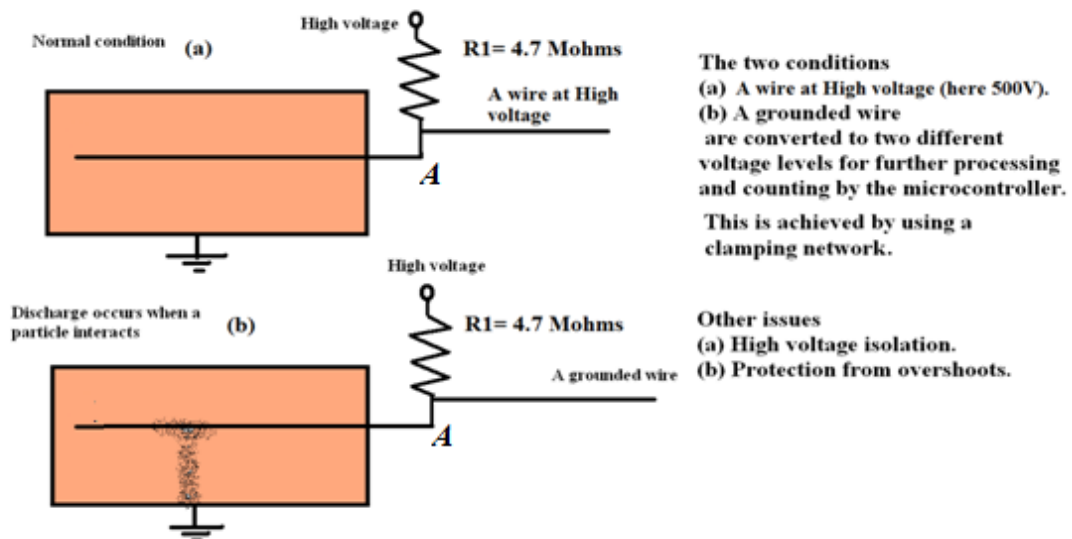


Figure 2-5 Pulse generation in GM tube

Whenever there is an occurrence of particle interaction, ionization of the fill gas takes place, thereby creating a resistive path between the central wire and the chassis, which momentarily pulls down the voltage at the junction towards ground level. The typical values of the lowest resistance attained by the ionized fill gas lie in the range of 80 to 100 M Ω . The voltage swing observed at this junction correspondingly drops down to a minimum value of 475 V before returning to the normal value of 500 V. Figure 2-6 shows a typical snapshot of a GM tube output pulse as seen on an oscilloscope screen obtained on a camera. The anatomy of this pulse is illustrated in figure 2-7.

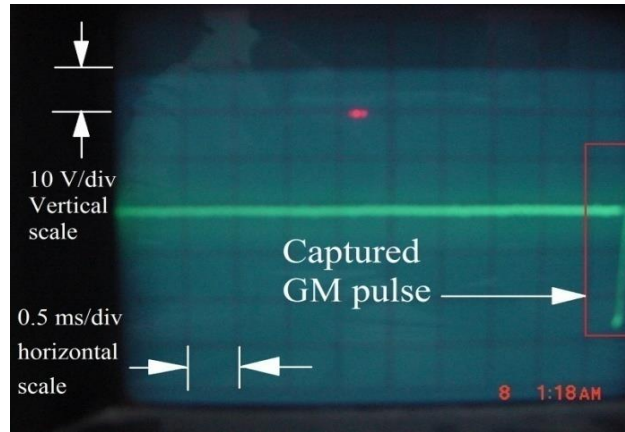


Figure 2-6 Photograph of a GM pulse captured on an oscilloscope

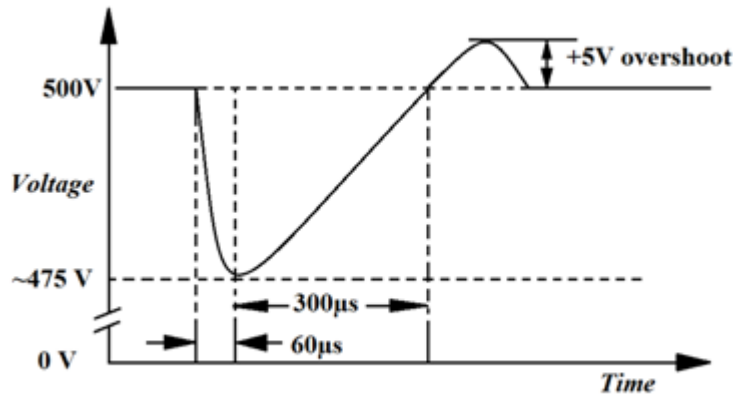


Figure 2-7 Typical time profile of a GM tube output voltage pulse showing a fast 60 μ s rise time. Typical decay time of pulse for the RC components used is 300 μ s with a 5 V positive overshoot

The observed pulse characteristics correspond to those observed generally in GM tubes with similar dimensions [61]. A point to note is that a suitable translation of the high voltage swing is required, so that the dynamic range of the pulse falls within the safe operating limit of the low voltage (LV) counting circuit (figure 2-8). This translation is enabled by employing a comparator that converts the raw analog GM pulse into a TTL logic pulse. Additional issues that need to be addressed are

- (a) High voltage (HV) isolation and

(b) Overshoots due to sudden switching (inductive effect of the central conductor).

The above two issues are generally solved by employing a HV isolation and signal clamping circuit as shown in figure 2-8.

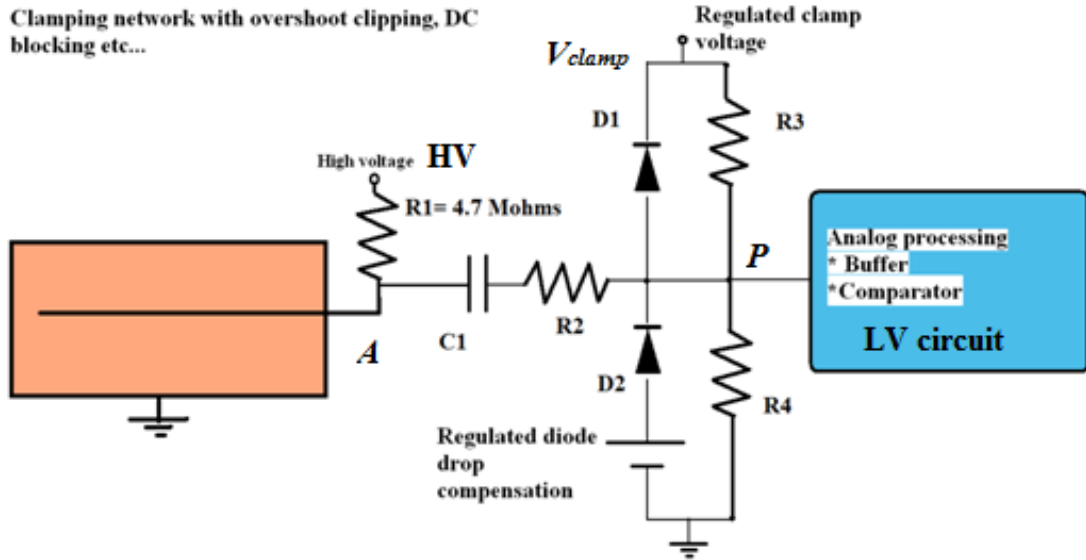


Figure 2-8 General clamping circuit with overshoot protection and high voltage isolation

Provision of HV isolation is ensured by using a low ($<1 \Omega$) impedance for the capacitor, so that it allows the AC signal swing of the GM tube while blocking the 500 V DC. The dielectric breakdown voltage of this capacitor is usually fixed at 1000 V for safe operation.

The resistances $R3$ and $R4$ are used to maintain the LV circuit input P at a known quiescent value usually chosen at the mid-voltage between the power supply rails of the LV circuit. The overshoots present in the signal (figure 2-7) exceed the quiescent level by large amounts ($>5V$) due to the inductive effect. These need to be clipped when they rise beyond the power supply voltage level of the LV counting circuit to ensure its safe operation against over-voltage damage. But in practical designs, the clipping action which is accomplished using diodes is performed at a level (V_{clamp} in figure 2-8) well below the

supply voltage. A lower level for clipping is chosen so that the diode forward voltage drop of 0.7 volts is also accommodated within the supply voltage level.

A positive overshoot of the GM tube signal which rises above 0.7 V from V_{clamp} at the input point **P** is held at and prevented from rising above this level ($V_{clamp}+0.7$ V) by the turning-on of the diode **D1**. The resistor **R2** is added to prevent dead shorting of the GM tube central conductor with the V_{clamp} source or with the ground during a signal overshoot or an under-shoot. The negative excursion i.e. the under-shoot of the signal below ground level is handled by the turning ON of diode **D2**, thereby connecting the GM output to the ground level with **R2** as a resistive load. Usually, a compensatory voltage slightly more than the 0.7V diode drop is added in series with the diode **D2**, to prevent the voltage swing at **P** from going to 0.7 V below ground level.

2.2.2.1 PSoC based Input protection circuitry

In existing designs [38, 39], the clamping voltage sources and isolation network are implemented using a combination of discrete transistors and Op-Amps. Owing to the presence of in-built Programmable Gain Amplifiers (PGAs) in the PSoC-1 I.C., this design uses a simple diode resistor clamping network with PSoC based generation of clamping voltages. In this design, PSoC power supply voltage is selected to be +5V and the clamp voltage V_{clamp} is fixed at 2.5 V. Thus any large positive overshoot excurses only to 3.2V level at the input, which is well below the supply rail of the PSoC chip at 5V. A compensatory voltage of 1V which is slightly more than the 0.7V diode drop is added in series with the diode **D2** to handle under-shoots as discussed earlier.

An amplifier output has the capability to be used as a regulated source for very low current loads; hence, two PGAs are used to get a 2.5V and a 1V regulated source. For the 2.5V source, a PGA is used as an attenuator with the PSoC power supply itself as the signal input. The 1V source is obtained by the same technique using another PGA

module. Thus, the internal PGA modules configured as attenuators (gain settings <1), aid in generating the lower clamping voltage sources than the supply. This is shown in the configuration of the **ACB 02** and the **ACB 03** analog blocks of figure 2-3. In addition to providing regulated voltage sources, the PGAs also provide isolation between the GM output and PSoC supply rail.

For limiting the current drawn from the PGA based regulated sources, the resistors **R3** and **R4** are chosen with a very high value-of the order of a few hundred kilo ohms. In the present design, a 100 K Ω variable resistor **VR3** replaces **R3** and a fixed resistor **R16** of 100 K Ω replaces **R4** as shown in the schematic of figure 2-4. The variable resistor **VR3** was chosen to overcome the limitations in the fine adjustment of the comparator threshold. The resistor **R2** in figure 2-8 prevents dead short of central conductor with either the clamp voltage level or the ground level. Its value is chosen to be 3.3 K Ω . It is to be noted here that this resistor is shown as **R13** in figure 2-4. The design is implemented

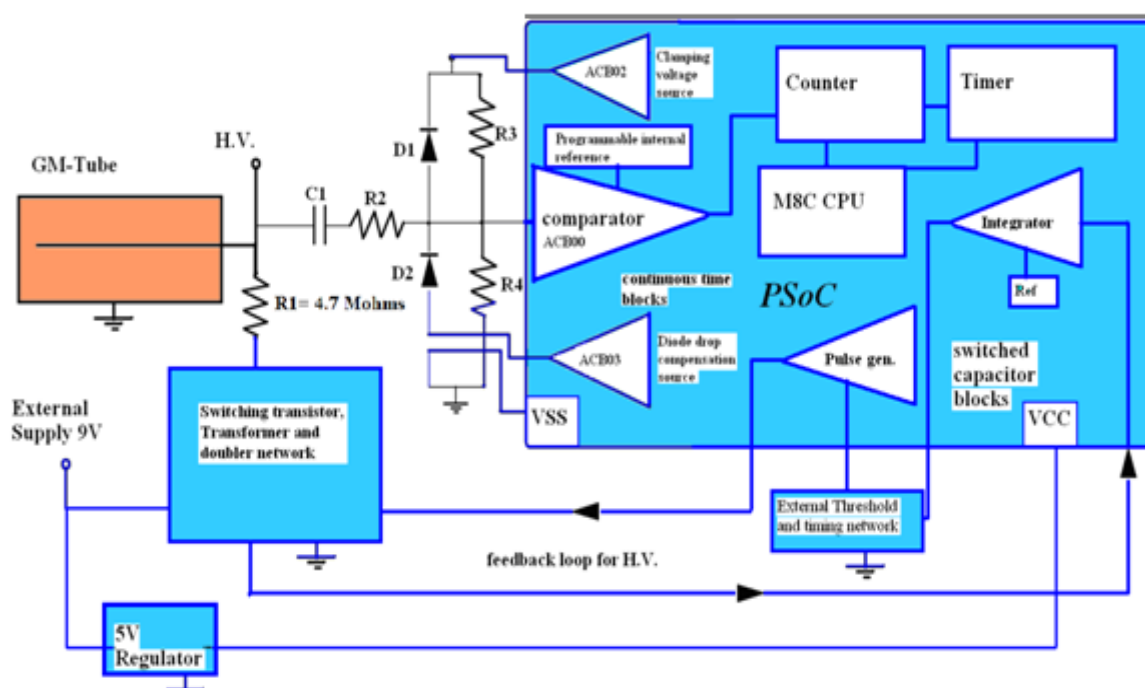


Figure 2-9 On-chip analog PSoC blocks aid in integration of HV regulation modules and the core counting functions on to a single chip

on the PSoC platform in conjunction with other related functions like signal conditioning using comparators and pulse counting. These assist effectively in providing an integrated embedded solution (figure 2-9) to high voltage isolation and overshoot protection issues described using figure 2-5.

2.2.3 Pulse conditioning, dose rate measurement and user interface

The operating principles of pulse conditioning are discussed in this section. The raw analog pulses obtained from the clamping circuit are conditioned to form logic pulses satisfying certain voltage level and timing requirements [57]. In principle, once clamped, the analog pulses are converted to logic pulses using a simple comparator. From figure 2-7, it is evident that the analog pulse waveform performs a downward excursion in voltage, whenever an event occurs in the GM tube. This warrants that a suitable threshold reference level near the positive clamping voltage be chosen for firing the comparator. This generates logic pulses only for sufficiently large GM pulses which rise above the background noise level. The logic pulses thus generated are used for clocking a counter to record the events. All these requirements for signal conditioning are met in this design using PSoC internal blocks. Once converted to the operating levels of the PSoC using the clamping network, the raw analog pulses are then directly fed to a PSoC internal comparator. This generates logic pulses for the internal counter module. The threshold voltage of the comparator in PSoC internal block, **ACB00**, is chosen around 2V from its internal band-gap reference as shown in figure 2-3. The comparator is configured to fire, whenever the falling edge of the pulse signal crosses this threshold.

The parameter and information to be extracted from a GM counter is the counts per second, which directly relates to the recording of events. This is achieved by concurrently running a timer and a counter, the timer being used as a time gating device. Whenever the timer overflows, the current count value is read out and divided by the

elapsed time to get the value in terms of counts per unit time. In this design, the counting of the TTL pulses that correspond to the occurrence of ionizing event, is achieved by using a counter block (**DBB 20**) and a timer block (**DBB 01** and **DCB 02**) configured inside the PSoC chip as shown in figure 2-10. The counter and the timer are started on reset of the PSoC chip. The PSoC CPU core is programmed in such a manner that the timer overflow interrupts are generated for every 20 ms. These interrupts are used to readout the current count value in the counter register and subsequently clear it and reinitialize it.

In a general implementation, communicating the dose rate information to a personal computer (PC) enables both display of measured data and availability of the data to other software applications. Hence, in the current design the measured data is sent to a PC through an RS232 serial communication link. The PSoC chip is programmed such that it periodically logs the dose rate data to the Hyperterminal ® based user interface every second.

2.2.4 PSoC Design and programming

PSoC Designer version 5.1 Integrated Development Environment (IDE)[62] was used for programming this system. The IDE consists of an interconnect viewer and a C compiler. The use of this IDE is limited to the earlier version of PSoC i.e. PSoC-1. The functional hardware testing was done using PSoC-1 In-Circuit Emulator (ICE) and a development board. A screenshot of the development environment is shown in figures 2-3 and 2-10. Its mechanical assembly and the test setup are shown in figures 2-11 and 2-12, respectively.

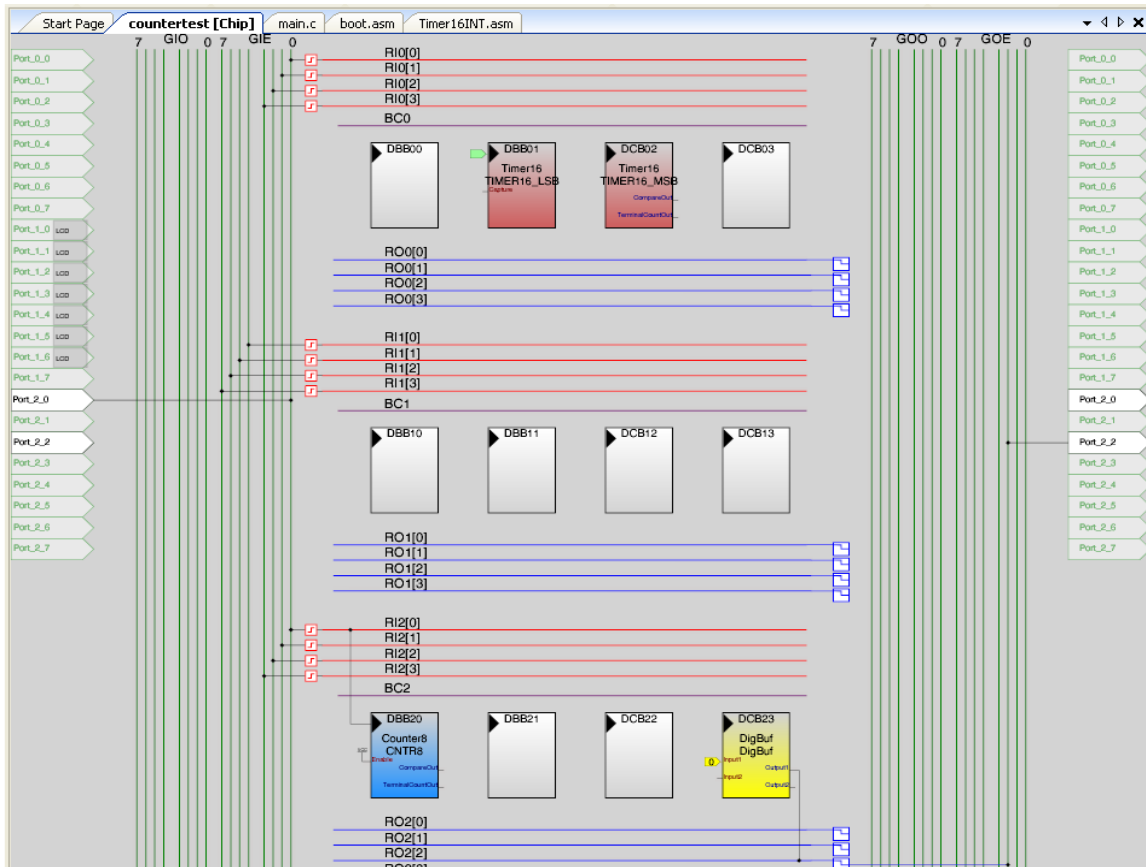


Figure 2-10 Configuration of PSoC digital blocks for GM-counter application

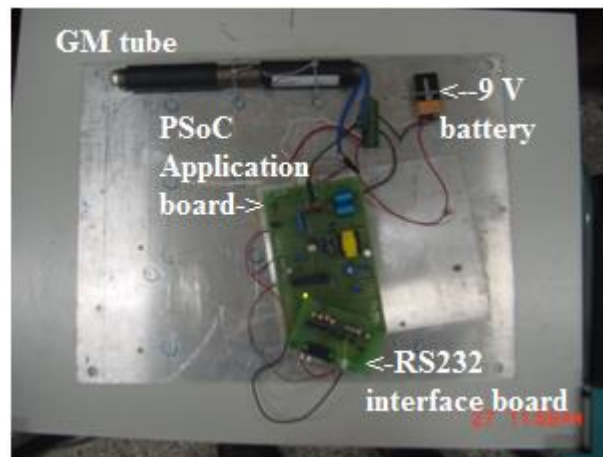


Figure 2-11 Application board mechanical assembly for testing



Figure 2-12 Complete test setup with PC communication accessories and 0.1799 mCi cobalt-60 gamma source

2.3 Results and discussion

The performance of the system was tested for its functionality and calibrated with a 0.1799 mCi Cobalt-60 (Co^{60}) source in the laboratory (table 2-1). As part of calibration, the dose rate variation is emulated using the distance dose rate (\dot{D}) relation given below [63]

$$\dot{D} = \frac{0.005 \times C \times E}{d^2} \text{ Sv h}^{-1} \quad (2.3)$$

where C is the activity of the source in curie (Ci), E is the average energy of the gamma photons released in each disintegration in MeV and distance d is measured in metres (m). In the present report, the theoretical dose was computed for distances varying from 31 cms to 250 cms, to emulate different dose rates in Co^{60} in order to facilitate the system calibration. The theoretically generated dose rate is plotted in figure 2-13 and the instrument sensitivity is deduced from the slope of the linear fit in terms of the observed counts per second for various source-to-detector distances [64]. Satisfactory correlation between theoretically generated curve and experimental count rate clearly indicates the quality of the detection thereby ruling out any significant loss.

Table 2-1 Calibration data of the designed GM counter.

Source to detector distance (cm)	Theoretical dose rate values (nSvh ⁻¹)	Observed counts per second (CPS)
31	23447	344
48	9779	180
68	4873	96
108	1932	40
153	962	20
216	483	11

Moreover, the measured sensitivity is found to be 0.01451 CPS/nSvh⁻¹ from the plotted data (figure 2-13). This implies that for a unit change in the dose rate of 1 mSvh⁻¹, the

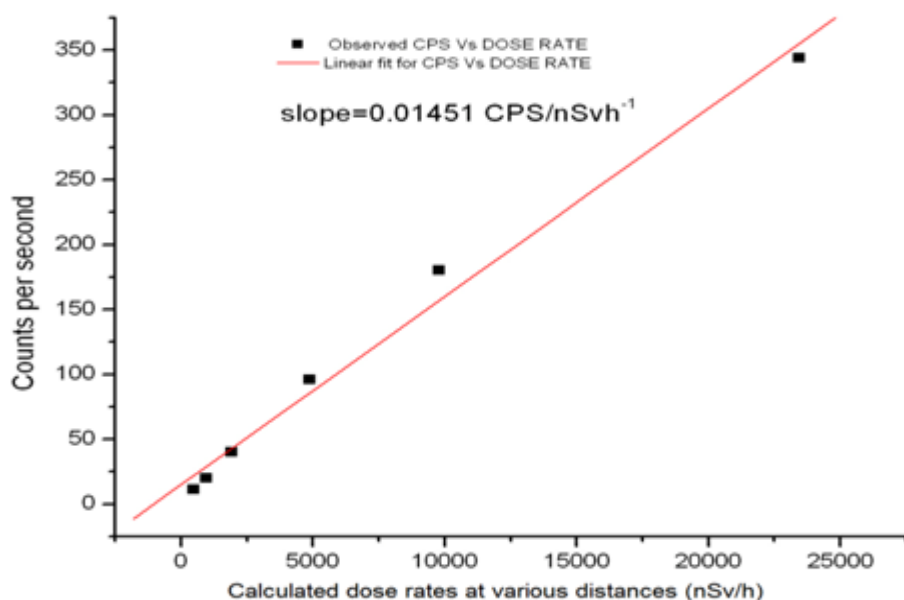


Figure 2-13 Calibration graph with Co⁶⁰ source of 0.1799 mCi. Observed counts are plotted against calculated dose rates

GM survey system registers 14510 pulses per second. This sensitivity is found to be better than that of other commercial systems such as DRM 1 area monitor of “Laurus” make systems with a sensitivity of 1700 Cps/mSvh⁻¹[65], PRM-9000 personnel dosimeter of Mazur make instruments of sensitivity equal to 5830 Cps/mSvh⁻¹[66]. Thus the system developed in this work is a blend of a remote data logging area monitor and a wearable personnel dosimeter. The versatility of the PSoC based design is that, it can be easily adapted to perform the functions of either an area gamma monitor or a personnel gamma dosimeter with minimal or no changes in the system hardware. Regarding the accuracy of the system, it is typically $\pm 10\%$, with a maximum error of $\pm 15\%$ of the typical value and the maximum measurable pulse rate is 15kcps, which corresponds to a maximum measurable dose rate of 1mSvh⁻¹.

Table 2-2 compares other popular commercial gamma survey meters with the present PSoC based system. As is evident from table 2-2, compared to the current commercial models, the PSoC based survey meter design is a low cost and light weight portable design. Although the dose rate range of the present design is orders of magnitude smaller than the commercial versions, its sensitivity in the near background level region (25 nSvh⁻¹ to 25 μ Svh⁻¹) outcores all the other designs. The typical environmental dose rates routinely encountered near an operational nuclear facility are reported in [57]. It can be inferred from the reported values, that during a planned radiological release of Ar⁴¹ from reactors, the maximum dose rates do not exceed 1.5 μ Svh⁻¹. Hence, the current design is best applied as a sensitive tool for emergency preparedness in and around an operational facility. Moreover, the typical alarm level set to detect movement of radioactive materials in portal monitoring applications is around 0.1 mSvh⁻¹. The current instrument is aptly suited for use in such situations as a hand-held frisking device.

Table 2-2 Comparison of design parameters of various brands of gamma survey meters.

Brand	Sensitivity (Cps/mSvh⁻¹)	Weight (g)	Price USD (\$)	Dose rate range (mSvh⁻¹)
Model, 2242 M/s Ludlum Instruments	1915	1300	2826	10 ⁻³ to 9999
DSM-500, M/s WB Johnson instruments	2298	1000	1389	0 to 9999
PRSM-1, M/s Para electronics	2200	800	682	0 to 2
Present PSoC based design	14510	600	200	0 to 1

Added advantages of PSoC based design

It is mandatory that any portable system is very efficient in terms of battery power utilization and adaptable to modern communication interfaces. The present scheme which employs on-chip DMA based waveform generation from PSoC, ensures a longer operation time for the survey meter as compared to other schemes employing blocking oscillator. Further, a simple comparison of features of the above topologies in an energy harvesting application is reported in [67]. It is evident that, the blocking oscillator scheme is advantageous in terms of features like self start up capability and simplicity. But when its efficiency is considered, (~61%) it fares poor compared to that of the present scheme which is around 75% [67, 68].

Many other low cost schemes for generating HV for GM tubes have been reported in literature [69-72]. But, these are either based on COTS HV block [69] or a Villard cascade [70] based topologies, which do not lend themselves to efficient closed loop control as is achieved in the present scheme.

In keeping with current data communication trends which employ high speed USB interfaces in PCs, the present design based on PSoC provides USB 2.0 full speed communication interface in addition to the RS232 interface. This is an added advantage over existing commercial designs such as Model 2242 [38] and DSM-500 [39] in which data communication is based on RS232 only.

The single chip embedded design implementation, is more compact, rugged, and ensures better reliability and accuracy. The stability for this embedded design is excellent, since the high voltage is found to be stable for ~9 hours of continuous operation. Table 2-3 gives the system level specifications of the application board that was developed in this work.

2.3.1 System level specifications of the application board

Table 2-3 System parameters and corresponding values for Portable GM counter

Power supply	9 V alkaline battery (500mAh)
Current consumption of board	60mA
PSoC IC used	CY8C29466
GM tube	Centronic ZP 1221
Instrument sensitivity	0.01451 CPS/nSv/h
Readout terminal	Windows Hyperterminal [®] based readout through RS 232 interface and LCD

The embedded C program for the GM counter application is listed in appendix A.1 of this thesis.

2.4 Conclusions

PSoC based embedded read-out system has been successfully implemented, designed, fabricated and tested with the GM counter and found to be working satisfactorily. The calibration graph in figure 2-13 shows excellent linearity in measurement with the indigenous PSoC embedded design based read-out and regulated high voltage biasing circuit. The functionality of the compact cost effective PSoC embedded GM counter read-out is comparable with commercial bench top models. This demonstrates that any specific application can be implemented in an easy manner as well as effectively in a single silicon chip with this embedded design tool.

CHAPTER 3 PSoC Embedded read-out design for PIN diode based portable alpha particle spectrometer

3.1 Introduction

High resolution alpha spectroscopy is increasingly playing a major role in many radiation measurement applications which include environmental characterization for radiation protection, nuclear fuel cycle, nuclear safeguards and study of geochemical processes. These applications involve the identification of various alpha emitting nuclides and their isotopes present in a sample. The precise location of energy peaks in the spectrum and the determination of the isotopic ratios [21] enable nuclide identification. Hence, the accuracy of the measurements in these applications depends greatly on the quality of the energy spectrum obtained, which is determined largely by the noise performance of the detector and the front-end electronics.

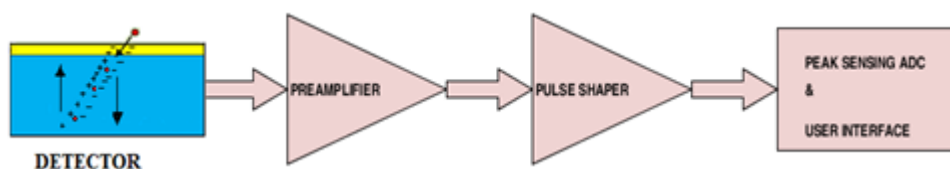


Figure 3-1 General alpha spectroscopy system block diagram showing the detector, preamplifier, the pulse shaping filter and the peak sensing circuits

A general alpha spectroscopy system consists of a detector at the first stage, where particles interact and deposit their energy to generate charge pairs. This is followed by a pre-amplifier and pulse shaper at the front-end, using which energy information is mapped to the amplitude of a voltage pulse (figure 3-1). This chapter describes the design, implementation and performance of an alpha spectrometer in which, a spectral resolution suitable for field measurements is obtained using PIN diode-based detection. Notwithstanding, it provides additional cost benefits by completely eliminating the pulse shaper stage that is mandatorily used in conventional systems for noise elimination and pulse pile-up prevention. This is achieved by utilizing a novel Embedded PulsedResistiveReset (EPRR) technique implemented at the pre-amplifier stage, thereby reducing the total number of high cost analog components. This spectrometer uses a PSoC (Cypress Semiconductor) mixed signal microcontroller platform for both the digitization and embedded reset function. The system design is based on virtual instrumentation and hence, the mixed signal microcontroller platform also performs the data communication with a PC based GUI developed using LabVIEW.

The system level description of the spectrometer is given in the next section. The subsequent sections in this chapter describe in detail, the design and implementation of the frontend, its associated EPRR function and the integration of EPRR with the user interface of the alpha spectrometer. The final section depicts the spectrum obtained from the above topology and the results of the same are discussed.

3.2 Overview of the system level modular design

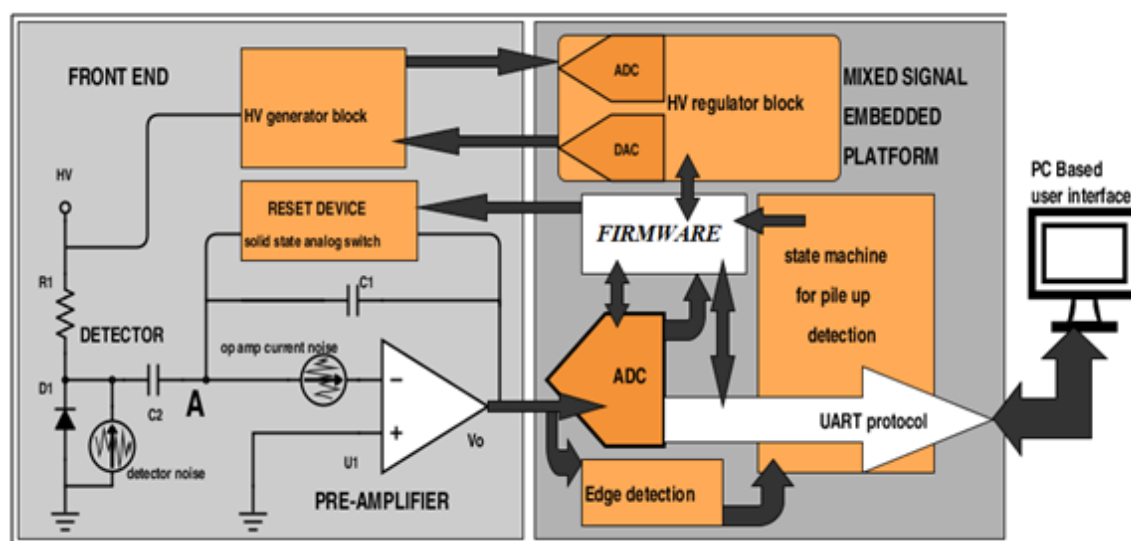


Figure 3-2 Block diagram of embedded pulsed reset alpha spectrometer. The PC with GUI, the mixed signal embedded platform, the front-end comprising a pre-amplifier, a reset device, a HV bias block and the dominant noise sources are shown

Figure 3-2 shows the system level modular design scheme of the spectrometer which consists of three main blocks. The first is the front-end consisting of the detector (D1), pre-amplifier, HV generator for detector bias and solid-state analog switch as reset device. The second block is a mixed signal embedded platform which acts as the interface between the PC and the front-end. It performs various functions like pulse height digitization, pile-up detection and detector bias regulation. The third block is a virtual instrument GUI that provides a console to the user for spectrum viewing and spectrometer control.

3.3 The front-end design

The front-end design consists of various sub-component modules like, the detector, its mount, the HV biasing network and the pre-amplifier. The pre-amplifier design mainly involves the selection of COTS components like the Op-Amp to match the detector characteristics and the reset device.

3.3.1 Detector and its mount

The detector is a planar PIN diode which has a heavily doped shallow p+ and n+ regions on the top and bottom surfaces respectively of a high resistivity n-substrate (a nearly intrinsic- region), originally a part of a silicon wafer (figure 3-3). The bottom n+ layer provides a good ohmic contact between the n-substrate and an additional aluminum metal layer used for biasing the p+ n junction. Radiation interacts in the depletion region formed in the substrate by reverse biasing the p+ n (intrinsic region) junction to produce electron hole pairs. The electric field present in the depletion region sweeps the electrons towards the n+ region and holes towards the p+ region producing a momentary current pulse in an external circuit which is integrated using a charge sensitive pre-amplifier for generating a charge signal. The most important characteristics used while choosing a detector is its shot noise, which arises out of the leakage current through the reverse biased junction [73].

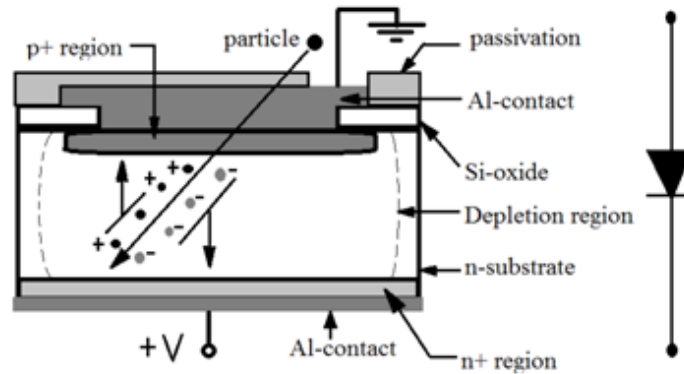


Figure 3-3 Structure of a planar PIN diode with all the important parts being shown

The spectral density of the shot noise current i_{nd} in terms of the reverse leakage current i_d is given by.

$$i_{nd}^2 = 2ei_d \quad (3.1)$$

where, e is the charge on an electron. Since the shot noise is directly proportional to the square root of the reverse leakage current, a device with low leakage current is a good choice. The present design uses a commercial 100 mm² PIN diode (M/s BEL, India) (figure 3-4 inset), which is made from high resistivity (3-5 K ohm-cm) silicon substrate and has a very low reverse leakage current of 25 nA (design value 10 nA) measured at a voltage of 100 V under reverse biased condition and hence a negligible shot noise level [36].



Figure 3-4 The vacuum chamber used in this work and the PIN diode (inset)

The operation of PIN diode for alpha detection warrants two experimental conditions, namely, experiment should be conducted in dark environment and under vacuum. The sensitivity of the PIN diode surface for ambient light and the energy straggling of alpha particles in air necessitates these conditions. A small vacuum chamber (8.5 x 5 x 7 cm) is made which can support a vacuum of 20 torr (~0.002 MPa) [74], while providing a dark ambience for the diode operation (figure 3-4).

3.3.2 The detector bias

The energy range of alpha particles from naturally occurring sources is between 3 MeV and 7 MeV. The alpha energy deposited in the depletion region of the planar PIN diode alone contributes to the external detector signal. Hence, it should be ensured that the width of the depletion region is always equal to or greater than the range of the

highest energy alpha particles (i.e. 7 MeV alpha particles) impinging on the detector. The width of the depletion layer varies with respect to the detector reverse bias[73]and its value is estimated from the detector capacitance measurement using the relation

$$C_d = \epsilon A/d \quad (3.2)$$

where, C_d is the detector capacitance in Farads (F), ϵ is the dielectric constant of silicon material (F/m), A is the area of the diode (100 mm²) and d , the depletion width (m).The variation of depletion width with respect to the reverse bias for the M/s BEL PIN diode used in this work measured experimentally using an LCR meter (M/s Agilent E4980A) at 1 kHz is shown in figure 3-5.

It is estimated from the capacitance values in the figure that for an unbiased diode (0 V reverse bias), the depletion width is typically ~1 μ m and is very less compared to 45 μ m, which is the approximate range of 7 MeV alpha particles in silicon.

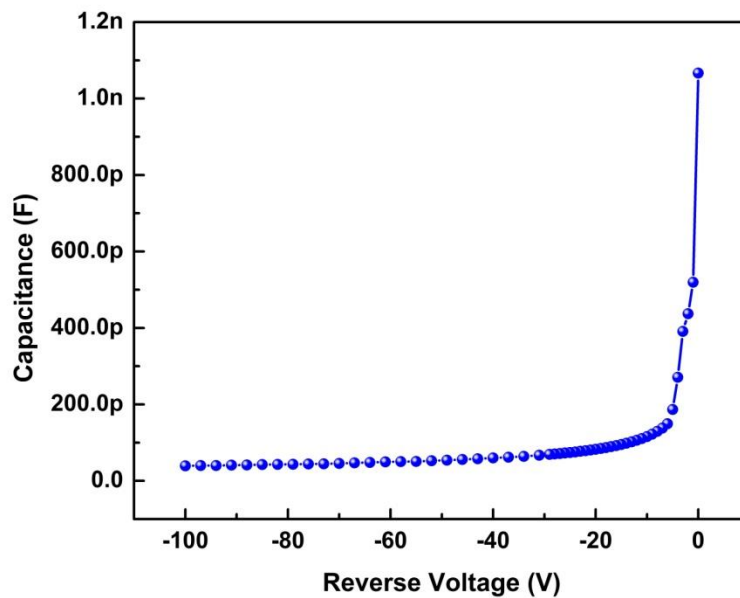


Figure 3-5C-V characteristics of the M/S BEL PIN diode

The depletion width increases and reaches the desired value of 45 μ m at a reverse voltage of ~3V. However, we see that the depletion width corresponding to this voltage is

not the stable terminal depletion width of $\sim 260 \mu\text{m}$ estimated from the 40-pF capacitance value attained at 100 V reverse bias. Moreover, at a reverse bias of 3 V, the depletion width is very sensitive even to small variations in the bias voltage. The bias voltage of 100V has been chosen for the detector operation to maintain a stable large depletion width with respect to drifts in bias voltage and thereby ensure complete energy deposition for highest energy alpha particles.

The generation of high voltage bias, is achieved through a Pulse Width Modulation (PWM) based DC-DC boost converter. The analog regulation network for the boost converter is implemented using on-chip user modules of the embedded hardware platform, whereas the converter itself is placed externally, comprising of a switching transistor, passive filter and a pulse transformer [75]. One of the primary concerns in a high voltage bias system for radiation detectors is that, any fast transients in the bias voltage would permanently damage the input FET of a pre-amplifier due to transient current spikes [76]. Hence, a safe 5V/s ramp in high voltage, during system turn on and turn off is achieved by varying the reference voltage of the DC-DC converter loop using a dedicated internal Digital to Analog Converter (DAC) and a timer. Conventional designs use high-quality Silicon Surface Barrier (SSB) or Passivated Implanted Planar Silicon (PIPS) semiconductor detectors in the first stage [77, 78]. These detectors are operated with Application Specific Integrated Circuit (ASIC) or discrete hybrid pre-amplifiers and shapers to get best results in terms of resolution, thereby rendering them expensive. However, for most radiation measurements in field applications, portability and cost are the important deciding factors [79].

3.3.3 The preamplifier design

Owing to the recent availability of low cost, high performance Op-Amps, the efforts on front-end design for portable radiation measurement systems is increasingly being

centered around the choice of the best COTS functional blocks. COTS amplifiers have hitherto been employed in pre-amplifier designs for CdTe detector[78, 80] (figure 3-6 (a)) to obtain high resolution gamma spectroscopy and considerable cost reduction. The capacitance and leakage current characteristics of Si PIN diodes are comparable to CdTe detectors (~100pF for a 21.5 x 21.5 x 0.5mm area CdTe detector)[81]. Hence, in this work, an existing pre-amplifier design for CdTe detector has been adopted with requisite modifications for alpha detection using Si PIN diodes. COTS Op-Amp based circuits [80-82] eliminate the dependence on expensive ASIC or discrete component based hybrid circuits, which additionally involve substantial circuit design time and complexity in its optimization[83].

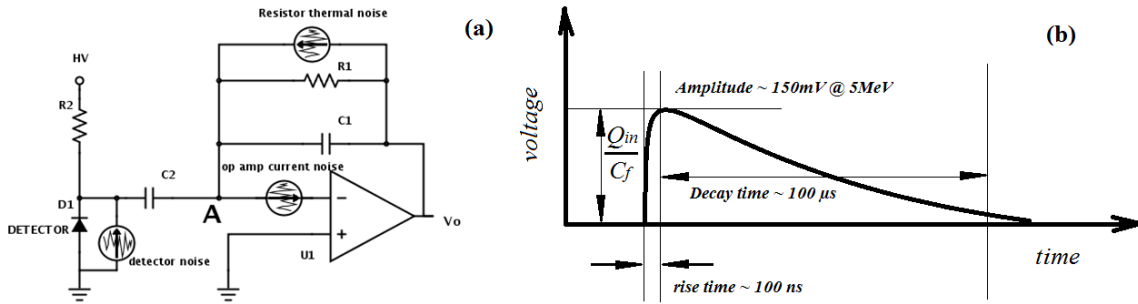


Figure 3-6(a) The pre-amplifier configuration with the dominant noise sources and (b) a typical tail pulse output with the resistive reset scheme

The configuration of the pre-amplifier stage designed in this work is a charge sensitive one in which, the output is a voltage tail-pulse signal as shown in figure 3-6 (b). The step height of the tail-pulse corresponds to the charge generated by an alpha particle in the sensitive region of the detector. The charge sensitivity or the charge gain which is the pulse height voltage per unit charge generated is given by

$$Gain = \frac{1}{C_f} \quad (3.3)$$

In this design, a feedback capacitor (C_f) value of 1pF is chosen which corresponds to a charge sensitivity of 1V/pC. It is to be pointed out that the capacitance and leakage current characteristics of the input FET had been a prime consideration for the choice of Op-Amp. The charge sensitive pre-amplifier design is matched to the detector using two main detector characteristics namely, C_d and i_d based on the data obtained from the C-V characteristics shown in figure 3-5 and the measured reverse leakage current at 100 V. This has been experimentally verified in the gamma spectroscopy application for which it was originally designed [78]. The approach employed for CdTe detectors has been adopted in this present work.

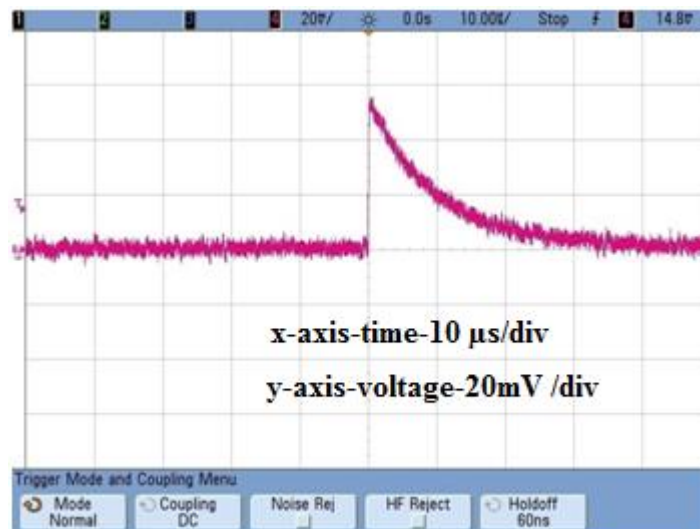


Figure 3-7 Preamplifier output with standard resistive reset scheme with a feedback resistor of 10M Ω . The pulse decays to ground level within 30 μ s

The output pulse obtained from the pre-amplifier for a 5486 KeV alpha particle from an Am-241 source is shown in the figure 3-7 above. This design uses the commercially available OPA 656 Op-Amp from Texas instruments [84] owing to its salient design capabilities. Its features comprise a 500 MHz wide stable unity gain bandwidth, a FET input stage enabling very low input bias current of 2pA, a very high input impedance and an ultra-low input voltage noise power density of 7nV/ $\sqrt{\text{Hz}}$. These features make it the

best choice for an ultra-low noise charge sensitive pre-amplifier for alpha spectroscopy. In a standard pre-amplifier design, the charge accumulated on C_I is discharged through a parallel resistor R_I . This prevents pile-up of pulses from radiation events closely spaced in time, thereby reducing errors in output pulse height measurement.

R_I values in the range of 10 M Ω to 100 M Ω are commonly used for moderately quick discharge (~ 50 μ s). Such low resistance values are ideal for quick discharge of capacitor resulting in reduction of pulse pile up. But, the level of thermal current noise in the input node is increased by low resistance values. The power spectral density of the feedback resistor current noise i_{nR}^2 is inversely proportional to the resistance value R_I as shown in equation (3.4).

$$i_{nR}^2 = \frac{4kT}{R_1} \quad (3.4)$$

Where k is the Boltzmann constant and T is the absolute temperature. It is clear from equation (3.4) that R_I should be maintained at a very high value (\sim G Ω), to ensure noise reduction. However, maintaining the high value for R_I for long durations increases the chances of pulse pile up. The above two conflicting requirements have been met in the present design by utilizing a special reset scheme.

3.4 Embedded pulsed reset function

To meet the two conflicting requirements of reduction in pulse pile up error and thermal noise simultaneously, a conventional solution is to use a pulsed resistive reset technique [85-91]. As shown in figure 3-8, in this technique, R_I is replaced with a reset device which is usually an optical switch, a transistor or a CMOS solid state analog switch. The operation sequence of this technique is explained as follows. During acquisition of radiation events (duration from start of **T1** to the start of **T3** in figure 3-9),

the reset device is turned OFF to function as a very high resistance path. The output in this condition is a series of positive rising voltage steps with reduced thermal noise levels. The high resistance condition of the switch is maintained until the output eventually crosses a voltage threshold to quickly reach saturation near the supply rail of the pre-amplifier. The moment the threshold is crossed, the output of the pre-amplifier triggers a voltage comparator with the same voltage threshold to fire momentarily. The comparator output is utilized to turn ON the reset device to function as a momentary (start of **T2** to end of **T3**) low resistance path. This quickly brings both the saturated pre-amplifier output and the voltage across C_1 to the zero base-line so as to begin the next cycle of radiation event acquisition.

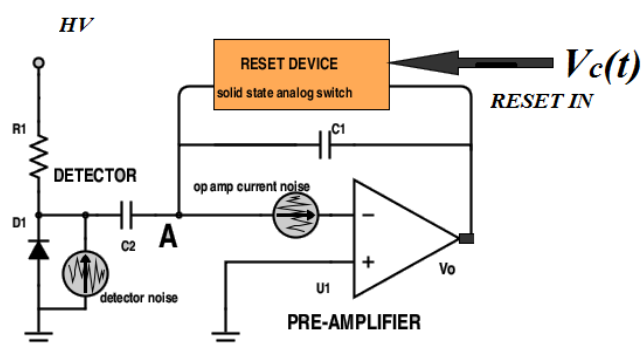


Figure 3-8 The basic preamplifier circuit with the feedback replaced by an analog switch

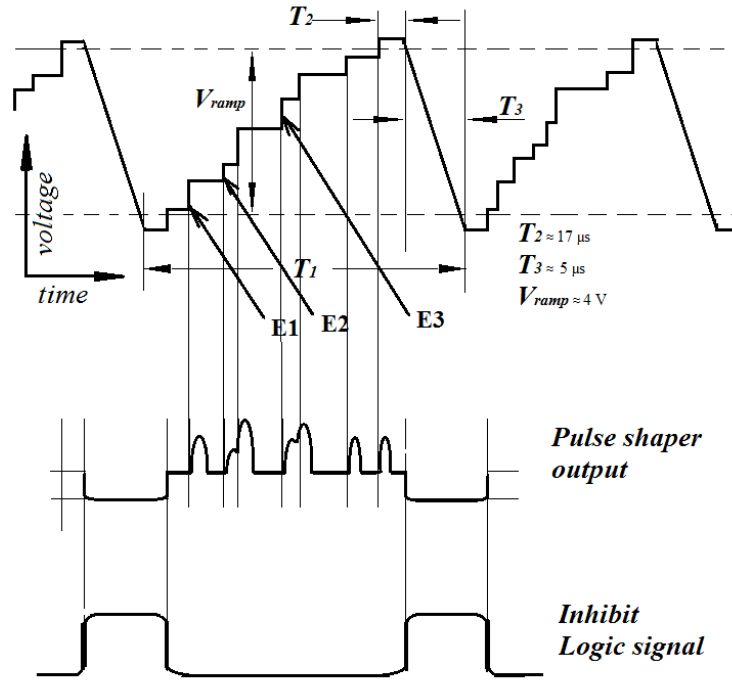


Figure3-9 Output staircase waveform of pulsed reset pre-amplifier. The corresponding pulse shaper output and inhibit logic waveforms are also shown

The pre-amplifier output waveform in a pulsed resistive reset configuration is a staircase of voltage steps instead of a train of tail-pulses as obtained in a standard configuration. Though this is advantageous in terms of noise, it makes all the pulses to get piled-up causing errors in pulse height measurement. This problem is dealt with by a pulse shaping amplifier stage in the signal processing chain. The pulse shaping amplifier converts the pre-amplifier's staircase output into a train of gaussian pulses. The amplitudes of these pulses are kept proportional to the step heights in the staircase and the duration of the pulses lie in the order of the rise time of pre-amplifier output steps. This ensures a reduction in error peaks in the spectrum corresponding to the piled-up pulse heights. The pulsed reset pre-amplifier warrants two additional modules in the signal chain: One, the generation of inhibit logic and the other, a gate element at the input of pulse shaping filter. The gate element controlled by inhibit logic prevents any momentary large negative polarity pulse at the pre-amplifier output from entering the pulse height

digitizer. This prevents the registration of an erroneous pulse height value in the system. The pulse shaping amplifier, the inhibit logic and the gate element can be eliminated altogether by using a modified pulsed resistive reset scheme. The present design explores an Embedded Pulsed Resistive Reset (EPRR) technique which is a modified version of the conventional pulsed reset. In this technique, the momentary resistance switching to the low value extreme in the feedback path is performed immediately after every rising edge (**E1**, **E2**, **E3** etc... in figure 3-9) in the pre-amplifier output. This is in contrast to the existing pulsed reset technique, in which resistance switching to the lower limit occurs only after a series of events that lead to pre-amplifier output saturation (start of **T3**).

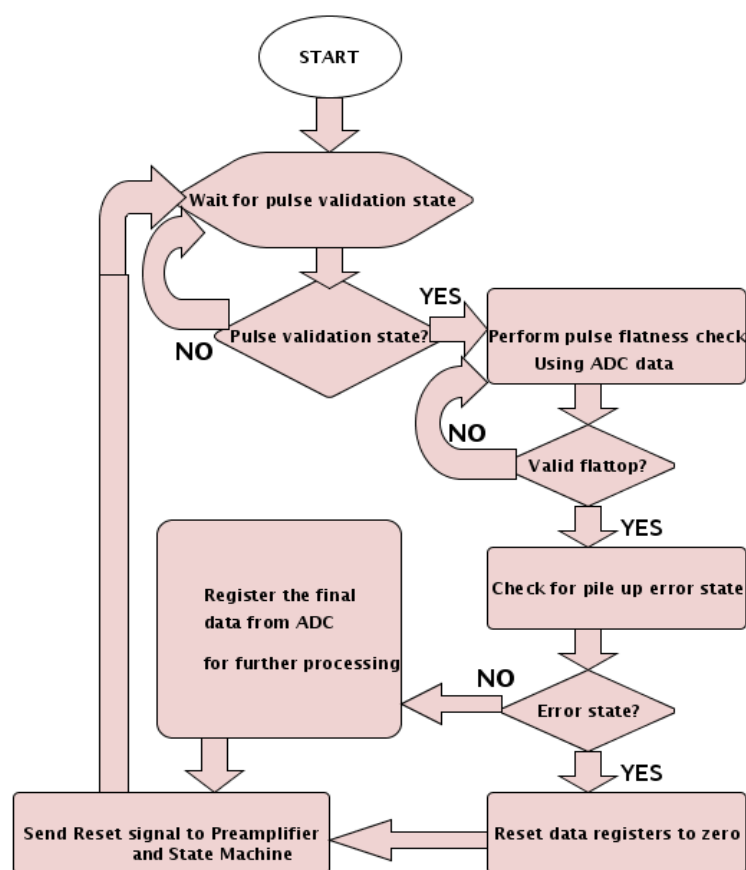


Figure 3-10 Flow chart of the Firmware operation running in parallel with a state machine in the embedded pulsed reset scheme

In the modified technique, a CMOS analog switch is used as the feedback element which is controlled by a unique firmware generated reset signal from a mixed signal microcontroller platform. This technique is described in the flow charts of figures 3-10 and 3-11.

While the conventional scheme uses pulse duration reduction to prevent pile-up errors, the EPRR scheme uses the pile-up detection and elimination technique [86]. In this design, both the pile-up detection and elimination function are executed using a simple state machine which operates in conjunction with the firmware. This is achieved by real-time intimation of pile-up events to the firmware utilizing its own reset signal and an external timing signal from the pre-amplifier. The operation of the EPRR function is best understood by the concurrent description of both the firmware (figure 3-10) and state machine operation (figure 3-11).

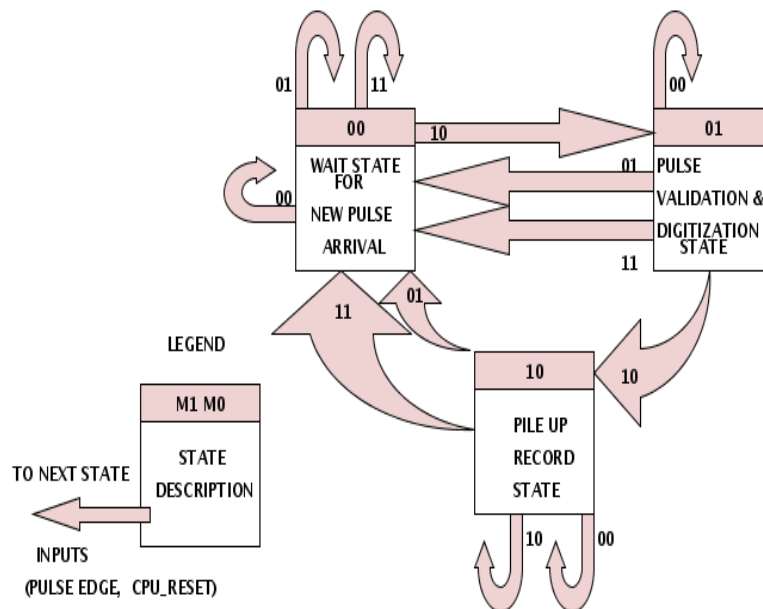


Figure 3-11 State machine for detection of pulse pile up during digitization

The flow chart of figure 3-10 describes the sequence of operations executed in the firmware. The firmware operation is controlled by the state transitions that occur in an

independent simple state machine working in parallel to the firmware (figure 3-11). Two external digital signals labeled the PULSE EDGE and the CPU_RESET control the state transitions of the state machine. The PULSE EDGE (**PE**) signal is generated by an edge detection circuit in the output of the pre-amplifier and corresponds to the occurrence of the pre-amplifier output rising edge. The CPU_RESET (**CR**) signal is generated by the firmware after completion of each digitization operation. The logic variables **M1** and **M0** describe the current state of the state machine. As shown in table 3-1, three states are identified in this design.

Table 3-1 State variables and their corresponding state descriptions

SYMBOL	STATE DESCRIPTION	M1	M0
W	Waiting state for new pulse arrival.	0	0
PVD	Pulse validation and digitization state.	0	1
PR	Pile up record state.	1	0

The wait state (**W**) forms the initial state of the state machine. The only transition allowed in the **W** state is the transition to the pulse validation and digitization (**PVD**) state. This transition occurs provided that a pulse edge at the pre-amplifier output is detected, thereby asserting the **PE** signal and that the firmware has not generated a reset, maintaining a negated **CR** (**PE**=1, **CR**=0). Any other combination of **PE** and **CR** keeps the state machine continuously in the **W** state. Once the state machine finds itself in the **PVD** state, there exists two possible state transitions viz. a transition back to the **W** state or a transition to the pile-up record (**PR**) state. The former occurs irrespective of the presence of a pulse edge when the firmware asserts the **CR** (**PE**=1 or 0, **CR**=1). The latter occurs when an assertion occurs in the **PE** signal with the **CR** signal negated (**PE**=1, **CR**=0). Finally, the only transition allowed from the **PR** state is, to the **W** state which occurs when **CR** is asserted irrespective of the **PE** signal (**PE**=1 or 0, **CR**=1).

Referring to the figure 3-10, when the system is initialized (START), the firmware and the state machine find themselves in a waiting state (WAIT FOR PULSE VALIDATION STATE) for new pulse arrival. They continue to remain in this state until the **PE** signal triggers a change. The **PE** signal brings the State machine to the **PVD** state. The firmware concurrently enters an Interrupt Service Routine (ISR). In the ISR, the firmware ascertains that a flat top in the signal has been reached (PERFORM PULSE FLATNESS CHECK). This is done by comparing the successive values of an Analog to Digital Converter (ADC) to which the pre-amplifier output signal is fed. The details of the ADC used in this scheme are given in the next section. Once the flat top is ascertained, the firmware records the current value of ADC. While it is engaged in the digitization process, the state machine is free to respond to its inputs independent of the firmware.

Immediately after completing the digitization process, the firmware probes the **M1** and **M0** signals of the state machine to gauge its current state. If the current state read by the firmware is still the **PVD** state, the firmware registers the final recorded value of the digitizer (REGISTER THE FINAL DATA FROM ADC) as a valid pulse height and then asserts the **CR** signal. But, if the current state read is the **PR** state, the firmware discards (RESET DATA REGISTERS TO ZERO) the final recorded value of the digitizer prior to asserting the **CR** signal (SEND RESET SIGNAL TO PRE-AMPLIFIER AND STATE MACHINE). This is because the transition to the **PR** state is an indication of a pile up event that has occurred during the pulse validation and digitization process in the firmware and hence will cause an erroneous value of a pulse height to be recorded. The subsequent assertion of the **CR** signal marks the end of one pulse digitization cycle as both the state machine and the firmware find themselves once again in the initial wait state. The same **CR** signal generated by the firmware to bring the state machine back to

the initial state is used to trigger the discharge of feedback capacitor in the pre-amplifier. This is achieved by using it as the trigger signal to turn ON the CMOS analog switch.

The proper functioning of the EPRR scheme is critically dependent on the time profile of the state machine clock and the Pulse Edge (PE) signal. The PE signal marks the time for each alpha interaction event in the detector and its ON-time duration relative to the state machine clock is as shown in figure 3-12.

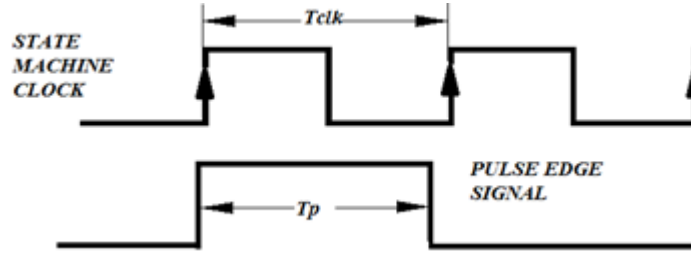


Figure 3-12 The timing constraint on the PE signal

Any implementation should ensure that the duration of assertion T_p of the PE signal does not exceed a single period of the clock signal T_{clk} used to run the state machine. However, it should also ensure that this duration is long enough for exactly a single clock edge to detect it. Hence, the condition,

$$T_p \cong 0.9T_{clk} \quad (3.5)$$

should be maintained, to ensure that the state machine does not erroneously skip the PVD state and find itself directly in the PR state, even without a pulse pile-up condition. The satisfaction of equation (3.5) in the design, demands the availability of a jitter-free clock and a high-speed comparator on a single platform. Further, the EPRR scheme demands a hardware platform which facilitates concurrent functioning of two modules - a simple state machine and a firmware to run in a high-speed Central Processing Unit (CPU).

The EPRR scheme can be implemented using conventional microcontrollers in combination with COTS analog and digital integrated circuits. But, this option poses design challenges in the form of the final system size. Moreover, the inclusion of other

peripheral functions like high voltage regulation and data communication in the design as stand-alone modules introduces interference related errors. These errors are caused by pickups in the long signal routing traces between various modules. One other possibility is the use of high-end field programmable gate arrays (FPGAs). But this drastically increases the cost for a portable system. Hence, there is a need for a mid-path programmable hardware which is both cost effective and has features for a high-resolution portable spectroscopy system.

The PSoC platform from Cypress Semiconductor Inc. is a unique mid end hardware platform which enables concurrent implementation of both the EPRR scheme and the peripheral spectrometer functions. Hence, the PSoC platform is used in this design.

3.4.1 PSoC- 5 platform features

PSoC is a software-configured mixed signal array with a built-in Microcontroller Unit (MCU) core. A PSoC IC has a CPU core, configurable analog and digital blocks, Programmable Logic Device (PLD) based customizable user modules, all integrated on a single chip. PSoC 5 LP is a latest version and has a 32-bit ARM® cortex M3 processor core with up to 80 MHz speed. In this work, IC CY8C5868 AXI LP035 device is used as the basic platform. PSoC creator 3.0 IDE, and Cypress Joint Test Action Group (JTAG) programmer were used for designing and programming the application board.

The core functions of the spectrometer namely, the firmware and the state machine are run in the high-speed CPU and the PLD area, respectively. The interconnections of the on-chip user modules to perform the peripheral as well as the core functions are depicted in figures 3-13, 3-14 and 3-15. Figure 3-13 shows the interconnections of the on-chip PSoC blocks to implement the high voltage regulation and ramping functions required for the detector bias. The high voltage regulation in this system is done using a switched

mode scheme [75]. While the switching transistor and the transformer of the boost converter are implemented as external elements along with the high voltage feedback filters, the active components are implemented using on-chip modules. Further, the

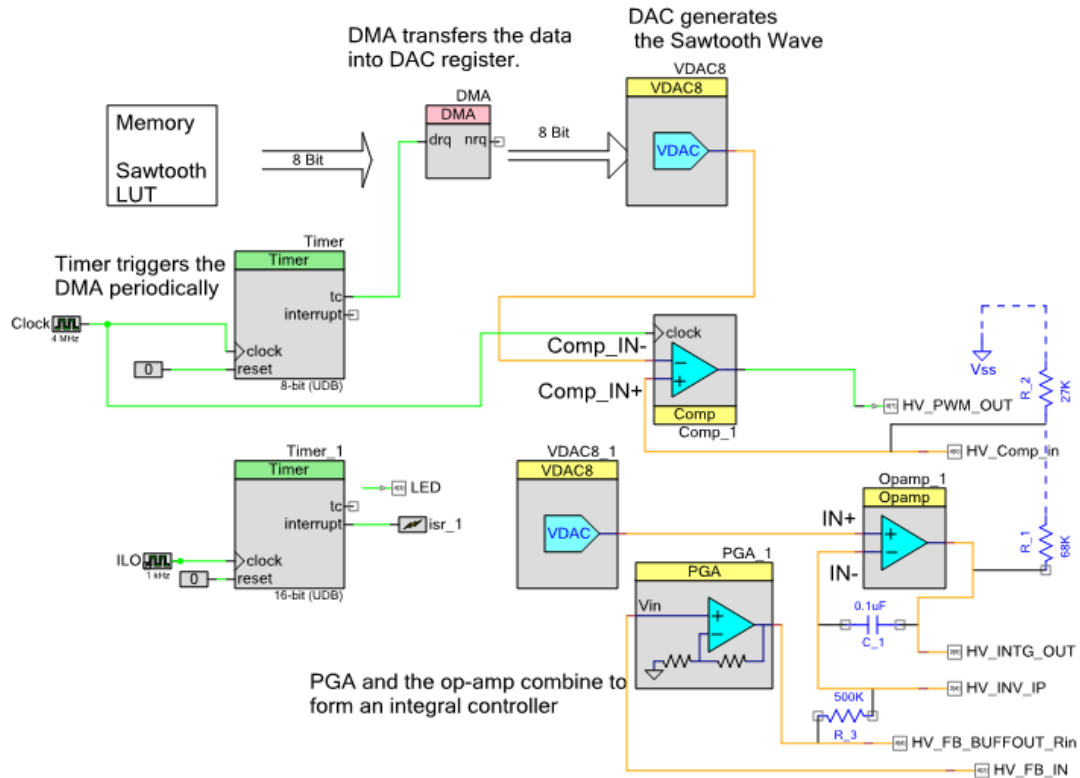


Figure 3-13 The PSoC creator schematic for the on chip high voltage ramping and regulation module

VDAC8_1 DAC module acts as the reference voltage generator for the HV system and hence, its output is fed to the non-inverting input (IN+) of an integrator. The internal Op-Amp OPAMP_1 is configured as the integrator to which a fraction of the output HV is given as feedback to the inverting input (IN-). The integrator output is either a positive or a negative voltage ramp and is determined by the sign of the HV output error. This ramp signal is fed to a comparator COMP_1 at its COMP_IN+ input. This comparator compares this slow ramping signal to a saw tooth waveform fed at its COMP_IN- input to produce a PWM signal (HV_PWM_OUT). This PWM signal is given to an external

switching transistor (see figure 2-2) of a regulated HV loop similar to that described in section 2.2.1. The saw tooth waveform essential for the PWM signal is generated in this system by periodically dumping data from a Look-Up-Table (LUT) into a DAC module VDACC8. This is done using direct memory access (DMA) transfer. The use of DMA technique ensures that the waveform generation is CPU independent. The trigger signal for periodic DMA transfers is generated by the timer module labeled TIMER. The HV ramping function is implemented by internally ramping the VDACC8_1 DAC using the interrupt generated by the timer module TIMER_1. This enables the firmware to increase the DAC data value during system startup and shut down.

The state machine function is implemented using the on-chip D-flip-flops and logic gates as shown in figure 3-14. The two input signals fed to the state machine -the CPU_RESET_IN and POS_EDGE_IN correspond to the **CR** and the **PE** signals, respectively, that are used in the state machine description.

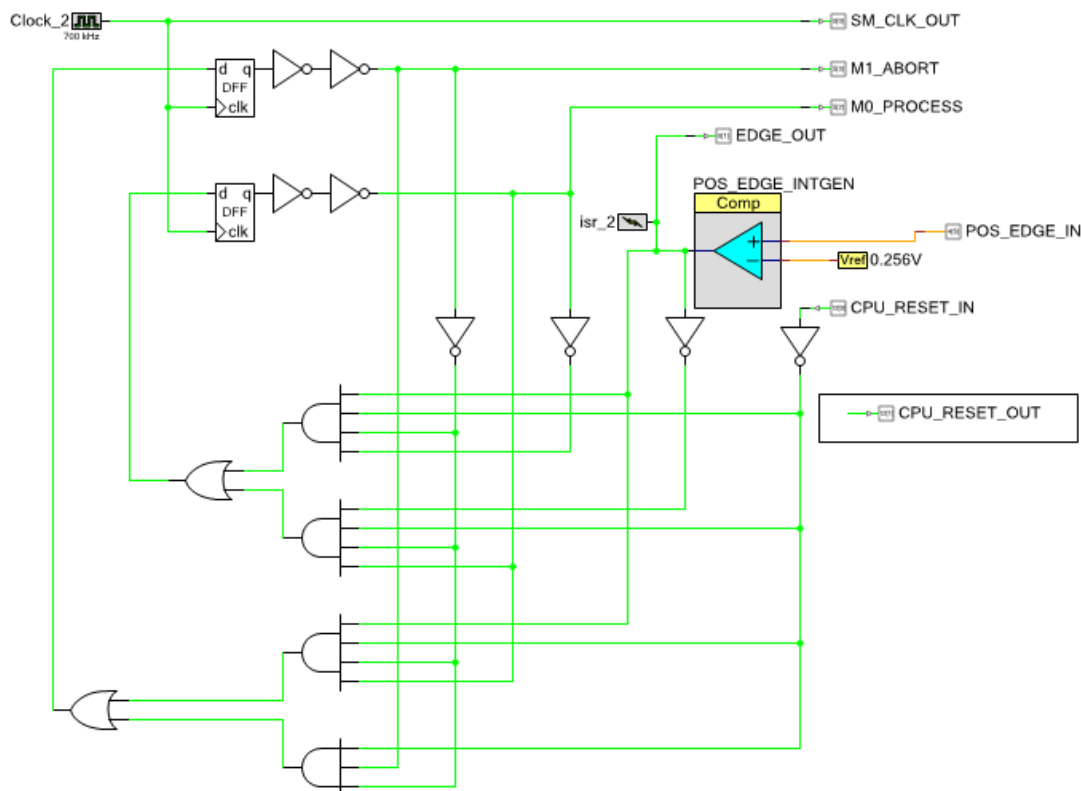


Figure 3-14 PSoC creator schematic for the on-chip State machine module

While the former is fed directly, the latter which is generated from an external transformer-coupled edge detection circuitry in the pre-amplifier output undergoes a prior conversion to Transistor-Transistor Logic (TTL) level. The level conversion is done using an internal high-speed comparator ‘Comp’ with a 250-mV internal reference. The clock of the state machine is chosen in accordance with the duration of the shortest possible logic pulse obtained for the **PE** signal. The output signals of the state machine are M1_ABORT and M0_PROCESS.

The digitization and data communication functions are implemented using an on-chip delta-sigma ADC- ADC_1 and universal asynchronous receiver transmitter (UART) UART_TX_1 module, respectively. Figure 3-15 shows the implementation of this function in the PSoC IC. The delta sigma ADC is used at either 12-bit or 14-bit resolution configured using software at a maximum sampling rate of 250 Ksps.

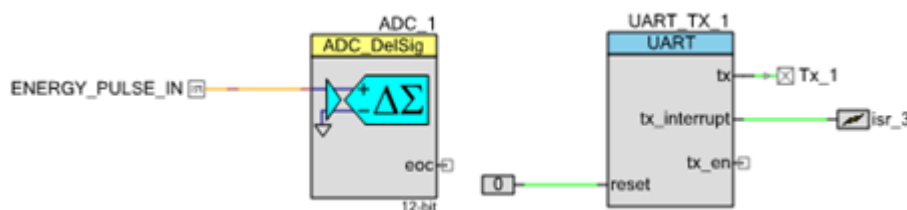


Figure 3-15 PSoC schematic for the on-chip digitizer and UART communication modules

3.4.2 Reset device

The following are the considerations for the selection of the reset device which are the same as in the design of a conventional pulsed reset pre-amplifier.

- (a) The OFF-state resistance (5 to 10 G Ω) for very low thermal noise
- (b) The ON state resistance (10 to 100 Ω) for quick discharge.
- (c) The switching speed.
- (d) The charge injection level, which is most important.

Several devices were considered and compared based on the above-mentioned parameter values, for use as the reset device. The switches considered are listed in table 3-2.

The charge injection is the introduction of a small amount of charge into the substrate/channel of an analog switch from the control input terminal. It is a very critical parameter while using analog switches in precision applications like charge pre-amplifiers. This phenomenon occurs due to the presence of stray capacitance between

Table 3-2CMOS analog switches with design parameters considered for the reset function

Sl no .	DEVICE	OFF Leakage current @ channel voltage difference	Charge injection	Turn-On Turn-Off time	Package option
1.	ALD 4211	100pA @ 4V	1pC max	130ns	16 pin SOIC
2.	Vishay-DG636	0.1nA @ 10V	0.1pC max	60ns	14 PIN TSSOP
3.	Vishay-DG9233	100pA @ 1 V	5pC max	120ns	8-PIN SOIC
4.	MAX 4594 (Used in present work)	0.5nA @ 3.5V	5pC max	40ns	5-PIN SOT-23

the control electrode and the channel. The ideal charge injection level should be zero; nevertheless, practical devices show a non-zero charge injection in the range of 1 to 5pC which can be eliminated through indirect methods. The present design uses a MAX 4594 analog switch [92] to implement the reset function which has an extremely high OFF state and low ON state resistance of $\sim 7 \text{ G}\Omega$ and $\sim 10 \text{ }\Omega$, respectively. The switch has a moderate charge injection of 5pC. Though the charge injection in this device is high compared to the other available switches, its high switching speed and small package size outweighs all the other parameters, making it an ideal choice.

3.4.3 Switch control signal characteristics

In order to reduce the effect of charge injection to negligible levels in the pre-amplifier output, a novel profile shaping scheme is employed in this design for the control signal $V_c(t)$ (figure 3-8) of the reset device. This scheme works on the principle that the injected current i_{inj} is proportional to the rate of change of the control signal and hence, can be reduced by its slow ramping during the switching instant. The coupling between the channel of the reset device and the control input pin is capacitive. Hence,

$$i_{inj} = C \frac{dV_c(t)}{dt} \quad (3.6)$$

where C , is the stray capacitance between the channel and the control pin and $dV_c(t)/dt$ is the rate of change of the control signal. Since $dV_c(t)/dt$ value at the rising and the falling edges of the switching waveform is large, the charge injection is more profound at these instants; hence, slow ramping of edges in the control signal is a necessity. However, in mid-end platforms like PSoC, the slope control of both the edges for slow ramping is severely restricted. Hence, a modified slow ramping scheme is evolved by studying the charge injection effect in the pre-amplifier output. This ramping scheme thus evolved can easily be implemented in the PSoC platform. Figures 3-16 and 3-17 show the experimentally observed charge injection effects with two different switch control waveforms. In both the cases, the switch control signal $V_c(t)$ is generated using a function generator. In figure 3-16 $V_c(t)$ is given in burst mode. In this mode, the channel resistance of the reset device changes from tens of Giga-ohms in the OFF state to tens of ohms in a very short time (typically 1 μ s). The burst mode also prevents the output from swinging

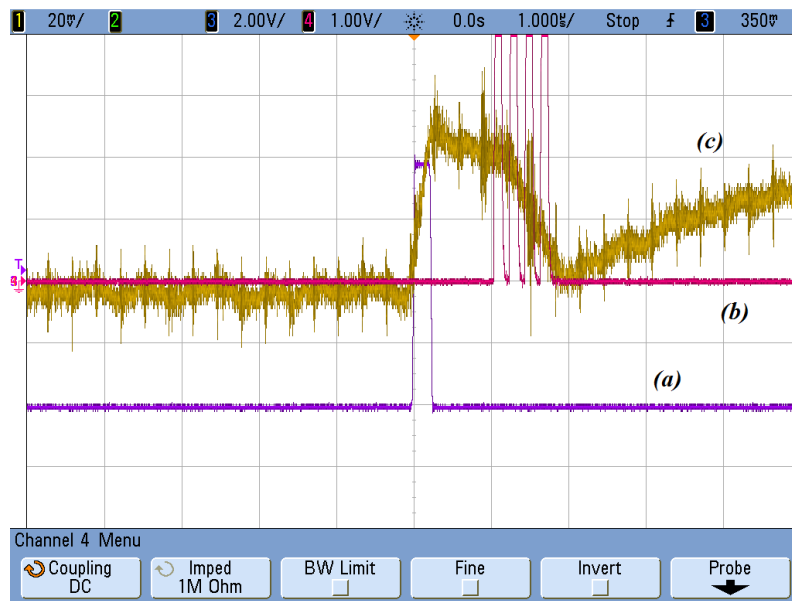


Figure 3-16 Preamplifier output (c) shown along with the Pulse Edge signal (a) and the burst mode reset signal (b)

to the negative side due to zero average injected current. This is due to the fact that the response time of the channel is much slower than the switching speed of the control signal, thereby making the average injected current zero.

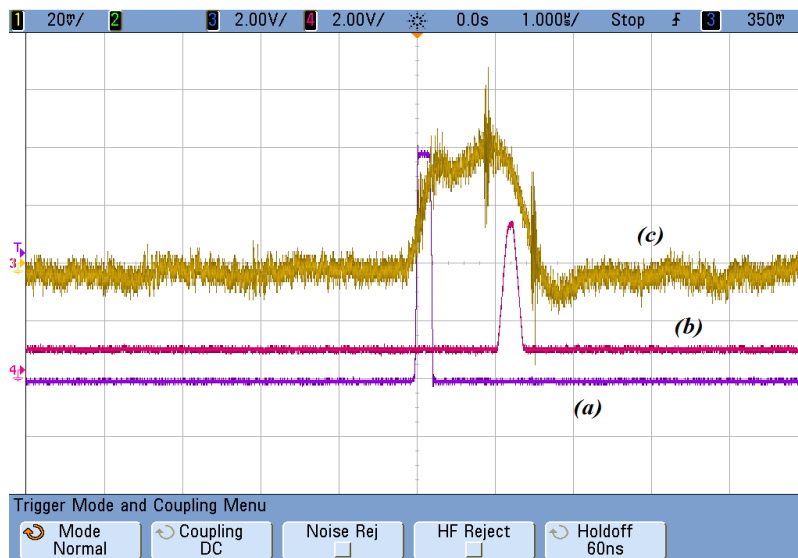


Figure 3-17 Effect of slow ramping in the falling edge of the switch control waveform (b) on the preamplifier output (c)

The effect of the fast falling edge degrades the pre-amplifier output (waveform (c)), as it injects current from channel to the control pin and makes the output rise again from the baseline with a positive slope. The slope of this falling edge was optimized separately to reduce charge injection. To enable this optimization, the function generator was used in the burst mode with a single pulse. Figure 3-17 shows the pre-amplifier output with this mode. It is observed from this figure that a slow falling edge of the switch control waveform of at-least ~ 200 ns duration completely eliminates the charge injection. This is in contrast to the positive slope observed in the previous case (figure 3-16) immediately after the falling edge. The final evolved waveform combining both the above switch waveform modes, generated from PSoC internal blocks is described in figure 3-18. It is observed from the figure that the evolved waveform combines both the

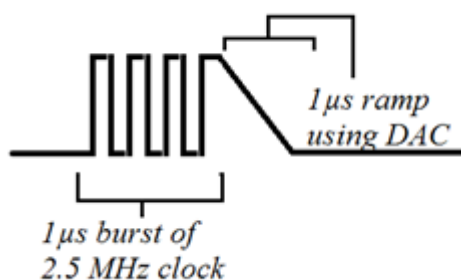


Figure 3-18 Switch control waveform generated using on chip PSoC blocks

high frequency burst and the falling edge ramping techniques. It consists of a burst of 1 μ s duration and a seamlessly integrated falling edge, which is controlled using the PSoC internal DAC with a fall time of 1 μ s.

3.5 PC based User interface

A simple user interface for the spectrometer is developed using M/s National Instruments LabVIEW® program. This interface is designed to perform spectra display

when the firmware is run in the PSoC hardware platform. The digitized 16 bit pulse height data is communicated as a formatted ASCII decimal number to the LabVIEW VISA (Virtual Instrument System Architecture) interface. This data communication is achieved through UART. The LabVIEW program extracts the numerical value from the formatted UART data to display it as a histogram plot. The plot is analyzed online by the user for statistical analysis.

3.6 Experimental results

The spectrometer was tested with a standard triple alpha source of 0.15 μCi activity. This source consists of mixed nuclides of plutonium-239 (Pu-239), Americium-241 (Am-241) and Curium-244 (Cm-244) emitting majority of alpha particles at peak energies of 5.155 MeV, 5.486 MeV and 5.805 MeV, respectively. Figure 3-19 shows the screen shot of LabVIEW front panel window during acquisition of Cm-244 alpha spectrum. Figure 3-20 shows the corresponding spectra in which the channel numbers have been converted to energy scale and plotted off-line using stored data from a spread sheet file. The Cm-244 nuclide emits alpha particles at two energies viz., 5.763 MeV and 5.805 MeV with the corresponding branching ratios of 23.3 % and 76.7 %, respectively. From figures 3-19 and 3-20, it is clear that both the minor and the major peaks present in the Cm-244 spectrum are resolved. A resolution of 30.55 keV FWHM (Full width between half maximum) is observed in the major energy peak (5.805 MeV) of Cm-244, which enables the minor energy peak at 5.763 MeV to be discerned in the spectrum.

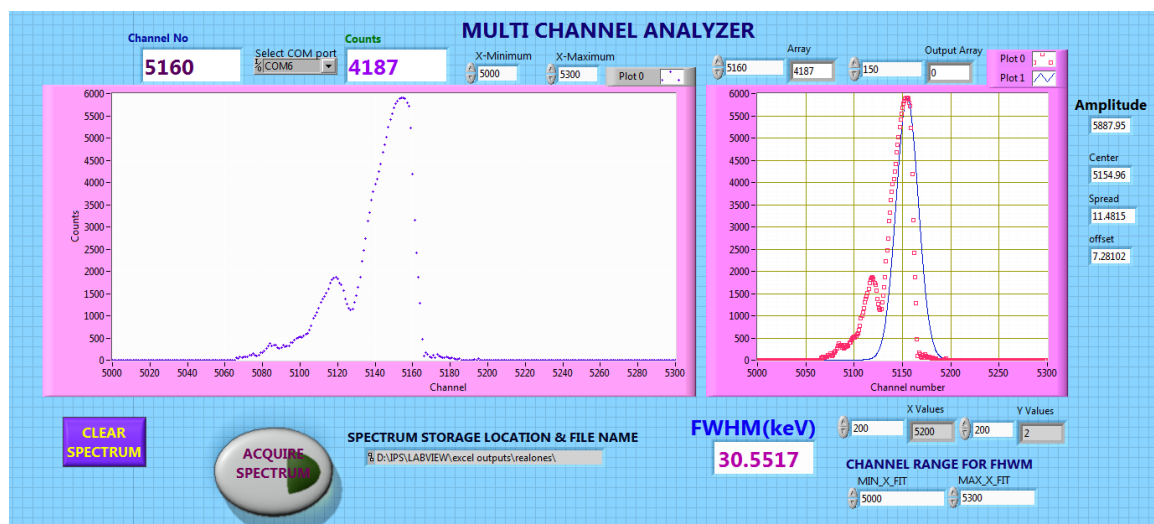


Figure 3-19 The detailed alpha spectrum of Cm-224 from a mixed nuclide source along with the real-time Gaussian fit

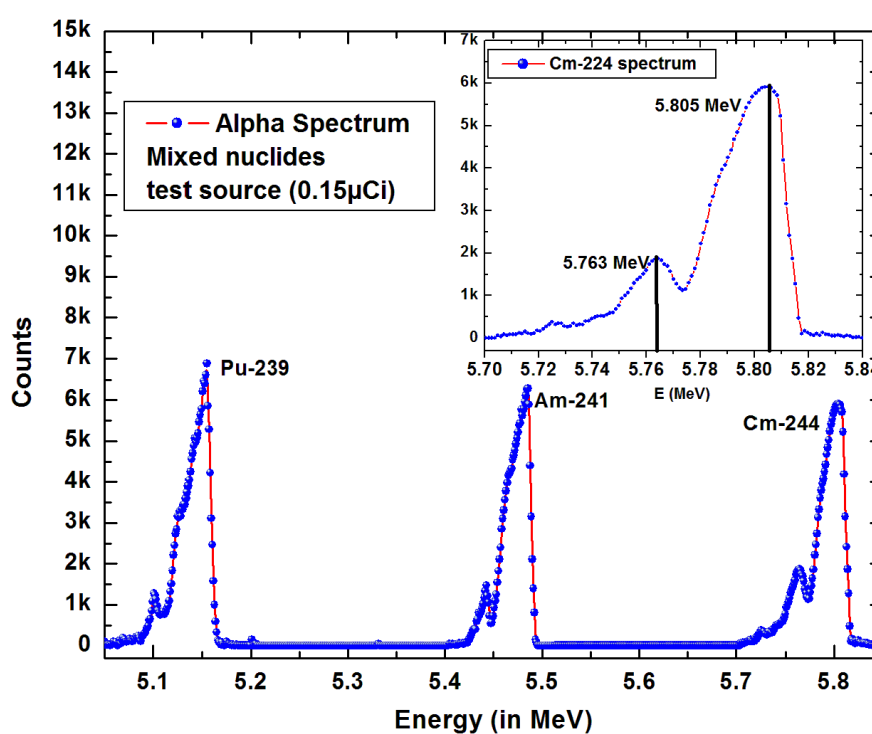


Figure 3-20 Combined alpha spectrum of the mixed nuclide source plotted off-line from stored data. Energy calibration is done using the Cm-224 peak

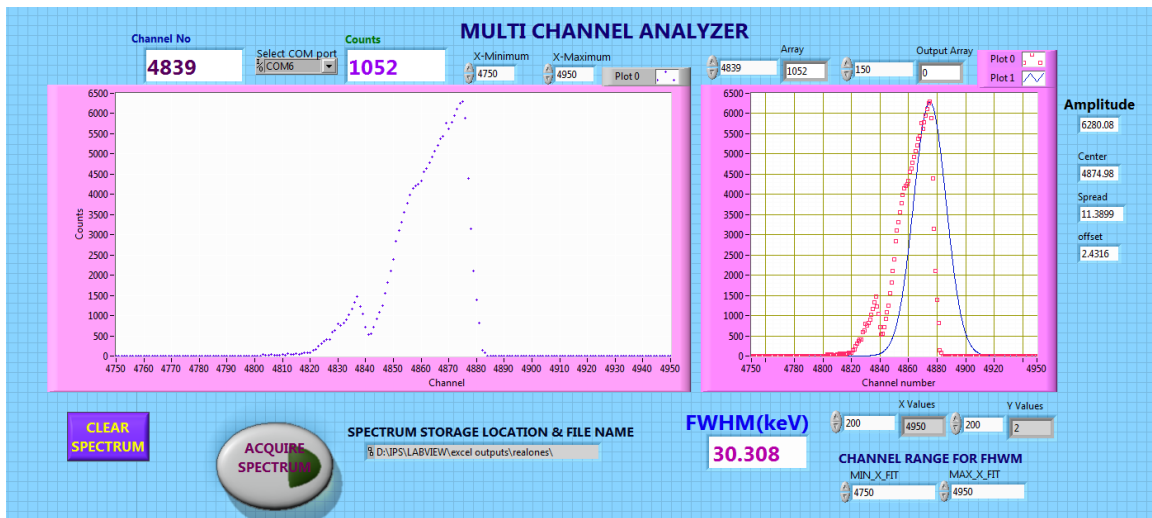


Figure 3-21 The detailed alpha spectrum of Am-241 from a mixed nuclide source along with the real-time Gaussian fit

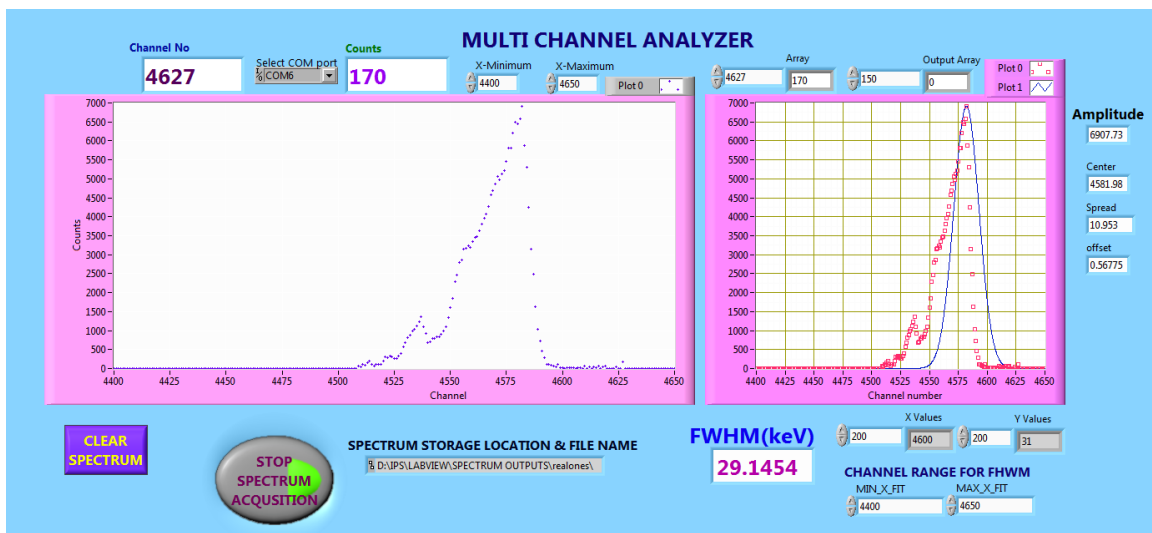


Figure 3-22 The detailed alpha spectrum of Pu-239 from a mixed nuclide source along with the real-time Gaussian fit

The LabVIEW GUI for the spectrum obtained for other nuclides present in the sample are also shown in the subsequent figures 3-21 and 3-22. The Am-241 spectrum shown in Figure 3-21 consists of the minor (5.443 MeV and 5.388 MeV) as well as the major (5.486 MeV) peaks. The branching ratios of 5.486 MeV, 5.443 MeV and 5.388 MeV alpha emissions are 85.2 %, 12.8 % and 1.4 %, respectively. As the 5.388 MeV peak is only 1.4%, it is not resolved in the spectrum.

The Pu-239 alpha spectrum shown in Figure 3-22 is given in terms of the channel numbers. The channel numbers are calibrated in terms of energy in figure 3-20 by using a conversion factor of 1.125 KeV per channel. This conversion factor is obtained from the americium peak at 5.486 MeV. The Pu-239 alpha spectrum consists of two minor peaks (5.143 MeV and 5.105 MeV) and a major peak (5.155 MeV). The major peak spectrum with a branching ratio of 73.4 % completely submerges the 5.143 MeV minor peak with the branching ratio 15.1% since this minor peak lies within half the FWHM (15 keV approx.) of the major peak. The other minor peak (5.105 MeV) with a branching ratio of 11.5 % is resolved in the spectrum owing to its large separation from the major peak in terms of energy.

The spectral resolution obtained with the present EPRR scheme is better in terms of resolution as compared to that obtained using a cost-effective readout design [44] which is portability-centric for field applications. It is to be noted here that the resolutions for Pu-239 reported in [44] by D. Vujo *et al* is 56 keV as compared to 29.1 keV in the present work. The pulse throughput of the entire system was measured using an on-chip PSoC counter to count the PE signal occurrences. An average pulse throughput of 180 cps was observed for this system which is lower by a factor of 5 compared to the design reported in [44] which is 1000 cps. Although there are reports of better spectral resolutions (10 to 15 KeV (FWHM)) achieved [21, 93-95] using advanced readout designs with PIN diodes, they are adopted for lab scale measurements. The difference in spectral resolution between the present work and that reported in ref. [21] are primarily attributed to three reasons, namely, leakage current, residual charge injection and clock signal feedthrough. The higher reverse leakage current (25 nA at 100 V reverse bias) in the M/s BEL PIN diodes as compared to the commercial M/s Hamamatsu PIN diodes (1-2 nA at 100 V reverse bias) used in the prior work [93] leads to spectral broadening. As seen from

sl.no.4 in table 3-2, the finite charge injection of a maximum of 5pC introduces errors in the pulse height. Clock signal feed-through in the feedback network, also known as digital cross-talk [96] in analog channel is specific to the EPRR scheme. This is an additional source of pulse height error.

As evident from the discussion above, the spectral resolution of 29.1 keV is better as compared to other portable detectors of both analog and digital pulse processing topologies employed for field applications with an added advantage that it is also cost effective. The cost reduction in the present spectrometer is owing to an optimised design and can be better understood by comparing and contrasting with other recent reports on portability centric analog signal processing chains by S.W. Kwak *et al.*, Y. Cheng *et al.*, A. Martin Sanchez *et al.* and D. Vujo *et al.* in [41,42,43 and 44]. In refs 41 to 44, conventional analog signal processing chain is employed at the detector front-end. In these processing chains, the preamp stage, pulse shaper and base line restorer use one, at least two and one high speed COTS Op-amp, respectively. In contrast, the present design employs only a single high speed COTS Op-Amp at the preamplifier stage. The utilization of lesser number of high speed COTS Op-Amps is reflected correspondingly in the reduction of cost by at least a factor of four. Incidentally, the price of a single high speed COTS Op-Amp is Rs. 950.

As far as spectrometers by W.K. Warburton *et al* [97] based on digital pulse processing topologies are concerned, a dedicated high end ADC and DSP are employed, thereby pushing up the cost. The high end ADC (AD9245BCPZ-40) with 40 Mega samples per second sampling capability at front-end typically costs around Rs.2360.

In addition to this, the output from the preamplifier consisting of a single Op-Amp is pre-processed using a pulse shaper stage utilizing two more Op-Amps, before feeding it

to the digitizer. The digitized preamplifier pulses are further processed using a DSP at 40 MHz clock which typically costs around Rs.500. A conservative cost estimate shows that the price of the signal chain alone in such systems would lie upwards of Rs.5000 (3 Op-Amps, 1 DSP and 1 ADC). In contrast to the above topology, the present design using PSoC is comparatively cheaper as it uses only three main components - a high-speed low noise Op-Amp (Rs. 950), a solid state analog switch (Rs 160) and the PSoC chip (CY8C5868 AXI-LP-035, Rs. 1470) including a low-end ADC (250 Kilo samples per second @ 14-bit resolution in-built) used for digitization. Thus, the overall cost of the new signal chain adds up to just Rs.2580 making it at least half as costly as the design by W.K. Warburton *et al.* In summary, the cost reduction in this design is achieved by elimination of (a) analog filters and (b) expensive high-speed ADCs. In addition to the above advantages, the versatility and adaptability of PSoC platform enables easy addition of new customized features such as isotope identification function, user programmable HV ramping control, battery monitoring and automatic air sampling with vacuum pump control. Effectively, the strength of this novel single chip design is that it is rugged for implementation in field conditions and enables portability due to miniaturization to a high degree.

3.7 Conclusions

A portable and cost effective PSoC based embedded read-out design has been successfully implemented, designed, fabricated and tested for alpha spectrometry. The essential features for an alpha spectrometer such as the high voltage ramping, its regulation, embedded pulsed reset scheme and data communication with graphical user interface have been successfully designed and verified. The throughput of the present

design is reasonable and satisfies the requirements of a low cost portable system which can be used in gross measurement applications like environmental radioactivity surveys.

CHAPTER 4 Design simulations of planar semiconductor neutron detectors.

4.1 Introduction

This chapter discusses in detail, the simulations for optimization of thickness of converter layer for planar semiconductor neutron detectors. As noted in chapter 1, the efficiency of the detectors strongly depends on the type of converter material and relative dimensions of the converter vis-a-vis the semiconductor regions. The simulations have been carried out based on the method outlined by Shultis and Mc Gregor [98]. As the dead layer also contributes to significant reduction in efficiency, the detailed simulation pertaining to inclusion of dead layer is also discussed. The converter thickness is optimized by Monte Carlo technique implemented in MATLAB program. The planar configuration of the detector is built by geometrical modifications in trench structured neutron detectors[49]. The effect of dead layers on efficiency is simulated by modification of this planar configuration by inclusion of the metal electrodes. The following sections discuss the factors affecting neutron detector design and their optimization / study through the above two simulations in detail.

4.2 Design evolution of neutron detectors

Different designs for semiconductor neutron detectors have been explored and investigated in recent years [99]. An important motivating factor for these efforts is the pursuit of high intrinsic neutron detection efficiency. The intrinsic neutron detection efficiency (ϵ_{int}), is defined as the probability that a neutron entering a detection volume gets registered in the detection system. In most applications, neutron detectors are

operated in the pulse mode. In this mode of operation, the detector signal is a series of randomly spaced current pulses in time, each caused by the ions of a neutron capture[32]. The time of occurrence of each pulse and its amplitude correspond to the time of arrival of the ions into the semiconductor region and their instantaneous energy, respectively. This raw detector signal is integrated in a charge sensitive preamplifier to generate a voltage pulse signal. The height of this voltage pulse represents the total energy deposited in the detection volume. Thus, for a neutron detector operating in the pulse mode, the ϵ_{int} , is defined as

$$\epsilon_{int} = \frac{\text{Number of pulses recorded}}{\text{Number of neutrons incident on the detector}} \quad (4.1)$$

An important factor that affects the value of ϵ_{int} , is the probability of neutron capture. Not all the neutrons that enter the detection volume undergo capture interaction. The type of the Converter Material (CM) and its length along the path of the neutron beam determine the number of neutrons that undergo capture interaction. It is quantitatively described by the neutron beam attenuation equation (4.2) for a parallel beam of neutrons incident with a fluence I_o on a CM.

$$I = I_o e^{-\Sigma_{capture} t} \quad (4.2)$$

Thus, the fluence I of the neutron beam exiting the CM with a macroscopic capture cross section $\Sigma_{capture}$, decreases exponentially with an increase in the thickness t of the CM. For any finite thickness t , there are always some neutrons in the beam exiting the CM without undergoing capture.

Another major factor that affects the value of ϵ_{int} is the energy straggling of ions. The energy straggling occurs due to a path-length distribution of the ions in CM, arising

from the probabilistic nature of the depth at which the neutron capture occurs. Therefore, the actual kinetic energies deposited by the ions, in the semiconductor region range from near zero values to that with which they are emitted in the capture reaction. Extraneous phenomena like gamma emissions accompanying neutrons and electronic noise also cause pulses similar to those arising out of neutron interactions. But, typically these are low energy events and hence, their maximum pulse heights are limited to voltage levels, which are lower compared to the maximum pulse heights of neutron events. Moreover, due to the energy straggling effect, the probability of ion energies getting reduced to levels comparable to that of the extraneous events increases.

In the operation of practical neutron detectors, the extraneous events are prevented from getting spuriously registered as neutron events by setting a minimum energy threshold known as the Low level discrimination (LLD) energy. Only those voltage pulses with heights above a minimum voltage corresponding to the LLD energy, are considered as true neutron events and are registered. The energy straggling effect in conjunction with a higher LLD setting, increases the probability of rejecting true neutron events, thereby reducing ϵ_{int} .

Based on these two important factors namely, the neutron-capture probability and the energy straggling effects in CM, ϵ_{int} is defined more appropriately as.

$$\epsilon_{int} = \frac{N_{capture}}{N_{incident}} \times \frac{N_{above\ LLD}}{N_{capture}} \quad (4.3)$$

where $N_{incident}$ is the total number of neutrons entering the detector volume, $N_{capture}$ is the number of neutrons undergoing capture interaction, $N_{above\ LLD}$ is the number of ions entering the semiconductor region and depositing energy above the LLD. The first and the second ratios in the equation (4.3) are identified as

- (a) The probability of a neutron entering the detection volume undergoing capture and
- (b) The probability of the ions entering and depositing energy in the semiconductor region above the LLD.

The emergence of various detector designs is attributed to the efforts in independently increasing the two probabilities mentioned above.

4.2.1 Detector configurations

The planar neutron detector has the simplest construction in which, a CM is coated on to a surface of a planar PN junction or a Schottky barrier diode. As shown in figure 4-1, some neutrons from the incident beam undergo capture in the CM layer of a planar detector. The resulting ion pairs emanating from these interactions are emitted in opposite directions in space. Out of the two ions, only that which has a finite component of displacement along the direction of the incident neutron beam, has a finite probability of entering the semiconductor detection volume. The thickness t of the CM determines the number of neutrons that undergo capture in a plane-parallel neutron beam that is incident normally on the detector surface. With an increase in t , initially there is an increase in the number of neutrons undergoing capture, as evidenced by the beam attenuation equation (4.2) and hence ϵ_{int} increases. Beyond a certain value of t the ions that are formed in the CM regions which are farther from the semiconductor region deposit a major portion of their kinetic energy in the CM itself. This is a consequence of the increased distance the ions have to travel inside the CM along the direction of incident neutron beam (z - axis in figure 4-1), in order to reach the semiconductor region. As a result, the number of ions that deposit energy above a set LLD level inside the

semiconductor region decreases, bringing about a reduction in ϵ_{int} . Therefore, the major limiting design factors for ϵ_{int} in a coated planar neutron detector are

- (a) collection of only one ion inside the semiconductor and the fact that
- (b) detection is possible, only if the displacement of the ions has a component along the incident neutron beam (along z-axis in figure 4-1) with sufficient energy.

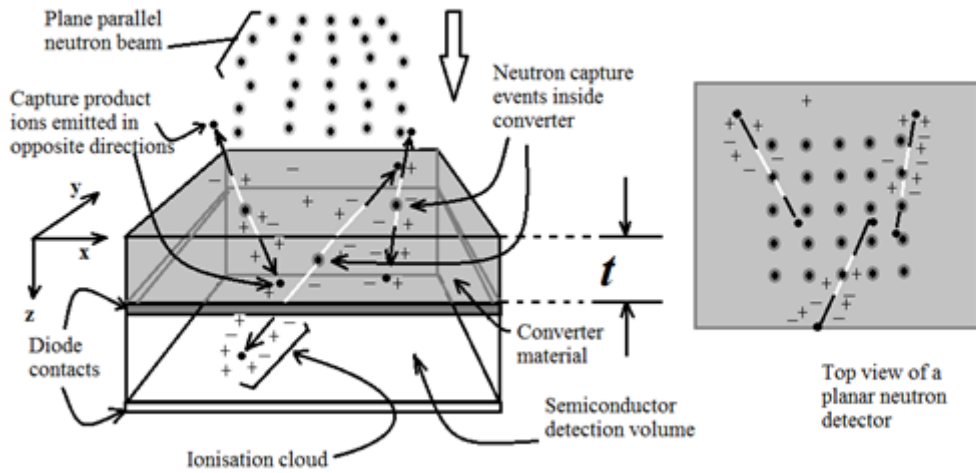


Figure 4-1 Construction details of a planar neutron detector along with the neutron beam direction and capture product ion tracks

Detector configurations employing trench structures have been extensively simulated using MATLAB [23]. Unlike planar configurations, the use of trench or pillar structures of CM inside a semiconductor detection volume directly enables the collection of both the ions. This ensures that, for each capture interaction, the probability of ions depositing energy above the LLD is increased. Moreover, the restriction on the ion displacement component is also eliminated. As shown in figure 4-2, an additional displacement component along a direction orthogonal to that of the incident neutrons (x-axis in figure 4-2) also contributes to its path towards the semiconductor region. In this design, the distance that an ion emitted in a fixed direction would require to travel and reach the semiconductor region remains the same at all depths inside the CM. Thus, the

CM thickness or more appropriately its depth, can be increased to any arbitrary value to enable more neutrons to undergo capture. This ensures that the contribution from neutron capture and the ion energy deposition, to the detector signal do not come into conflict.

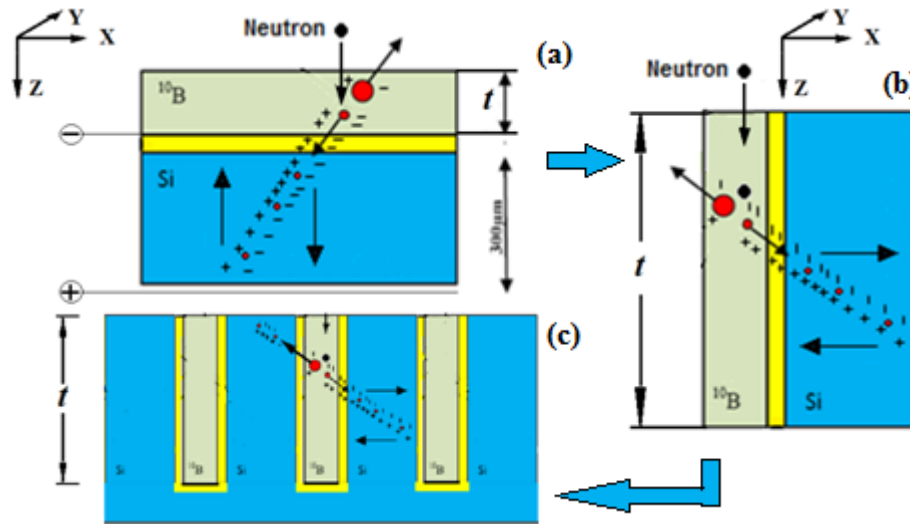


Figure 4-2 Evolution of the trench design from planar neutron detector (a). The energetic capture ions are enabled to reach semiconductor in a direction orthogonal to the neutron beam direction (b). The periodic repetition of the structure in (b) leads to the trench design in (c).

4.3 Motivation for Monte Carlo simulation

The qualitative insights on the working principle of neutron detectors have led to the emergence of different detector designs. These insights have to be verified using quantitative estimates of performance parameters prior to the actual fabrication of detectors for achieving optimum design implementation. In this work, ϵ_{int} , which is an important detector performance parameter, is estimated and thoroughly investigated through simulations. As is evident from equation (4.3), ϵ_{int} is a product of two probability terms. Though the first term –the neutron capture probability, can be readily estimated using the beam attenuation equation (4.2), the estimation of ion energy deposition probability is greatly affected by the spatial location of the neutron capture event and the

direction of emission of ions in space. This influence of spatial locations in a single x-y plane on the probabilistic events is illustrated in figure 4-3.

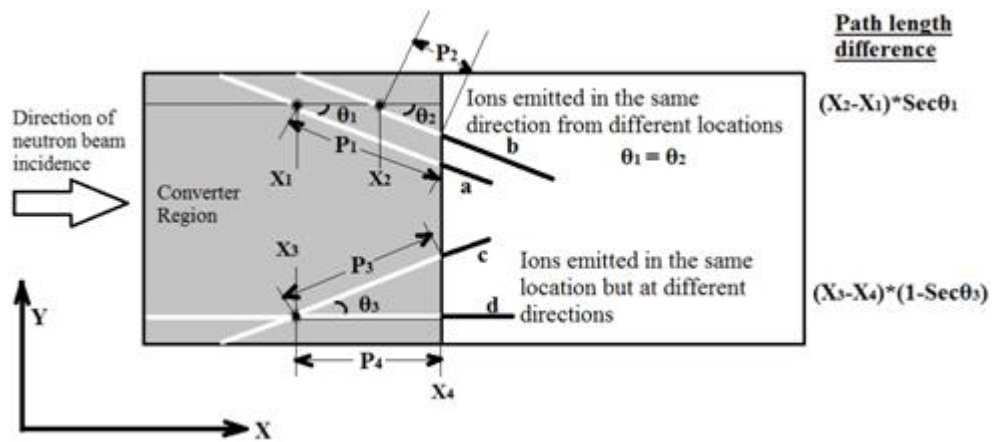


Figure 4-3 Effect of capture event location and ion emission direction on ion path length in semiconductor region

The spatial capture events occurring at the locations X_1 and X_2 are shown to emit ions with the same direction θ_1 with respect to the x-axis. But, due to the difference in X_1 and X_2 , their path-lengths (X) inside the converter P_1 and P_2 differ, making them deposit different amounts of their initial kinetic energy. Their residual energies (E) (details in section 4.4.3) at the interface of the CM and the semiconductor region are consequently different. It is this E that is represented by the detector signal. The difference in E at the boundary is reflected in length of segments **a** and **b**. The figure also illustrates another case where the capture events occur at the same location (X_3), but the direction of emission of the ions is different (0 and θ_3 degree). This again gives rise to a path difference (P_3-P_4) inside the CM, thereby affecting E at the CM-semiconductor boundary. This difference in E at the boundary is again reflected in the lengths of segments **c** and **d**. The estimation of ion energy deposition is further complicated by two critical factors namely, the non- deterministic nature of both the spatial location and the direction of emission of the ions in space.

An effective computational approach to estimate a non-deterministic parameter, is to use the Monte Carlo method. In this work, Monte Carlo simulation of ion energy deposition is done for estimation of ϵ_{int} for planar detectors under different design conditions. For a given set of detector dimensions, the estimation of number of neutrons undergoing capture is straightforward. For this, the beam attenuation relation (equation (4.2)) based on the capture cross section data for the type of CM is used. Subsequently, the Monte Carlo approach is introduced in the simulations for the estimation of ion energy deposition. This is done by the randomized computational selection of the spatial location and the direction for neutron capture and ion emission, respectively. The ions are spatially tracked and their energy deposited in the CM as well as the semiconductor regions are logged. Finally, ϵ_{int} is estimated as the ratio of the number of events with energy deposition above a set LLD value to the total number of neutrons incident on the detector. These simulations are repeated for different sets of detector dimensions and LLD settings to optimize ϵ_{int} . The details of the implementation of the Monte Carlo method in MATLAB is discussed in the next section.

4.4 Simulation methodology

Several established simulation approaches like GEANT4 and MCNPX, employing Monte Carlo method have been adopted in literature [100]. Bellinger [49] has carried out simulation and corroborated with experiments on trench geometries using MATLAB codes. These codes are user friendly, versatile and can be customized to suit different detection scenarios. For optimization, the method of MATLAB is simpler and easily adaptable. Therefore, taking a clue from this, the optimization of converter thickness and the effect of dead layer has been studied in this thesis using MATLAB.

The methodology adopted for the optimization involves other Monte Carlo codes like (Stopping and Range of Ions in Matter)SRIM and (Transport of Ions in Matter) TRIM along with curve fitting tools like TableCurve®[101]. The data for residual-energy E versus path-length X (discussed in section 4.4.4) for ions of neutron capture are generated using the SRIM and TRIM codes. Subsequently, the empirical functions for the generated data are fitted using TableCurve®. It is to be noted that this methodology involves significant statistical variations in the final fit[101]. Hence, before proceeding to the actual simulation, it is imperative to understand the effect of sample size to be chosen for parameters such as ion population and the number of data points. These are known to have a strong bearing on the E versus X curves which in turn have an impact on ϵ_{int} . Shultis and McGregor [98] have extensively used the particle tracking methodology to simulate detector efficiency for trenches in three dimensions. This methodology is embarked to simulate the results of ref [98]. The details of the benchmarking simulations are discussed in section 4.5. Central to these simulations is the concept of a detector unit cell, which is subsequently described in this section.

4.4.1 The unit cell

A detector unit cell is defined as the basic structure which, when repeated periodically in space, would form the entire detector. Figure 4-4 (a) is a schematic of the entire detector, which is built by the periodic repetition, of the structure shown in figure 4-4 (b), in the x-direction. By definition, figure 4-4 (b) is the unit cell structure and its sectional view with dimensions are illustrated in figure 4-4 (c). W_{cell} , ‘wafer depth’ and L are the width, height and length of the unit cell, respectively. Further, t and W are the depth and width of the converter material inside the unit cell, respectively. In the configuration illustrated in figure 4-4, the trench structure evolves to a planar one when $W=W_{cell}$.

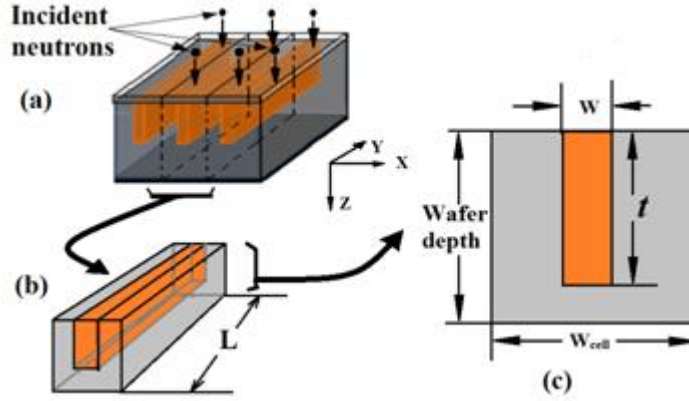


Figure 4-4 The concept of a unit cell. The complete detector shown in (a) is formed by the periodic repetition of the structure (b). (c) shows the front view of (b) along the positive y-axis

The basic assumptions in the existing model [49] based on the unit cell concept, which are crucial in describing the simulation methodology are listed in the next section.

4.4.2 Important assumptions in the simulation model

- (a) In general, the detector materials employed consist of boron (B^{10}) / Lithium Fluoride (Li^6F) as converter material, silicon (Si) as detection medium and gold (Au) as dead layer.
- (b) While considering the neutron absorption phenomena by the capture interaction, the silicon semiconductor region is assumed transparent to neutrons i.e. neutron capture effects in silicon are neglected. The neutron scattering effects in the silicon semiconductor region are also ignored.
- (c) The detector is irradiated with a parallel beam of thermal neutrons uniformly and normally illuminating the top surface (x-y plane in figure 4-4) of the detector.
- (d) The neutron absorption cross sections of B^{10} and Li^6 are much larger compared to that of fluorine and silicon [102, 103] and hence, contribution of only B^{10} and Li^6 to neutron absorption are considered.

- (e) All the energy deposited in the semiconductor region is assumed to contribute to the signal pulse height of the detector. The charge transport properties and the imperfections in the semiconductor diode contribute negligibly to the charge loss and are therefore ignored.

4.4.3 Particle tracking methodology inside the unit cell

The simulation methodology adopted in this thesis [104] is illustrated in figures 4-5, 4-6 and 4-7. In this methodology, a plane parallel beam of neutrons perpendicular to the detector face (shown in figure 4-5) is assumed incident uniformly on the top surface of the unit cell. As a first step, from a uniform random distribution, a random point (\mathbf{x}_i , \mathbf{y}_i) is selected and assigned for each incident neutron. Those coordinates which lie outside the top surface boundary of the CM are not considered. Once the entry point coordinates (\mathbf{x}_i , \mathbf{y}_i) are assigned, a depth \mathbf{Z}_i along a ray passing through the same top surface entry point is randomly selected using the relation,

$$\mathbf{Z}_i = \frac{\ln[1-(\mathbf{P}_{int} \times \mathbf{R}_i)]}{-\Sigma_{capture}} \quad (4.4)$$

where, $\Sigma_{capture}$ is the thermal average macroscopic capture cross-section for a given CM and \mathbf{R}_i is a uniform random number selected from the interval (0, 1) for the i^{th} ion. Further, \mathbf{P}_{int} , is the probability of neutron interaction at the end face of the CM and is expressed in terms of the neutron transmission term from equation (4.2) as

$$\mathbf{P}_{int} = 1 - e^{-\Sigma_{capture}t} \quad (4.5)$$

Where t is the thickness of the CM. For one of the ions from each capture, apart from the random depth \mathbf{z}_i in the beam direction, a random direction \mathbf{D}_i in space is also assigned. \mathbf{D}_i is chosen from an isotropic uniform distribution of direction cosines. The other ion is assigned exactly the opposite direction ($-\mathbf{D}_i$) in space.

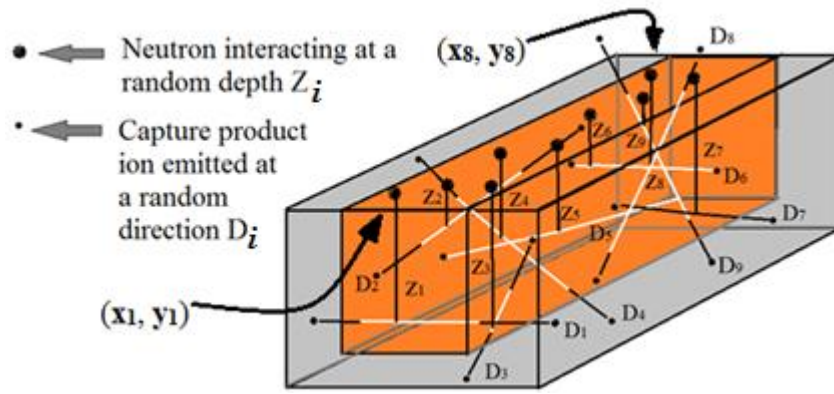


Figure 4-5 Initialization of the simulation by assigning random depths of interaction for neutrons and random assignment of direction cosines for the emitted ions in space

Figure 4-6 illustrates the various regions of the detector seen by one of the ions as it traverses through it. In general, the ions emitted in a particular direction inside CM are assumed to travel in a straight line through the detector and deposit their energy. In the course of this travel, they encounter alternate **CM** and semiconductor (**SC**) regions as shown inside the dashed line. Generally, the ions traverse multiple unit cells before coming to a stop, after completely depositing their initial kinetic energy in the various detector regions. The energy deposited by an ion i in each of the detector regions

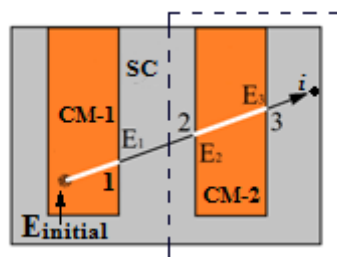


Figure 4-6 Ion energy deposition in different regions of a detector by one of the ions that it has traversed, is found by a spatial tracking method explained below. It is to be noted that, each ion from the neutron capture reaction is uniquely identified by its initial kinetic energy. This kinetic energy of i in region **CM-1** at the instant when it is emitted is $E_{initial}$. By the time it reaches the boundary **CM-1-SC**, it has an energy E_1 , thereby

depositing its lost energy ($E_{\text{initial}} - E_1$) in CM-1. The energy E_1 is known as the residual energy of the ion i at location 1. Similarly, the ion i continues to deposit energies ($E_2 - E_1$) and ($E_3 - E_2$), in the regions SC and CM-2, respectively.

Figure 4-7 illustrates the tracking of the spatial co-ordinates of the ion i with its energy E as it traverses through multiple unit cells in the detector. This tracking is done by utilizing a back-tracking method [90]. This method hinges on two facts. First, for an ion of type i , the residual energy E at the current position inside a material m is a function of the path-length X it has travelled in it. Second, the path-length X it would have travelled in m to reach the current position, is a function of its current residual energy E . This interdependence of E and X in material m is denoted by $\bar{E}_m(X)$ and $\bar{X}_m(E)$, respectively. These functions are determined by using SRIM and TRIM simulations, which are explained in detail in the forthcoming section.

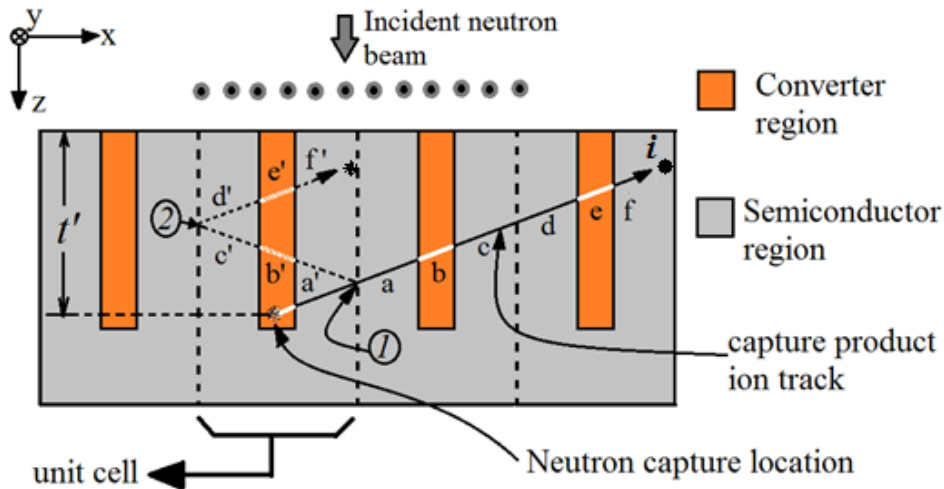


Figure 4-7 Ions born in a converter region traverse multiple unit cells. Their path can be tracked inside a single unit cell using specular reflection at the boundary of their original unit cell

The back-tracking method is implemented by incrementing the position of the ion i by infinitesimal lengths inside the unit cell structure. The application of a specular

reflection boundary (shown as points 1 and 2 in figure 4-7) inside the unit cell enables the mapping of the spatial track of ion i through multiple unit cells ($\mathbf{a-f}$) to a track in the single unit cell ($\mathbf{a'-f'}$). For those positions which lie on the segments of its path that fall in the SC region, the successive decrements in its residual energy \mathbf{E} are accumulated. The unit cell approach being periodic in nature with specularly reflecting boundaries, simplifies this tracking and accumulation of deposited energy, extending it for the entire detector. The incremental tracking enables the simulation to accurately capture three important events in the ion history and execute relevant operations. The events are

- (a) The arrival of the ion at the boundary of unit cell, in which its direction cosines are changed to that of a specularly reflected one.
- (b) The arrival of the ion at the CM-SC boundary, in which the accumulation of residual energy decrements is started/ stopped.
- (c) The attainment of zero residual energy by the ion, in which the tracking operation itself is stopped.

4.4.4 Estimation of $\bar{E}_m^i(X)$ and the $\bar{X}_m^i(E)$ functions

As stated in the previous section, the back-tracking method essentially increments the ion's spatial position and accumulates its residual energy decrements using the $\bar{E}_m^i(\mathbf{X})$ and $\bar{X}_m^i(\mathbf{E})$ functions. An analytical fit of parameters facilitates the calculation of these functions that can be easily incorporated in a MATLAB® program, which is the platform for the simulation. To obtain the empirical functions $\bar{E}_m^i(\mathbf{X})$ and $\bar{X}_m^i(\mathbf{E})$ for ions in various target media, the TRIM code is used [91]. It is a software package specifically employed to calculate the transport of ions in matter. For each of the ions, the TRIM simulation starts with an assignment of kinetic energy $\mathbf{E}_{initial}$, which is same as that at the instant of its birth in the neutron capture reaction. With each ion incident perpendicular to the target surface, a rough estimate of its range in both SC and the CM is calculated. This

range is arbitrarily subdivided into equal length intervals representing progressively increasing path-lengths travelled by the ion. Subsequently, a set of simulations are performed under similar conditions stated above, for a beam of ions to obtain a tabulation of data points (\mathbf{E}, \mathbf{X}). For achieving better statistics, the simulations have been performed with beams containing 10000 ions. It should be noted here that the length of the target along the direction of the beam is progressively incremented by the previously determined path-length values \mathbf{X} , before the commencement of each simulation. In each of these simulations, the mean kinetic energy of the ions in the exiting beam is calculated and recorded as the residual energy \mathbf{E} . Finally, the tabulated data (\mathbf{E}, \mathbf{X}) are fed to the curve fitting software TableCurve® [101] to fit and obtain $\bar{\mathbf{E}}_m^i(\mathbf{X})$ and $\bar{\mathbf{X}}_m^i(\mathbf{E})$ functions.

4.4.5 MATLAB code for particle tracking

For completeness, figure 4-8 shows the flow chart for a MATLAB® program designed by Bellinger [49] to simulate the straight trench detector comprising of CM-SC as represented by $\mathbf{B}^{10}/\mathbf{Li}^6\mathbf{F-Si}$, respectively. The core section of the code deals with tracking the path of the ions through the unit cell and accumulating the energy deposited in the silicon region alone. The residual energy \mathbf{E} of the ion at each incremental step on its path is represented by the symbol **ResE**. The decision boxes show the assertion logic and the negation logic by the symbols ‘**Y**’ and ‘**N**’, respectively. The variable ‘**EnergyDep_Si**’ represents the accumulated ion energy deposited in the successive silicon regions. As shown in the flow chart, the ion path is incremented in units of 1nm in its current direction until it finds itself in the unit cell boundary. Once the ion reaches the unit cell boundary, a specular reflection direction is chosen by modification of its existing direction cosines. A brief summary of the above methodology is outlined in the next section.

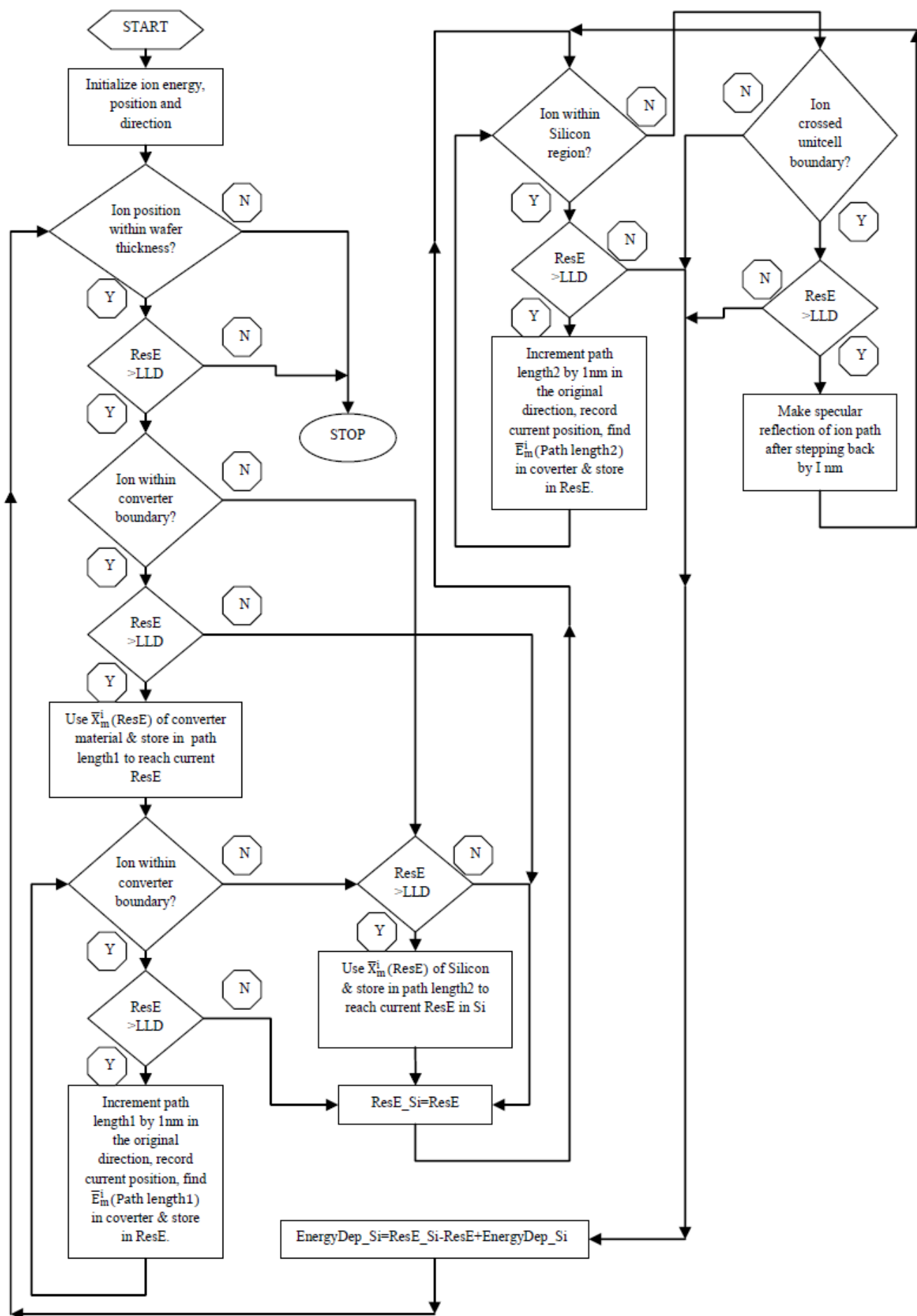


Figure 4-8 Flow chart showing the algorithm for estimation of energy deposited in silicon for a trench neutron detector

4.4.6 Summary of the simulation methodology

For clarity, figure 4-9 shows the entire sequence of steps in this simulation methodology, starting from the estimation of empirical fits to calculation of intrinsic neutron detection efficiency.

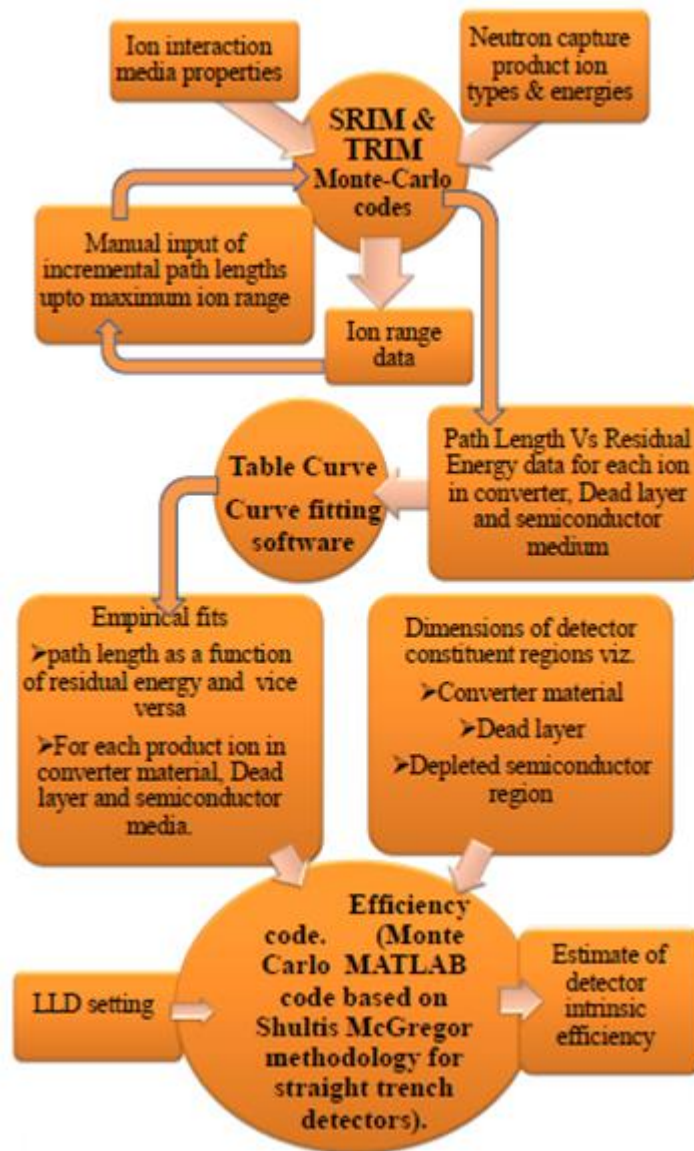


Figure 4-9 Flow chart showing the complete sequence of operations for estimating neutron detector efficiency

The operations are divided into three main steps namely,

- Generation of (E , X) data using TRIM code.
- Curve fitting for the generated data.
- Simulating the detector operation using the above empirical results in the back-tracking method.

4.5 Benchmarking simulations in trench detectors

As noted in section 1.5.3, the $^{10}\text{B}(\text{n}, \alpha)$ reaction and the $^6\text{Li}(\text{n}, \alpha)$ reaction are the two most important capture interactions used for detection of thermal neutrons. Bellinger [49] has reported ϵ_{int} values estimated using MATLAB for Li^6F converter. Following the methods outlined by Bellinger, an attempt is made in this thesis to estimate efficiencies incorporating the double-branched B^{10} conversion reaction. Further, the simulation results are benchmarked with existing values published in the literature [98]. This step was necessitated to benchmark and establish an error free procedure in the simulation process, as it involves multiple computational steps. The result of the simulations in terms of the ϵ_{int} variation with respect to the fraction of CM width (W) out of the total unit cell width (W_{cell}) for $W_{cell} = 4 \mu\text{m}$ and trench depth $t = 10 \mu\text{m}$ are tabulated in table 4-1. The ϵ_{int} values compare well with those in ref [98], indicating that the simulation methodology is successfully benchmarked.

Table 4-1 Estimated efficiencies for trench neutron detectors for different fractional converter trench widths. The unit cell width and the trench depth are kept at $4 \mu\text{m}$ and $10 \mu\text{m}$, respectively

$\frac{W}{W_{cell}}$	Efficiency estimated In the present work	Efficiency values from reference[98].
0.1	3.6021	3.7000
0.2	7.0195	6.9400
0.3	9.4941	9.7300
0.4	12.3245	12.1300
0.5	14.0403	14.1700
0.6	15.5452	15.8000
0.7	16.8771	17.0900
0.8	16.5409	15.5100
0.9	6.6721	6.1000

4.6 Estimated Efficiencies for planar detectors

The simulations of the trench configurations carried out using MATLAB described in the previous sections have been corroborated with experiments to a high degree of accuracy [49]. It is therefore appropriate, that this method would be successful for simulation of two dimensional planar configurations, which are described in the subsequent sections.

This section discusses the simulation results on planar neutron detectors with the double-branched B^{10} and the Li^6F converter. The ϵ_{int} values are estimated for planar neutron detectors using the approximation in a trench structured detector model as stated in section 4.4.1. For these simulations, neutrons are assumed incident normally on the top surface of the unit cell having an area of $100\mu\text{m}^2$. The LLD energy level, above which the energy deposited is considered to originate from a true neutron event, is fixed at 300 KeV. This LLD level is chosen on the basis of gamma absorptions in silicon which lead to spurious neutron events. In general, the gamma absorption cross section decreases with increasing gamma energy. In silicon, this absorption is significant only up to the gamma energy of 60 keV [92]. In order to have a better margin for gamma discrimination, the LLD is chosen at five times this value i.e. 300 keV.

The behavior of the ϵ_{int} value with the variation of the thickness of converter is studied. As shown in figure 4-10 for the case of B^{10} converter, initially, ϵ_{int} increases with increasing thickness of the converter material, reaching a maximum value of 4% at 2.5 μm . This result compares with [28] although a different technique is adopted. This optimized thickness t_c of 2.5 micron is used to estimate the effect of LLD. A similar variation of ϵ_{int} value with thickness is observed in the case of Li^6F converter also (figure 4-11). In this case a maximum efficiency of 4% occurs at a thickness t_c of 25 μm of Li^6F .

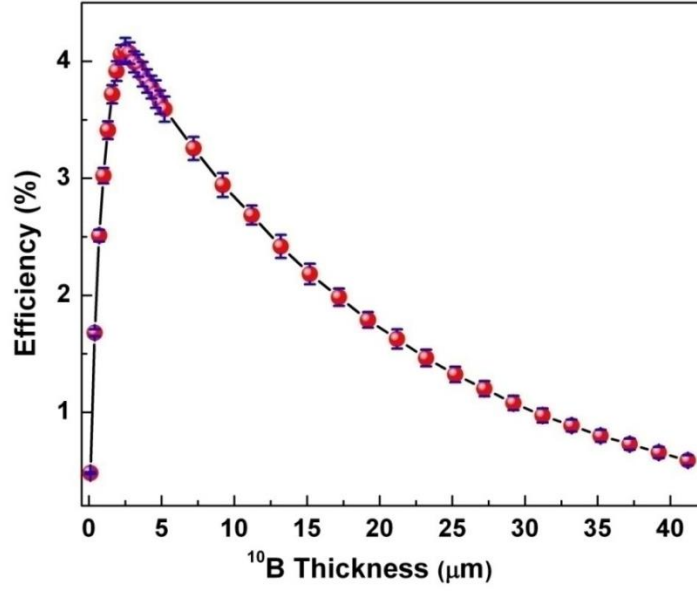


Figure 4-10 Variation of ϵ_{int} of a planar neutron detector with the thickness of the B^{10} converter layer

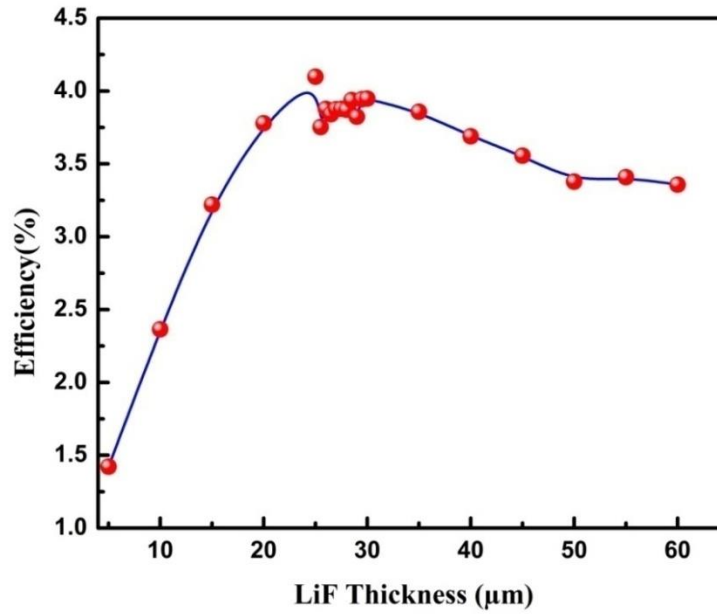


Figure 4-11 Variation of ϵ_{int} of a planar neutron detector with the thickness of the Li^6F converter layer

This behavior of ϵ_{int} in both cases is explained on the basis of the neutron transmission phenomenon, according to which, the probability of a neutron undergoing capture

increases with increasing thickness of the absorber [32]. The subsequent decrease with increasing thickness is the result of self absorption of ion energy in the converter itself. This effect is more prominently found for ions created farther away from the semiconductor region. This reduces the energy deposited in the depleted semiconductor region to below LLD levels.

4.6.1 Efficiency variation with respect to the LLD

The LLD energy level setting is a crucial factor in determining the intrinsic detection efficiency of a neutron detector. As discussed in section 4.2, the LLD energy level is used to distinguish between true and spurious neutron events. To determine the effect of LLD energy on the efficiency, B^{10} layer thickness of $2.5\ \mu\text{m}$ was chosen based on the optimization discussed in the previously in this section. The simulations were performed for LLD energies ranging from 0.1 MeV to 1 MeV. This energy range coincides with the typical gamma energies encountered in neutron sources [28]. The results presented in figure 4-12 show that the efficiency of the neutron detector decreases with increasing LLD. This result is similar to that observed for trench detectors with Li^6F converters reported in [49]. This decrease is ascribed to the fact that a larger fraction of true neutron events are ignored by the system with a higher LLD. Although it is desirable to set LLD at high values, in order to have a better discrimination from gamma, this interferes with the detection of genuine neutrons. This therefore, warrants optimization to set the LLD at a judicious value.

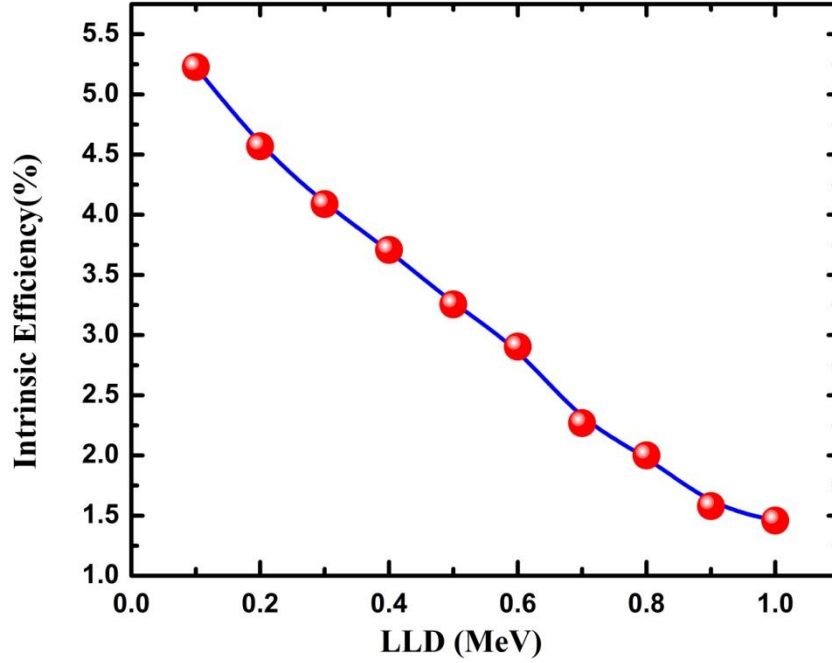


Figure 4-12 Variation of ϵ_{int} of a B^{10} coated planar neutron detector with LLD setting. The B^{10} thickness is fixed at $2.5\mu m$

4.7 Effect of dead layer on neutron detector efficiency

4.7.1 Introduction

As mentioned in section 1.5.3, the dead layers in a planar neutron detector influence the detection efficiency. In order to estimate the device performance and ϵ_{int} more accurately for practical devices, it is essential that the effect of ion energy loss inside the top metal electrode layer is included in the Monte Carlo simulation prior to device fabrication. In practical silicon PIN diodes, the dead layer comprises of various sub layers like Phospho Silicate Glass (PSG), metal electrode layer, SiO_2 and the P+ silicon. Its thickness extends to a length of 7 microns from the top surface of diode. Of all the sub layers, the metal electrode layer which typically consists of either aluminum,

gold, or titanium with thickness ranging from 0.1 μm to 1 μm [36, 93] has the lowest electric field intensity and is hence the most prominent sub layer [94]. In this work, gold (Au) is chosen as the dead layer for the following reasons

- (a) It forms an ideal ohmic contact,
- (b) it protects the electrodes from oxidation and
- (c) fabrication processes for gold-silicon eutectic systems are standardized.

It may be further noted that gold is a natural choice as metal pads, as it possess a low eutectic temperature with silicon and hence the wafer processing temperature is less than 100 °C below the final temperatures [95]. This ensures that the device configurations/ characteristics do not change upon ‘adding’ the gold pads. The simulations are carried out with typical thicknesses as encountered in practical devices [36, 93].

4.7.2 MATLAB® code for dead layer simulation

The MATLAB code as discussed in section 4.4.6 was modified for inclusion of dead layer. The unit cell configuration as shown in figure 4-13 includes a dead layer sandwiched between silicon and converter material region. The parameters of the unit cell used in the simulation are as follows. The width of the unit cell \mathbf{W}_{cell} , width of the converter material \mathbf{W} , depth of the converter material \mathbf{t} , the wafer depth and the dead layer thickness \mathbf{d} are 10 μm , 10 μm , 300 μm and variable, respectively. In this configuration, the dead layer thickness \mathbf{d} is varied from 0.1 μm to 1.1 μm in steps of 0.1 μm . The flow chart in figure 4-14, which is self explanatory, is a modified flow chart of figure 4-8 for the inclusion of dead layer in the MATLAB program.

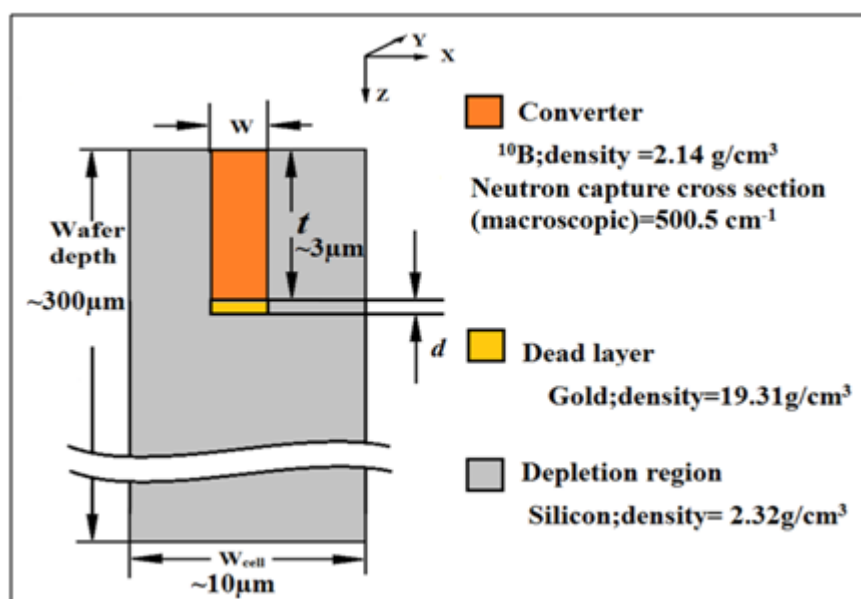


Figure 4-13 Inclusion of dead layer at the bottom of the converter trench

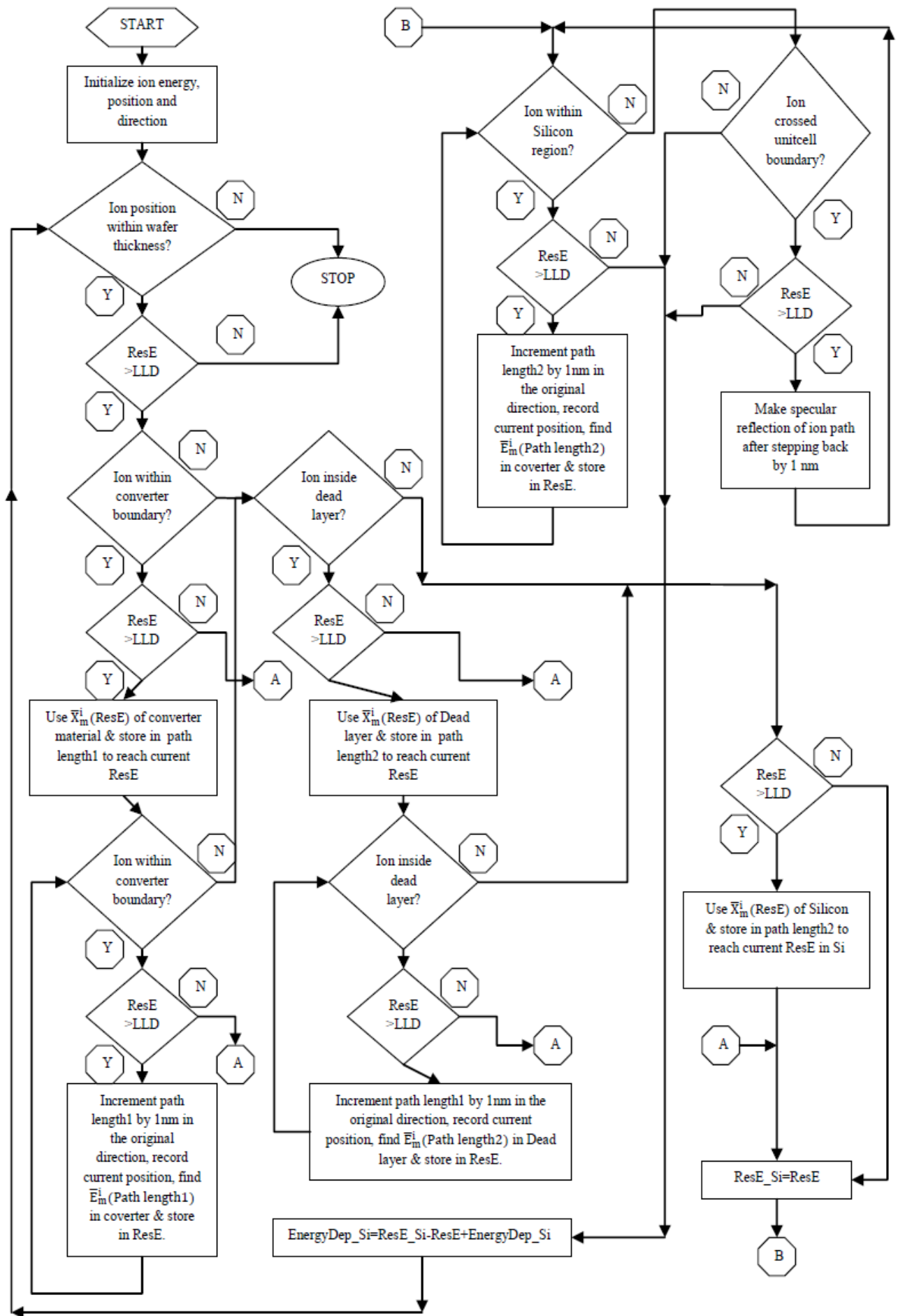


Figure 4-14 Flow chart showing the algorithm for estimation of energy deposited in silicon for a simple planar neutron detector with the inclusion of a dead layer

The procedure adopted for $\bar{E}_m^i(\mathbf{X})$ and $\bar{X}_m^i(\mathbf{E})$ estimation as discussed in the section on optimization of converter material thickness is followed for the dead layer also. The results are discussed in the next section.

4.8 $\bar{E}_m^i(\mathbf{X})$ and $\bar{X}_m^i(\mathbf{E})$ estimation in gold dead layer medium

The empirical relations $\bar{E}_m^i(\mathbf{X})$ and $\bar{X}_m^i(\mathbf{E})$ have been generated for the configuration shown in figure 4-13. The converter materials considered in the simulation are \mathbf{B}^{10} and $\mathbf{Li}^6\mathbf{F}$. Hence, the ion residual energy data are generated for the following ions and target conditions.

- (a) The Boron \mathbf{B}^{10} conversion reaction ions in gold (\mathbf{Au}) medium.
- (b) The Lithium \mathbf{Li}^6 conversion reaction ions in gold (\mathbf{Au}) medium.

As discussed in section 1.5.3, the \mathbf{B}^{10} neutron capture reaction has four possible ions, while the \mathbf{Li}^6 reaction produces a triton and an alpha particle. For the purpose of simulation, the ions of the former reaction are identified based on their initial energy as Alpha-1 (1.7762 MeV), Alpha-2 (1.4721 MeV), Lithium-1 (1.0133 MeV) and Lithium-2 (0.8398 MeV).

4.8.1 Empirical fits for \mathbf{B}^{10} and \mathbf{Li}^6 conversion ions in gold (\mathbf{Au}) medium

Figures 4-15 and 4-16 show the transport data of \mathbf{B}^{10} ions in gold layer calculated using TRIM and SRIM. As outlined in section 4.4.4, the empirical fits were obtained for $\bar{E}_m^i(\mathbf{X})$ and $\bar{X}_m^i(\mathbf{E})$. The behavior of monotonic decrease of residual energy \mathbf{E} with path-length \mathbf{X} is similar to that observed in the case of transport of ions in silicon and \mathbf{B}^{10} converters[105]. Tables 4-2 and 4-3 show the empirical fits obtained using TableCurve® for $\bar{E}_m^i(\mathbf{X})$ and $\bar{X}_m^i(\mathbf{E})$ of each ion.

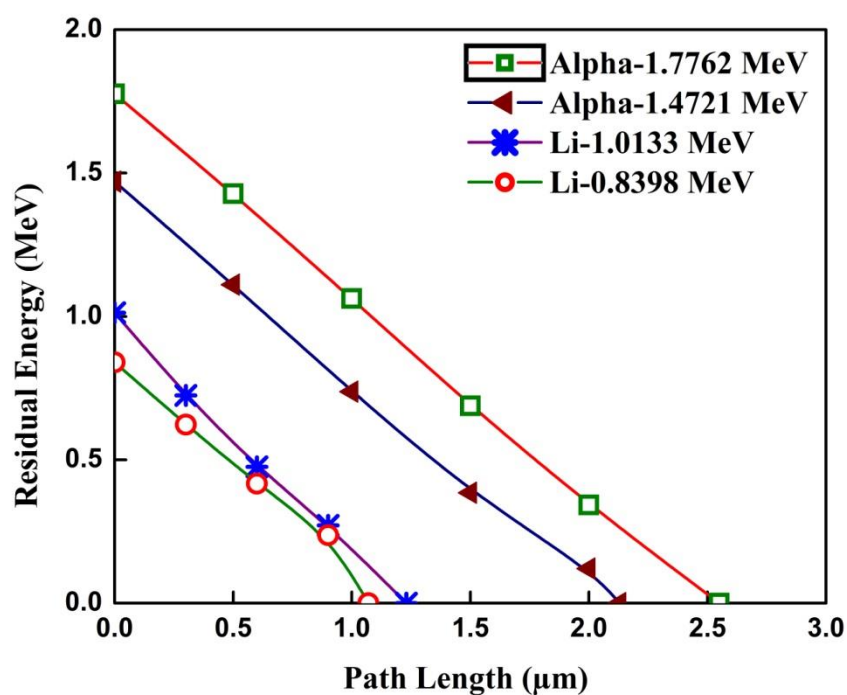


Figure 4-15 Interpolated residual energy versus path length data for transport of Boron (B-10) neutron conversion ions in Gold (Au)

Table 4-2 Empirical fit of residual energy $\bar{E}_m^i(X)$ after a path length 'X' in gold (Au) for B¹⁰ conversion ions

1.	Alpha-1 1.7762 MeV	$1.7767845 - 0.95797759(X) + 0.97449771(X^2) - 1.2010791(X^3) + 0.57103536(X^4) - 0.091596647(X^5)$
2.	Alpha-2 1.4721 MeV	$2.2805385 + 0.25256993(X^{2.5}) - 0.067546032(X^3) - 0.809966(e^{(X)})$
3.	Lithium-1 1.0133 MeV	$1.0131683 + 4.2973334(X^{1.5}) + 6.0278161(X^2) - 2.5451008(X^{2.5})$
4.	Lithium-2 0.8398 MeV	$0.84165019 - 902462894(X^2) + 16.988919(X^{2.5}) - 8.4683048(X^3)$

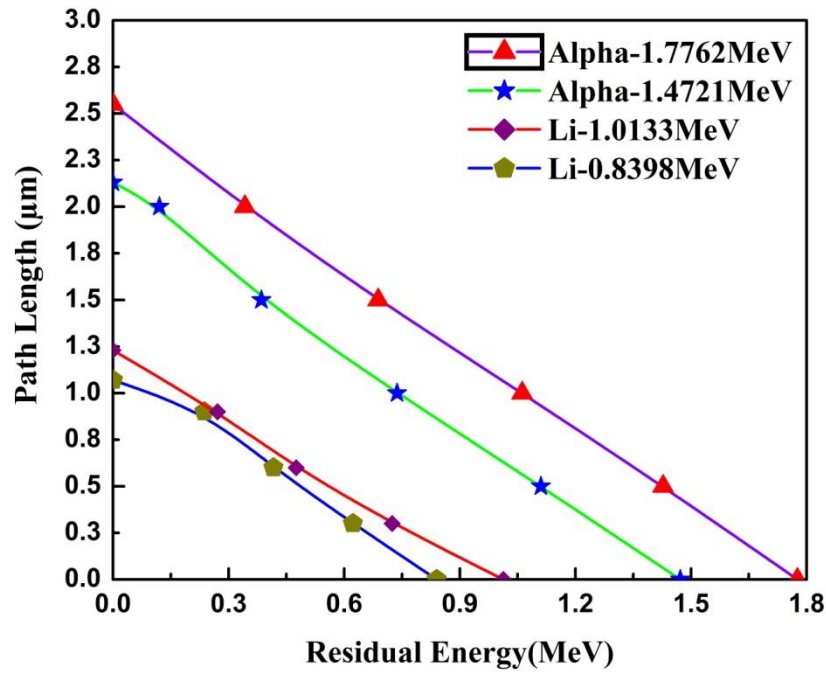


Figure 4-16 Interpolated path length versus residual energy data for transport of Boron (B-10) neutron conversion ions in Gold (Au)

Table 4-3 Empirical fit of path length $\bar{X}_m^i(E)$ to reach a residual energy 'E' in gold (Au) for B¹⁰ conversion ions.

1.	Alpha-1 1.7762 MeV	$2.5523204 - 6.0130413(E^2) + 12.234064(E^4) - 10.181023(E^6) + 2.6412968(E^8)$
2.	Alpha-2 1.4721 MeV	$\frac{2.1251348 + 12.347678(E^2) - 6.1503582(E^4)}{1 + 10.208672(E^2) + 1.5883816(E^4)}$
3.	Lithium-1 1.0133 MeV	$-17.343464 + 19.971642(E) - 9.4474929(E^{1.5}) + 18.573458(e^{-E})$
4.	Lithium-2 0.8398 MeV	$5.4181203 + 406398743(E^2) - 4.348119(e^E) + 1.5050993(E^{0.5})$

The Li^6 neutron conversion reaction produces a triton and alpha particles which are emitted in the opposite directions with 2.73MeV and 2.05MeV, respectively. Figures 4-17 and 4-18 show the $\bar{E}_m^i(\mathbf{X})$ and $\bar{X}_m^i(\mathbf{E})$ for these ions. Their empirical relations are tabulated in tables 4-4 and 4-5.

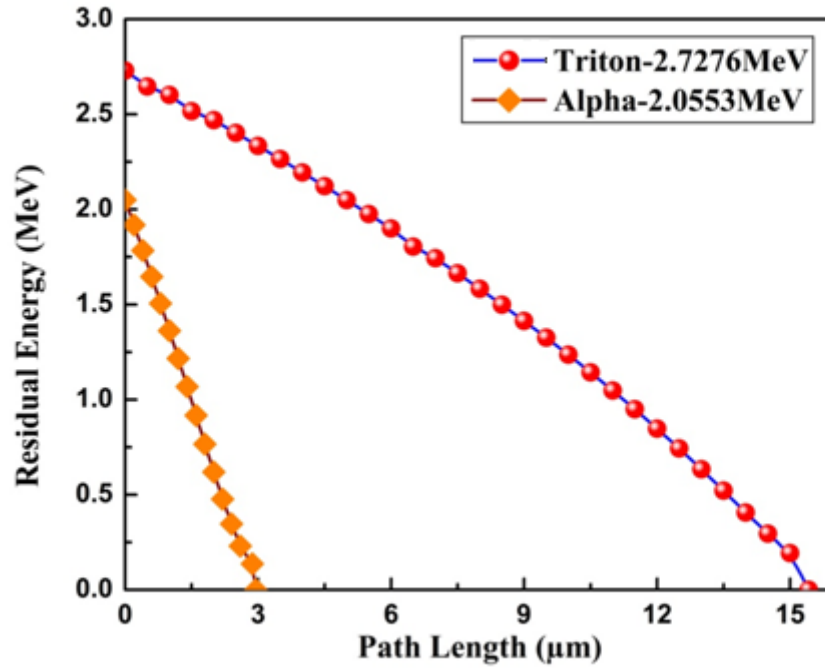


Figure 4-17 Interpolated residual energy versus path length data for transport of Lithium-6 neutron conversion ions in Gold (Au)

Table 4-4 Empirical fit of residual energy $\bar{E}_m^i(\mathbf{X})$ after a path length ‘X’ in gold (Au) for Li^6 conversion ions.

1.	Triton 2.73MeV	$2.7172445 - 0.11176175(\mathbf{X}) - 0.0089786184(\mathbf{X}^2) + 0.001417008(\mathbf{X}^3) - 122.55053 \times 10^{-6}(\mathbf{X}^4) + 3.422596 \times 10^{-6}(\mathbf{X}^5)$
2.	Alpha 2.05MeV	$\frac{2.0500052 - 1.9281259(\mathbf{X}) + 0.61313862(\mathbf{X}^2) - 0.065883559(\mathbf{X}^3)}{1 - 0.6231768 \times 10^{-6}(\mathbf{X}) + 0.11893467 \times 10^{-6}(\mathbf{X}^2) - 0.0046028961 \times 10^{-6}(\mathbf{X}^3)}$

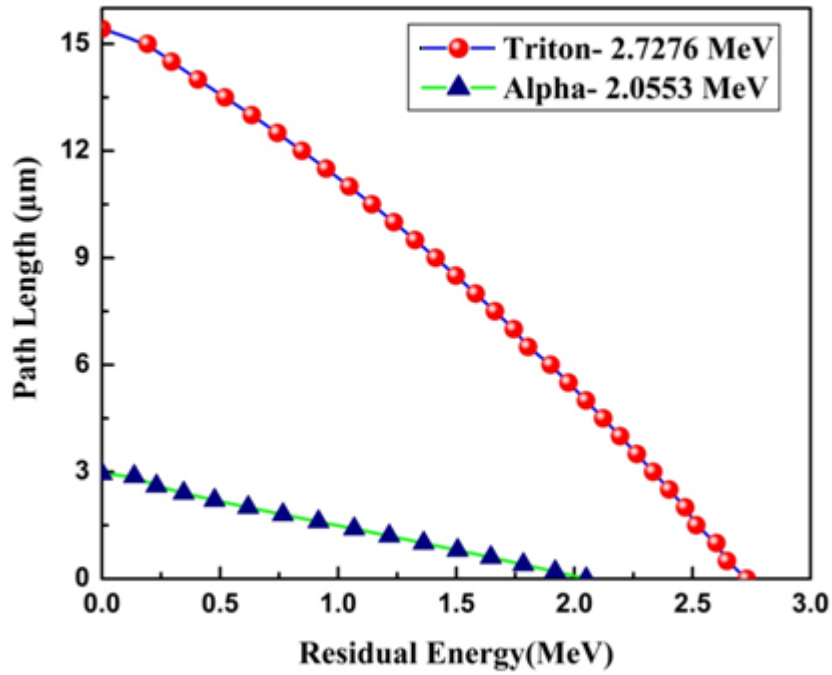


Figure 4-18 Interpolated path length versus residual energy data for transport of Lithium-6 neutron conversion ions in Gold (Au)

Table 4-5 Empirical fit of path length $\bar{X}_m^i(E)$ to reach a residual energy 'E' in gold (Au) for Li^6 conversion ions.

1.	Triton 2.73MeV	$15815419 - 4.1324825(E) - 3.7154129 \times 10^{-7}(E^2) - 9.1162815 \times 10^{-14}(E^3)$
2.	Alpha 2.05MeV	$\frac{3283480.3 + 12.392507(E) - 6.8270751 \times 10^{-6}(E^2)}{1 + 5.4093245(E) - 4705928.9(E^2)}$

4.8.2 Simulation of detector efficiency

Figure 4-19 shows the simulation of ϵ_{int} of a detector coated with B^{10} and Li^6F converter materials with varying gold dead layer thickness. The dead layer thickness is varied from 0.1 μm to 1.1 μm to emulate that encountered in practical devices. The

efficiency decreases with increasing thickness. The LLD energy for this simulation was kept at 300 keV[49]. From figure 4-19 it can be observed that the ϵ_{int} of a Si diode

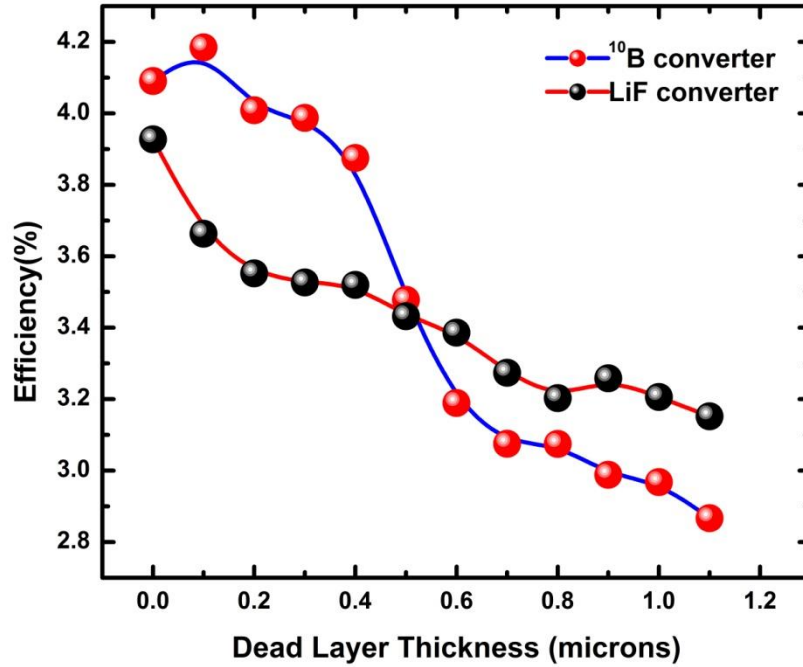


Figure 4-19 Variation of the intrinsic neutron detection efficiency as the thickness of the dead layer is varied. Efficiency variation for both Boron and Li⁶F converter materials are shown

generally decreases as the thickness of a sandwiched gold dead layer is increased. This is explained in terms of the effect of further reduction in the initial kinetic energy of the conversion reaction ions before they enter the depleted silicon region. In the model without the inclusion of the dead layer, most of the neutron conversion ions have their initial kinetic energy at or slightly above the LLD energy level. With the inclusion of dead layer, the events generating these are now prevented from getting registered as true neutron events because of the lower energy deposition. In this simulation, the thickness of the converter material was chosen to be the optimized value at t_c , from a dead layer-

sans detector as discussed in section 4.6. Hence, the thicknesses of the B^{10} and Li^6F converter materials are 2.5 and 25 μm , respectively. It is seen that the variation in efficiency with respect to the thickness of the dead layer follows different trends. For dead layer thicknesses less than 0.4 μm , the efficiency of a B^{10} coated diode is higher than that observed in the Li^6F counterpart. For dead layer thickness higher than 0.6 μm , a B^{10} coated diode has a lower efficiency than a Li^6F coated one. For the thicknesses of the dead layer between 0.4 μm to 0.6 μm , there is a steep decrease in efficiency from 3.9 % to 3.1% in the B^{10} coated diode, whereas the efficiency remains approximately constant at a value of 3.5% for a Li^6F coated one in this range of thickness. In both the cases, the efficiency reduces to $\sim 3\%$ at a dead layer thickness of 1 μm .

The higher efficiencies observed in the case of the B^{10} coated diodes as compared to the Li^6F coated ones for low values of dead layer thickness below 0.4mm is due to the higher neutron absorption cross section for B^{10} (3840 barns), which is almost four times higher than that of Li^6F (940 barns). From figure 4-15, it is observed that there are two paths in the B^{10} neutron capture, viz., a reaction resulting in alpha-1 (1.7762 MeV) and lithium-1 (1.0133 MeV) with 6% branching ratio and another reaction resulting in alpha-2 (1.4721 MeV) and lithium-2 (0.8398 MeV) with 94% branching ratio. In the case of Li^6F , the ions are triton (2.7276 MeV) and alpha (2.0553 MeV). The penetration depths of alpha-1, alpha-2 and the Li^6F conversion alpha in gold layer are 2.55 μm , 2.13 μm and 2.95 μm , respectively. The lithium ions from B^{10} neutron capture (lithium-1 and lithium-2), being heavier than the triton (15.42 μm penetration depth) lose larger percentage of their energy ($\sim 80\%$) and come to rest at 1.23 μm and 1.07 μm , respectively. Therefore, the combined effect of alpha and lithium ions contribute to the ϵ_{int} of boron coated diodes upto 1 μm . Beyond 1 μm , the contribution is from the alpha particle alone. This is the reason for the low ϵ_{int} value in Boron coated diodes.

Triton being lighter in mass as compared to lithium loses lesser energy (~5%) as it traverses gold for comparable thickness and therefore contributes significantly to the ϵ_{int} for thicknesses larger than 0.6 μm . The changeover from Boron to Lithium in ϵ_{int} is essentially a depiction of the energy deposited by the ions upto a maximum depth of ~ 2.95 μm .

4.9 Conclusions

Monte Carlo simulations of straight trench detectors and planar neutron detector operation were successfully performed in conjunction with TRIM code to estimate and study their important performance characteristics. It was found that the maximum achievable efficiency (ϵ_{int}) of a planar semiconductor neutron detector is ~4% for both B^{10} and Li^6F converter materials at a critical thickness t_c of 2.5 μm and 25 μm , respectively. The effects of LLD settings on the intrinsic detection efficiency were also studied for a B^{10} coated detector and it was concluded that the efficiency is highly sensitive to the LLD settings. Further, the effect of dead layer thickness on ϵ_{int} was investigated. It was found that a 1 μm thick metal electrode of gold (Au) sandwiched between the silicon diode and the converter material, reduces the intrinsic detection efficiency from the maximum value of 4% to a value of 3%.

CHAPTER 5 Summary, conclusions and future scope.

5.1 Summary

In the present work, novel embedded readout electronics for existing portable radiation instruments have been designed and implemented. The cost effective and reliable designs were made possible by the use of recent advanced mixed signal programmable system on chip platform. A design optimization study of low cost planar neutron detector has also been carried out. Brief conclusions of each of these studies are given below

- (a) The potential of recent reconfigurable mixed signal hardware platforms to implement cost effective and reliable readout electronics for portable radiation measurement applications is established after a thorough survey of different platforms and their functional capabilities. The importance of low cost alternatives in detectors for achieving cost effective designs is also established.

- (b) A compact, reliable readout for Geiger Mueller detector was designed and implemented using the PSoC platform. The novel feature has been built in the design in which all the peripheral functions in a GM survey meter like, high voltage bias regulation and data communication along with the core counting function are integrated on to a single chip. The single chip implementation improves reliability by increased immunity to external interference and by providing mechanical ruggedness through miniaturization.

(c) Novel embedded pulsed reset technique based readout electronics for an alpha spectrometer has been successfully designed and implemented. The pulsed reset technique controls the functioning of the feedback network of the preamplifier stage using a solid state analog switch. In addition to this the spectrometer also features novel designs like ramped high voltage supply for detector biasing and data communication to PC based graphical user interface. Again the single chip implementation of these features improves the reliability of the portable spectrometry application at an affordable cost.

(d) Design optimization studies of low cost semiconductor neutron detectors in planar configuration have been carried out using Monte Carlo simulations. Preliminary work is done in optimizing the neutron converter material thickness for maximum intrinsic neutron detection efficiency for a planar neutron detector. Additional simulation of the effects of dead layer inclusion on the efficiency is performed by suitable modifications in the existing Monte Carlo model thus establishing the effects of dead layer in a practical device.

5.2 Suggestions for future work

In general the count rate of pulses from GM tube, when exposed to gamma photons, is affected by both the actual exposure rate as well as the gamma energy. This is because the intrinsic detection efficiency of a GM tube itself is different at different gamma energies. In the present work on GM counter embedded readout the design is suitable for measuring accurate dose rates only with an energy compensated GM tube. An energy compensated GM tube is covered with a thin layer of metals such as lead and/or

tin [106]. This metal covering is done so as to empirically match the efficiency versus energy curve to the exposure per gamma photon versus energy for a given tube. In this embedded design a provision for manual entry of gamma energy can be provided so that this empirical compensation can be augmented in cases where the gamma energies in the application of concern are known *apriori*. This augmentation is made possible once the survey meter sensitivity versus energy data [107] is available and can be incorporated as a look up table in the firmware. The correction factors from this look up table can be included in the engineering conversion codes of the firmware. Additional features like battery monitoring and test can be included.

The alpha spectrometer application can be further improved by incorporating features such as isotope identification, user controlled ramping rate, long term stability monitoring and battery monitoring in the firmware. Further modifications in the reset switch control waveform and the use of recent advanced ultra low charge injection switches can be incorporated in the hardware to reduce the residual errors in pulse height measurement thereby enhancing the resolution.

The neutron detector optimization simulations can be further improved by incorporating composite dead layers in the unit cell. Further advanced semiconductor detector alternatives like neutron converter coated avalanche photodiodes with statistically varying multiplication factors can be substituted in place of simple PIN diode based structures in the Monte Carlo simulations for efficiency calculations.

APPENDIX A

List of embedded C- programs

A.1 Embedded C program listing for PSoC based GM counter readout design.

The embedded C program for measuring the pulse rate of GM output in a PSoC -1 IC is listed here. The program consists of a continuous loop in the main which updates the count rate on a timer overflow interrupt and updates a windows® hyperterminal® based GUI with the dose rate.

```
#include<m8c.h>// part specific constants and macros
#include"PSOCAPI.h"// PSoC API definitions for all User Modules
#include<stdlib.h>//standard library for float to integer conversions
#define GATETIME gatetime(int)// give the option of gating time for
counting pulses in units of seconds here.
#define SENSITIVITY sensitivity(double)//write the value of instrument
sensitivity in units of (CPS/nGy perhour) obtained through calibration
experiments here.
#pragma interrupt_handler timer_ovf//perform interrupt service routine
at the moment of timer interrupt.
#pragma interrupt_handler counter_ovf//perform batch value increment for
counter on ovflo interrrupt.

/*=====Start                                     Global
variables=====*/
int seconds;
int batch;
//char *dose;
/*=====End                                     Global
variables=====*/

//-----
// C main line
//-----
void main(void)
{
    /*=====Start                                     user           module
    intialisation=====*/
    M8C_EnableGInt ;//enable all interrupts of M8C processor
    BUFFER_Start(BUFFER_LOWPOWER);//start integrator buffer with low
power setting
    Relax_Start(Relax_LOWPOWER);//start the relaxation oscillator-
switched capacitor block in low power mode
```

```

        Integrator_Start(Integrator_LOWPOWER); //start the switched
capacitor integrator in low power
        COMP_Start(COMP_LOWPOWER); //start the comparator in low power mode
        DigBuf_Start(); //start the digital buffer module in low power mode
        CLAMPOUT_2_Start(CLAMPOUT_2_LOWPOWER); //start the positive
clamping source
        CLAMPOUT_1_Start(CLAMPOUT_1_LOWPOWER); //start the diode
compensation source
        Timer16_EnableInt(); //Ensure timer interrupt is enabled
        Timer16_Start(); /*start the timer also*/
        Counter8_EnableInt(); //enable the counter interrupts
        Counter8_Start(); /* start the counter */
        UART_1_Start(UART_PARITY_NONE); //start the UART module

        /*=====End user module
initialisation=====*/

        /*=====Start main function variables
declaration=====*/
        /*=====End main function variables
declaration=====*/
        seconds=0;
        batch=0;
        UART_1_PutChar(12);
        while(1)
        {
                /*do nothing just wait for timer and counter
interrupts(infinite while loop)*/
        }
}
/*=====Start timer interrupt
subroutine=====*/
void timer_ovf(void) //interrupt routine for timer 16 interrupt
{
        int totcount=0; //declare integer variable for holding the total
count.
        float countpersec=0, DOSERATE=0; //floating point variables for
persecond count and doserate.
        char dosebuf(25); //character array for holding formatted string for
doserate display in hyperterminal.
        seconds += 1; //increment the seconds value by unity upto the
GATETIME value.
        if(seconds == GATETIME)
        {
                seconds=0; //initialise "seconds" for the next round and
proceed.
                Counter8_Stop(); //temporarily stop the counter for reading
out the count value
                totcount=(batch*255)+(255-Counter8_bReadCounter()); //read
the current counter value and evaluate the total count value and store
in the ivalue variable
                batch=0; //reinitialize the value of batch.
                countpersec=totcount/GATETIME; //evaluate counts per second.
                DOSERATE=countpersec/SENSITIVITY; //evaluate the actual dose
rate interms of nGy.
                Counter8_WritePeriod(255); //re-initialise the counter
                Counter8_Start(); //restart the counter
                csprintf(dosebuf, "\n\r%fnGyph%c", DOSERATE, '\0'); //function
to produce formatted string equivalent(with null termination) of dose
rate.

```

```

        UART_1_PutString(dosebuf); //send the formatted (null
terminated) string to hyperterminal.
    }
}

/*=====Start counter interrupt
subroutine=====*/
void counter_ovf(void)
{
    batch+=1; //increment the variable batch by 1 when the 8-bit
counter overflows.
}
/*=====End of
program=====*/

```

A.2 Embedded C program listing for PSoC based alpha particle spectrometer readout design.

The C program for pulse height digitization using the embedded pulsed reset scheme for alpha particle spectrometer is listed here. The program consists of a continuous loop which digitizes the pulse height on the event of a pulse edge GPIO interrupt and communicates the results to a PC based GUI. In addition to this the main loop also generates the reset waveform. The look up table at the start of the program is used for the saw tooth generation in HV regulation using the Direct Memory Access (DMA) technique.

```
/* PROJECT DESCRIPTION
 * Sawtooth Lookup of length 128 is created in a flash array and the
 * values are updated continuously to a DAC.
 * The update rate and the number of points in the sawtooth look-up table
 * determine the frequency of the output sawtooth wave.
 * The values from the look-up table are updated into the DAC using a
 * DMA.
 * The DMA is set to update values on a hardware trigger.
 * The hardware trigger is given by a Timer.
 */

#include<device.h>
#include<cytypes.h>

// #define TABLE_LENGTH 256
#define TABLE_LENGTH 201
#define DMA_BYTES_PER_BURST 1
#define DMA_REQUEST_PER_BURST 1

/* This table stores the 128 points in Flash for smoother saw tooth wave
generation */

CYCODE const uint8 sawTable[TABLE_LENGTH] =
{
    0,1,2,3,4,5,6,7,8,9,10,
    11,12,13,14,15,16,17,18,19,20,
    21,22,23,24,25,26,27,28,29,30,
    31,32,33,34,35,36,37,38,39,40,
    41,42,43,44,45,46,47,48,49,50,
    51,52,53,54,55,56,57,58,59,60,
    61,62,63,64,65,66,67,68,69,70,
    71,72,73,74,75,76,77,78,79,80,
    81,82,83,84,85,86,87,88,89,90,
    91,92,93,94,95,96,97,98,99,100,
```



```

101,102,103,104,105,106,107,108,109,110,
111,112,113,114,115,116,117,118,119,120,
121,122,123,124,125,126,127,128,129,130,
131,132,133,134,135,136,137,138,139,140,
141,142,143,144,145,146,147,148,149,150,
151,152,153,154,155,156,157,158,159,160,
161,162,163,164,165,166,167,168,169,170,
171,172,173,174,175,176,177,178,179,180,
181,182,183,184,185,186,187,188,189,190,
191,192,193,194,195,196,197,198,199,200
};

/* Variable declarations for DMA .
 * These variables are defined as global variables to avoid "may be used
 before being set" warning
 * issued by the PSoC 5 compilers MDK/RVDS. In this case these variables
 are automatically initialized to zero */

uint8 DMA_Chain; /* The DMA Channel */
uint8 DMA_TD[1]; /* The DMA Transaction Descriptor (TD) */
unsignedshortint a;
volatileint8 i_ramp; // Vars changed in int-handler MUST be
declared as volatile
volatileint8 increment;
volatileint8 delay_index;
volatileint8 POS_EDGE_FLAG;

//CY_ISR(MyCustomISR)
CY_ISR(Timer_ramp_ISR)
{
    staticchar LedState = 0;
    Timer_1_ReadStatusRegister(); // This clears the sticky TC Bit
(Datasheet pgs. 11 and 28)
    increment=i_ramp;
    i_ramp++;
    increment=increment-i_ramp;
    LED_Write(LedState);
    LedState = ~ LedState;
}
CY_ISR(POS_EDGE_ISR)
{
    POS_EDGE_FLAG=1; /*This happens on a Positive edge of Preamp*/
}

void InitializeHardware(void)
{
    /*Enable Global interrupts*/
    CyGlobalIntEnable;
    //isr_1_StartEx(MyCustomISR);
    isr_1_StartEx(Timer_ramp_ISR);
    isr_2_StartEx(POS_EDGE_ISR);
    /* Start the VDAC and Timer components */
    //cap_discharge_Write(1);
    VDAC8_Start();
    IDAC8_Start();
    Timer_Start();
}

```

```

    Timer_WritePeriod(3);          /* Timer period is set to 3
resulting in a period of 1 us(4 cycles)*/
    UART_TX_1_Start();
//PGA_1_Start();
    Timer_1_Start();
    Comp_1_Start();                /*start the PWM coparator*/
    POS_EDGE_INTGEN_Start();/*start the pos edge gen comparator of the
state machine*/
    VDAC8_1_Start();                /*start the PWM VDAC*/
    VDAC8_1_SetValue(0);            /*testing work ignore*/
/*Start the interrrupt function*/
    LED_Write(1);
    //Pin_1_Write(1);
    Opamp_1_Start();
    PGA_1_Start();
    Adc_1_Start();
    Adc_1_StartConvert();
#if (defined(__C51__)) /* Source base address when PSoC3 is used */
    #define DMA_SRC_BASE (CYDEV_FLS_BASE)

#else/* Source base address when PSoC5 is used */
//#define DMA_SRC_BASE (&sineTable[0])
#define DMA_SRC_BASE (&sawTable[0])
#endif

    #define DMA_DST_BASE (CYDEV_PERIPH_BASE) /* Destination base
address */

    /* DMA Initialization is done for the DMA channel
    * Bytes per burst = 1, (8 bit data transferred to VDAC one at a
time)
    * Request per burst = 1 (this will cause transfer of the bytes
only with every new request)
    * High byte of source address = Upper 16 bits of Flash Base
address for PSoC 3,
                                = HI16(&sineTable) for PSoC 5
    * High byte of destination address = Upper 16 bits of peripheral
base address */
    DMA_Chan = DMA_DmaInitialize(DMA_BYTES_PER_BURST,
DMA_REQUEST_PER_BURST, HI16(DMA_SRC_BASE), HI16(DMA_DST_BASE) );

/* Allocate the TD for DMA channel */
    DMA_TD[0] = CyDmaTdAllocate();

    /* Configure the TD
    * Transfer count = table_length (number of bytes to transfer for
a Sine Wave)
    * Next Td = DMA_TD[0] (in this example, the TD loops back to the
same TD.
    * Configuration = The source address should be incremented for
every byte of transfer
    * to transfer all the samples for a Sine Wave */
    CyDmaTdSetConfiguration(DMA_TD[0], TABLE_LENGTH, DMA_TD[0],
TD_INC_SRC_ADR);

/* Configure the DMA_TD[0] for address
    * Source address = Lower 16 bits of sineTable array

```

```

        * Destination address = Lower 16 bits of VDAC8_Data_PTR register
    */
    //CyDmaTdSetAddress(DMA_TD[0], LO16((uint32)sineTable),
    LO16((uint32)VDAC8_Data_PTR) );
    CyDmaTdSetAddress(DMA_TD[0], LO16((uint32)sawTable),
    LO16((uint32)VDAC8_Data_PTR) );
    //CyDmaTdSetAddress(DMA_TD[0], LO16(DMA_SRC_BASE),
    LO16(DMA_DST_BASE) );

    /* Map the TD to the DMA Channel */
    CyDmaChSetInitialTd(DMA_Chan, DMA_TD[0]);

    /* Enable the DMA channel */
    CyDmaChEnable(DMA_Chan, 1);
}

int main()
{
    InitializeHardware();
    //cap_discharge_Write(0);
    delay_index=0;
    i_ramp=2;
    while(i_ramp<40)
    {
        VDAC8_1_SetValue(i_ramp);
    }
    Timer_1_Stop();
    isr_1_Stop();
    while(1)
    {
        if (POS_EDGE_FLAG==1)
        {
            Adc_1_IsEndConversion(adc_WAIT_FOR_RESULT);
            a=Adc_1_GetResult16();
            sprintf(x,"%05u\t",a);/*Formatting the ADC value*/
            UART_TX_1_PutString(x);/*Formatted data to GUI*/

            CPU_RESET_OUT_Write(1);/*Burst generation for reset*/
            CPU_RESET_OUT_Write(0);/*Burst generation for reset*/
            CPU_RESET_OUT_Write(1);
            CPU_RESET_OUT_Write(0);
            CPU_RESET_OUT_Write(1);
            CPU_RESET_OUT_Write(0);
            IDAC8_SetValue(255);/*ramping part of reset burst*/
            IDAC8_SetValue(190);
            IDAC8_SetValue(127);
            IDAC8_SetValue(63);
            IDAC8_SetValue(0);
            while(delay_index<=10)
            {
                delay_index++;/*delay for time adjustments*/
            }

        }
        POS_EDGE_FLAG=0;
    }
}

/* [] END OF FILE */

```

APPENDIX B

Mixed signal PSoC platform for auxiliary lab applications

In addition to the core work which relates to design of detector electronics using the PSoC platform, this thesis also describes design and development of other lab automation related projects done for getting familiarization with the steps of application development using the PSoC platform. These include

- a) PSoC based X-Y stage control system for generating micro patterns in substrates.
- b) Development of a High Voltage Pulsed Power Supply (HVPPS) with PSoC based Pulsing control and
- c) The development of a wireless electronic hand tremor monitoring system.

B.1 PSoC based X-Y table control system for creating straight trench patterns in substrates.

B.1.1 Introduction

Laser patterning of thin films and substrates offers new possibilities in lithography and rapid prototyping of several innovative devices. The patterns developed using this technique vary from simple micro trenches to multiple micro pillars depending on the application [108]. Owing to advantages such as non-contact nature of the laser-material interaction, flexibility/ ease of automation and the ability to produce fine features makes the direct laser writing, a well established technique.

A typical laser micromachining system consists of a laser source, beam focusing optics and an X-Y motorized translation stage. The precise movement and control of the X-Y stage plays a crucial role on the micro patterns generated, which in turn affects the final performance of the fabricated devices. Keeping this in mind, several ultra precision X-Y stages have been developed and commercialized [109].

In the present work, an inexpensive X-Y stage control system using PSoC interface and LabVIEW based control program is developed. With this system, a variety of micro patterns can be created by adjusting pitch between features, speed and direction. All these control signals are made available through a user friendly menu driven virtual instrument interface.

B.1.2 LabVIEW.

PSoC-1 is the basic version which is used in this work. Laboratory virtual instrumentation engineering workbench (LabVIEW) is a platform and development environment utilizing a visual programming language from M/s National Instruments. LabVIEW can be operated on a variety of platforms including Microsoft windows for data acquisition, instrument control and industrial automation. In the present work, a user friendly menu driven experimental automation of the micro patterning process is developed with virtual instrument programming.

B.1.3 Micro pattern generator design

Figure B.1-1 shows the indigenously developed experimental setup for micro patterning on a substrate. It consists of an X-Y table mounted with a sample holder and stepper motors. The stepper motors can control the translation of the X-Y table with a resolution of 1 μ m in both X and Y directions. The stage set up shown can be directly

fitted on to a vacuum chamber and an electronically activated slit for controlling the laser beam from a picosecond laser as shown in figure B.1-2.

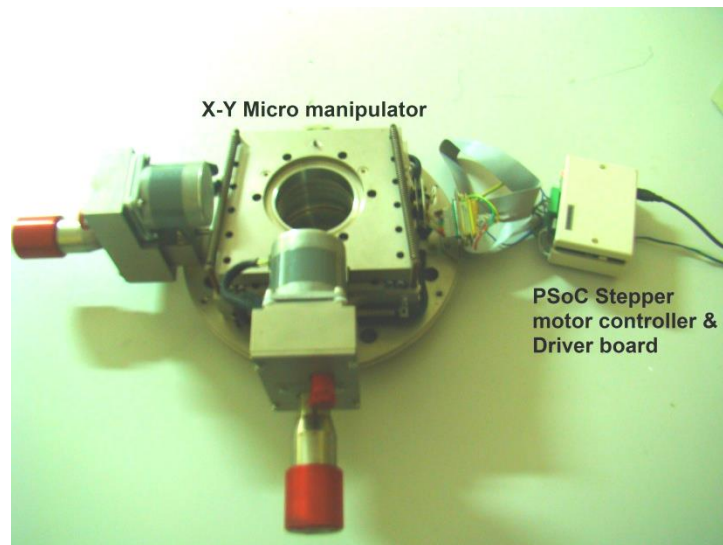


Figure B.1-1 Photograph of the X-Y micro positioning stage with its PSoC based stepper motor controller

The present system is designed and implemented based on the design given in [110]. The PSoC 1 IC is programmed to generate the data sequences for driving each of the X and Y control stepper motors. The data thus generated are fed to two L298 dual full bridge driver ICs to act as a high current and high voltage buffer between the TTL outputs of the PSoC and the high current motor coils. The motors are operated on a 6 V power supply with each of the windings drawing 500 mA on maximum load. The screenshots of the user interface with real time display of progress of the micro patterning process is shown in the subsequent figures for various pitch sizes. A precise control of the spacing between the micro-patterns is achieved using this system as shown in the figure B.1-4.

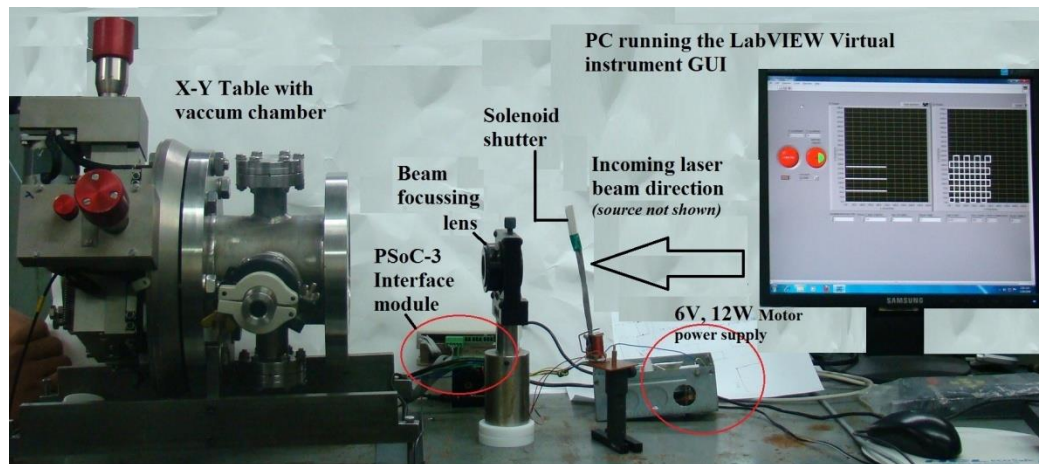


Figure B.1-2 Complete set up for laser patterning process with the X-Y micro positioning stage attached to a vacuum chamber

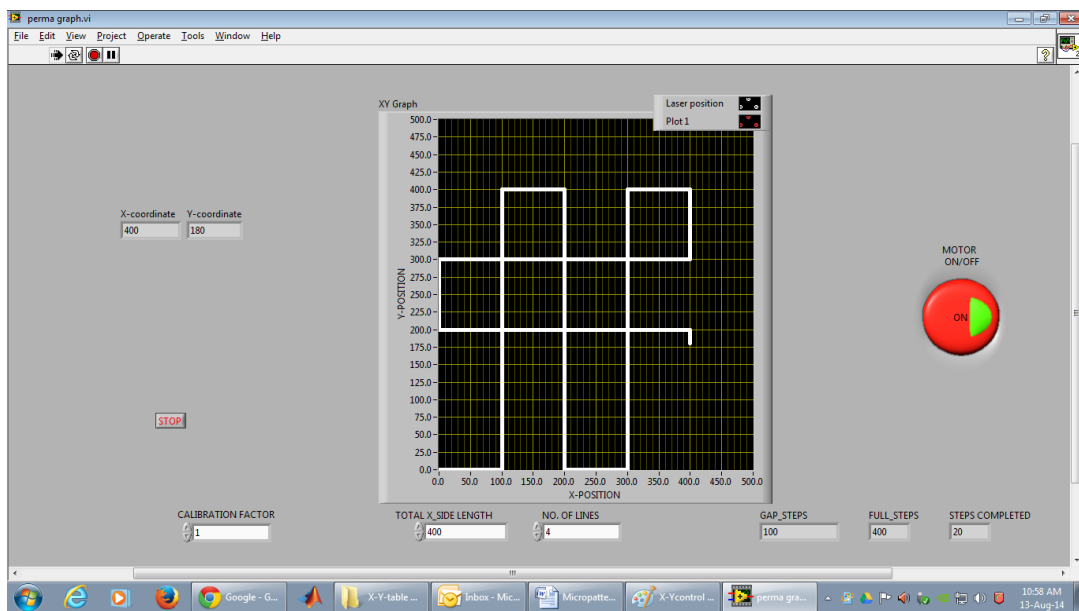


Figure B.1-3 User interface with real-time monitoring of the patterning process

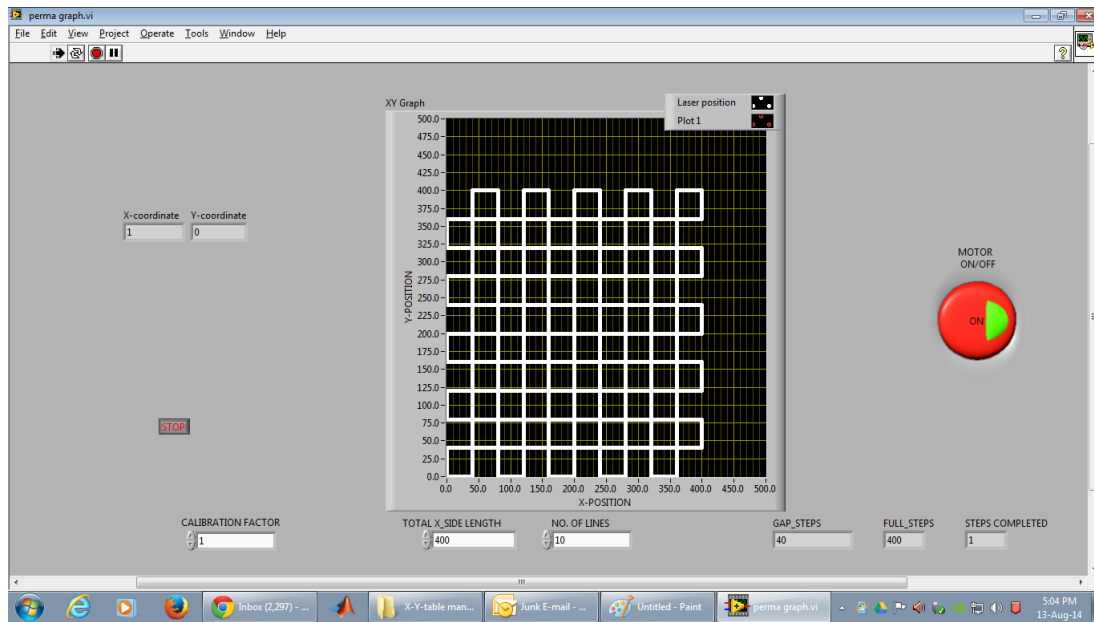


Figure B.1-4 User interface while patterning 10 lines within a distance of 400 μm shows the precision of the spacing between the lines.

B.2 PSoC based High Voltage Pulsed Power Supply (HVPPS) system for ion mobility spectrometer (IMS).

B.2.1 Introduction

IMS is a widely used technique of ion separation in gaseous phase based on the differences of ion mobilities under an electric field. This technique is used for the detection and monitoring of explosives, chemical warfare agents and in environmental / industrial assessments for toxic chemicals. The core controlling element of the IMS is the HVPPS, which operates an ion gate by pulsing between a voltage of -3.5 KV and 3 KV with a rise/ fall time of 100 μ s. This appendix explains details of design of this core control element with a PSoC. The figure B.2-1 below shows the schematic cut section diagram of an IMS.

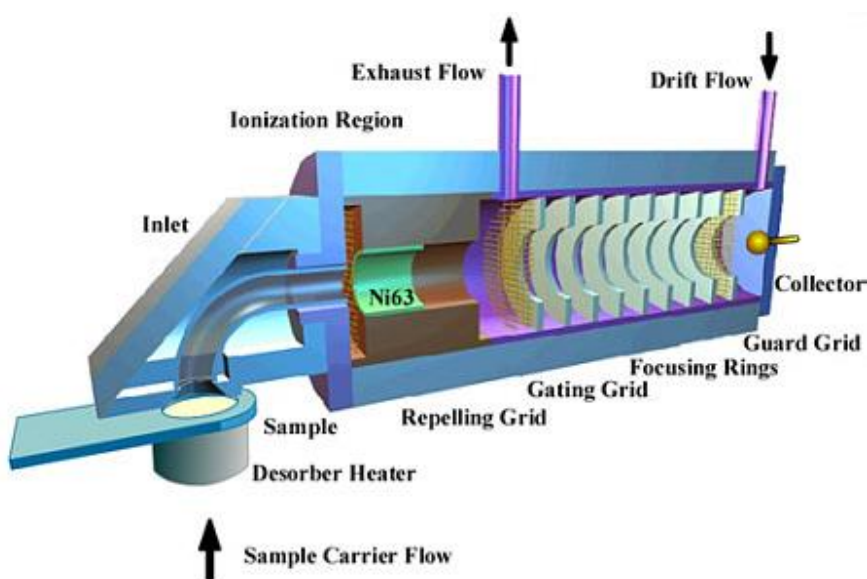


Figure B.2-1 Structure of the drift chamber in an Ion Mobility Spectrometer
Courtesy (<https://www.smithsdetection.com>, M/s Smiths detection, USA)

As shown in the figure B.2-1 the IMS has the following components (a) an ion source (b) an ion gate grid (c) a drift tube with a series of focusing rings and (d) a collector plate.

The ion source consists of a heater assembly, an inlet tube and an ionization chamber. Chemical samples which are to be analyzed are drawn-in into the IMS inlet tube along with a carrier gas which is usually the ambient air. The samples are best analyzed when the analytes are in vapor phase. Though many explosive compounds are volatile and can be directly fed, some in volatile compounds have to be heated to create enough vapor phase for detection. This is achieved by the inlet desorber and heater. Ionization of the sample vapour is achieved using a radioactive Ni-63 ring which emits energetic beta particles with an average energy of 17 KeV [111]. The ions thus generated inside the ionization chamber are injected into the drift tube using a high voltage pulse supplied to the ion gating grid. Inside the drift tube the ions move in a counter-current of dry air or dry nitrogen towards the collector plate under the influence of an electrostatic field. The counter-current is provided to avoid clustering of ions with water molecules. Due to their collision motion inside the drift tube, ions of different mass and different collision cross section reach the collector plate at different times. Upon reaching the collector plate each ion produces a specific current signal.

B.2.2 HVPPS system design

The gate electrode in an IMS is required to be biased in a pulsed fashion using a high voltage of -3.5KV which momentarily should rise to -3KV and should remain at this value for ~1.5 ms. The rise time requirement is that it should be less than 100 μ s. Various design options for pulsed HV operation were studied and were found to fall short of requirements in rise time characteristics or in HV level. A compact HV pulsing system with commercially available regulated 3.5 KV HV module using a PSoC based pulsing system was implemented. Figure B.2-2 describes the compact high voltage system with pulsing control for the IMS. The photograph of the complete assembly is shown in figure B.2-5. The core HV generation function is achieved by the boost converter circuit

consisting of the switching MOSFET Q4 and the transformer T1. The transistors Q1, Q2 and Q3 provide the GATE drive for the MOSFET Q4. The output of the voltage multiplier and the filter network, which is connected to the secondary of the transformer T1 maintains a HVDC of 3.5 KV at P. through a voltage divider network a lower negative voltage of -3 KV is maintained at S. The changeover between these two voltages is achieved by a switching network consisting of a high speed switching power MOSFET – IXTF 1N450 (Q5), which is driven by an opto-coupler based gate circuit and a chain of high voltage diodes.

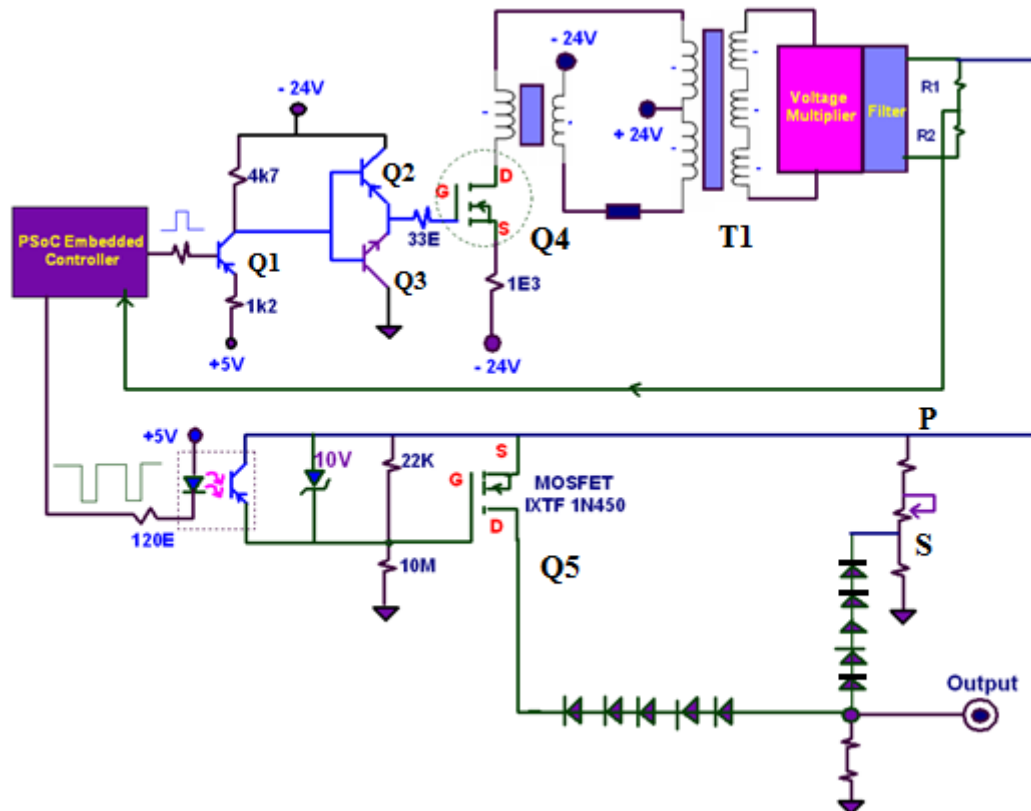


Figure B.2-2 Block diagram of the HVPPS with PSoC based pulsing control

A major challenge in the design of switched mode high voltage power supplies is the feed-through of the switching signal into the power supply output. This condition is shown in the figure B.2-3 wherein, the 48 kHz ripple is explicitly seen with peak-to-peak amplitude of 6 V riding on the negative voltage of 3.5 KV. A special filtering scheme was

designed to reduce the switching ripple with a stand-alone high voltage passive filter connected to the HVPPS output before feeding it to the IMS gate electrode. The results after the inclusion of this HV filter is shown in figure B.2-4. The high voltage pulsing waveform and the signal waveforms from the IMS collector plate trans-impedance amplifier shown in the subsequent figures.

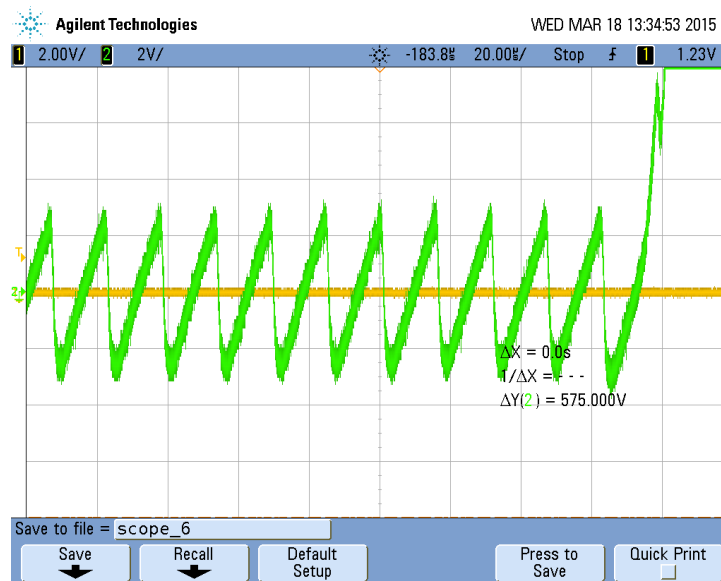


Figure B.2-3 Switching signal feed through in the HV output

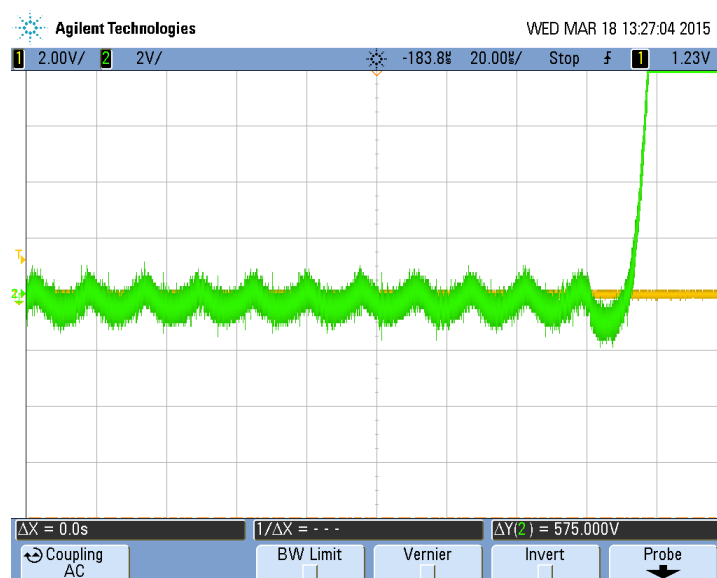


Figure B.2-4 Reduction in switching ripple with the inclusion of HV passive filter

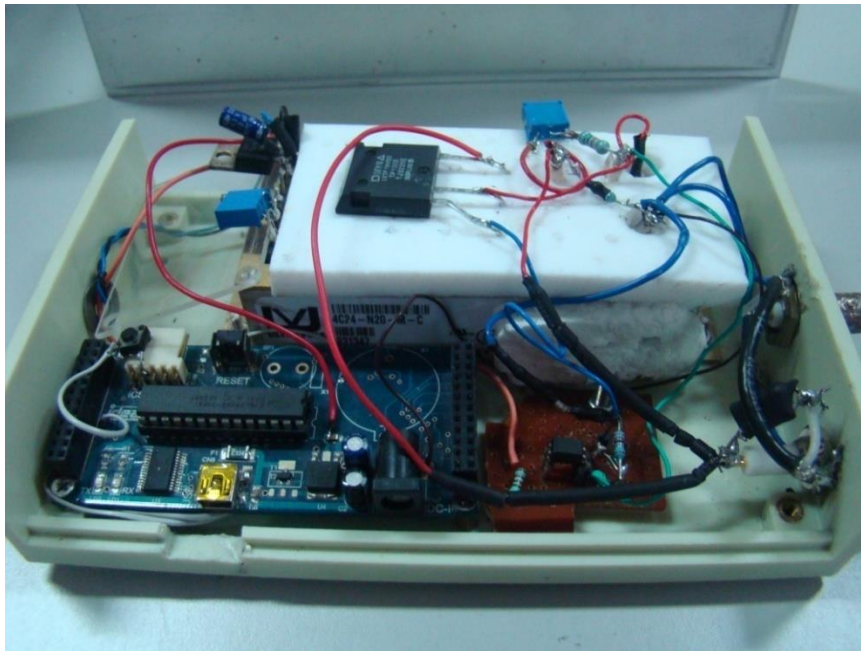


Figure B.2-5 Compact assembly for the IMS HVPPS with the PSoC application board shown

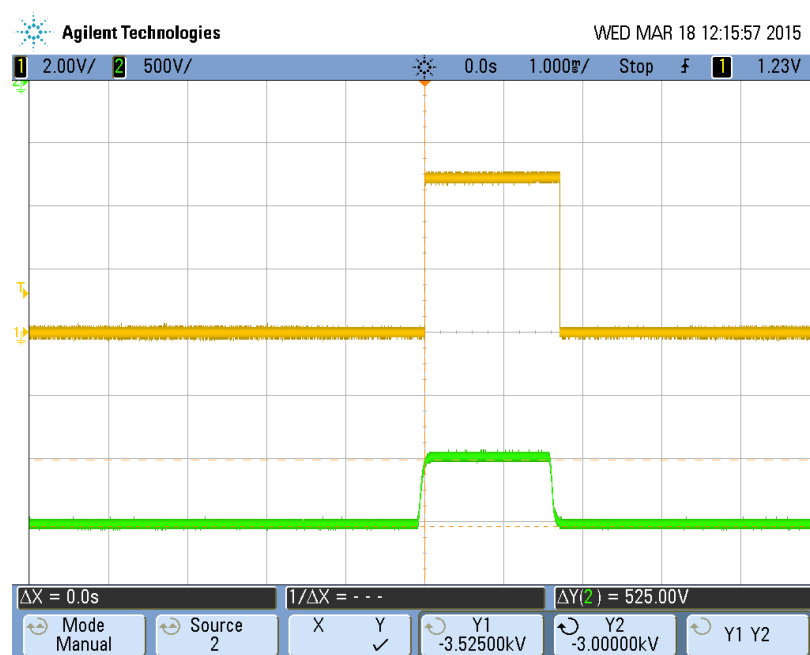


Figure B.2-6 The final filtered waveform with the pulsing operation shown

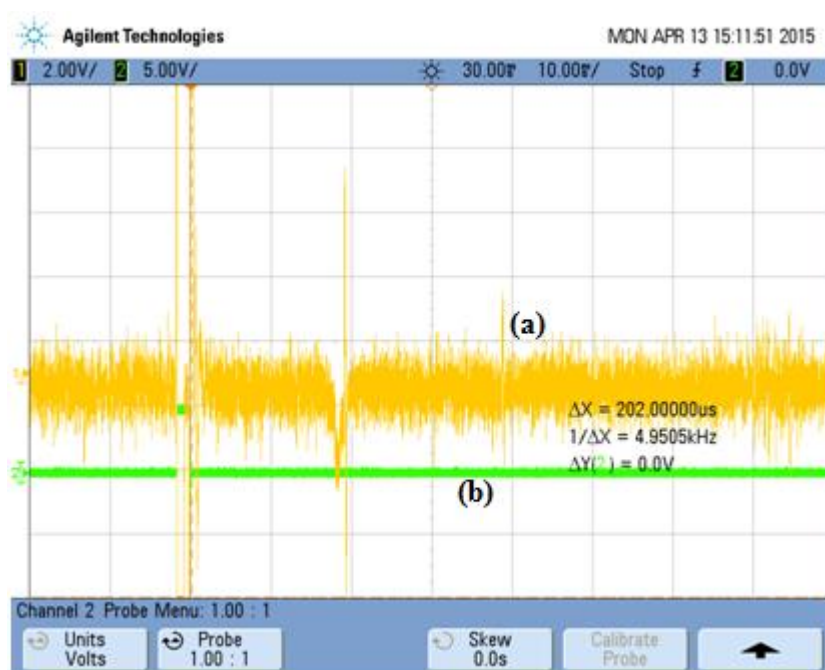


Figure B.2-7 The output of the trans-impedance amplifier connected to the collector plate of the IMS chamber. The initial dip indicates the presence of oxygen molecules

The functionality of the HVPPS is verified using the acquisition of trans-impedance amplifier output in a DSO as shown in the figure B.2-7. The waveform (a) shows the trans-impedance amplifier output and the waveform (b) shows a time-marker signal generated from the PSoC to mark the instant of the HV pulsing operation. This instant coincides with the initiation of the ion drift in the chamber and hence, this instant is taken as the time reference from which the drift times of the ions are measured. The chamber operation with the HVPPS designed in this work was tested by pumping ambient air inside the chamber. A dip is observed in the trans-impedance amplifier output (a), which is the result of oxygen molecules reaching the collector plate.

B.3 PSoC based wireless Hand tremor monitoring system

B.3.1 Introduction:

This appendix describes the design and implementation details of an electronic hand tremor monitoring system to assist in diagnosis and treatment of Parkinson's disease. The system consists of two sub systems- a handheld, wireless-enabled electronic glove and a PC based user interface for data acquisition. The following sections describe each of these subsystems in detail.

B.3.2 Electronic glove:

This sub-system consists of a MEMS based 3-axis accelerometer sensor, a mixed signal system on chip based application board and a 2.4 GHz ISM band Zigbee RF transceiver. All the modules are mounted on an ordinary glove. FigureB.3-1 shows the block diagram of this sub-system.

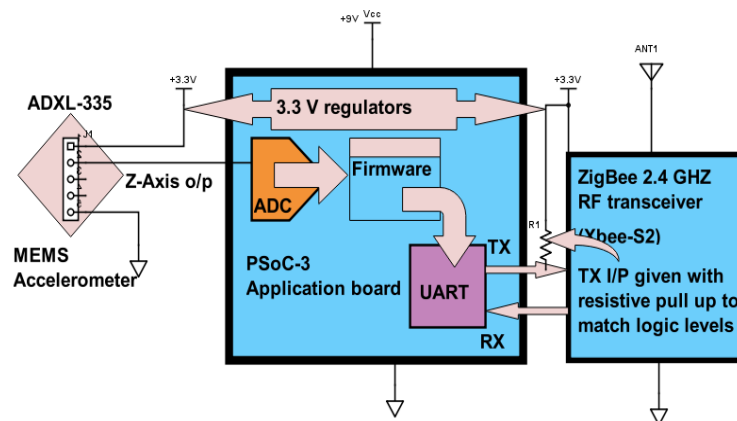


Figure B.3-1 Schematic blocks of the electronic glove

The ADXL-335 is a 3-axis accelerometer which can sense acceleration up to $\pm 3g$ ($g=9.8 \text{ m/s}^2$). This sensor works on a supply voltage of 3.3 V. In this application only a single axis output (Z-axis) of the sensor is used for sensing the vertical vibrations of a single finger. The dynamic voltage range of the sensor output is $\sim 1.5V$ with a 'zero g' voltage

of about 1.5 V. The sensor measures static as well as dynamic acceleration. The analog output corresponding to the Z-axis acceleration is given to the on-chip ADC contained in a Programmable mixed signal system on chip IC (PSoC-3). This IC is mounted on an application board containing all the necessary peripherals like regulators, I/O pins, power supply ports etc. required for any general application. This IC also contains an on-chip UART module which is used by a firmware to communicate the digital data acquired by the ADC to other external modules. The ADC samples the data at a rate of 15 KSPS. The firmware formats the ADC data in a user defined frame and sends it through the on-chip UART to an external wireless module. The delay introduced in formatting and processing in the GUI reduces the final sampling rate in the GUI to 250 SPS. Since the logic levels of the PSoC and the wireless module are different, an open drain output is used in the PSoC pin which converts the 5 volt logic in the PSoC pin to the 3.3 volt logic of the wireless module input pin through a resistive pull up.

The wireless module used here is a 2.4 GHz ZigBee protocol based module from Digi-international® (Xbee-S2®). This module works on a single 3.3 V power supply. The module is used here in a point-to-point configuration and hence can communicate with another single ZigBee transceiver in its periphery (~40m). This module in effect replaces a wired serial connection to a PC with a wireless connection. The serial communication configuration of the UART as well as the ZigBee wireless module is as given below.

Baud rate	: 9600 BPS
Data bits	: 8
Parity	: none
Stop bits	: 1
Flow control	: none

The electronic glove module is powered from a single 9V source. Other supply levels for the sub modules are derived from this 9V source. The total current consumption for the electronic glove module is 70 mA.

photographs of the glove based subsystem is shown below.

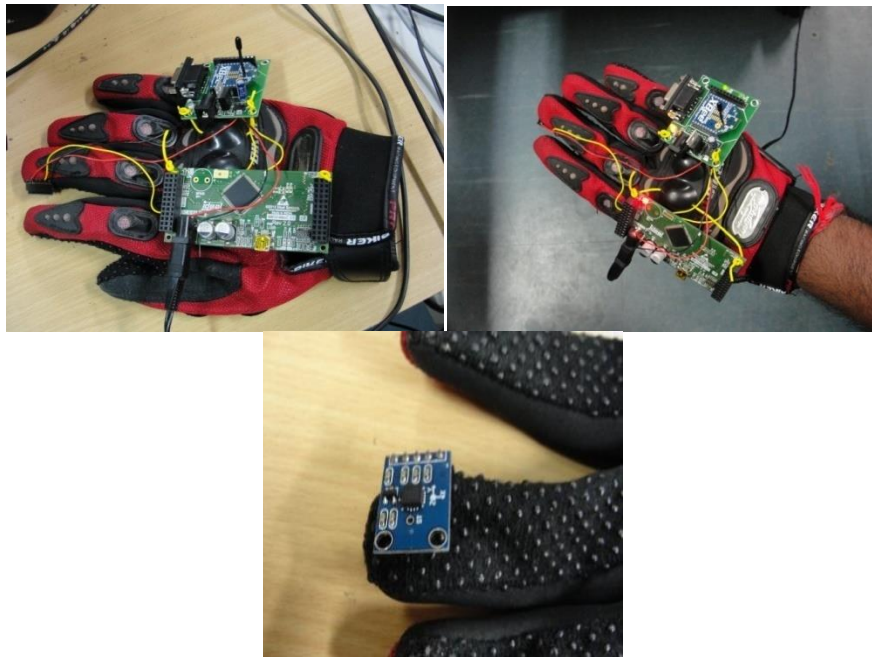


Figure B.3-2 Photograph of the handheld subsystem with the sensor mounting on the finger shown

B.3.3 PC- interface:

The interface to the PC is done through the RS-232 port. The data from the handheld glove is received through another ZigBee wireless module connected to the PC. This module demodulates and converts the data from RF to UART format. The logic level of the ZigBee module is 3.3V which does not match with the logic levels of PC RS-232 port ($\pm 12V$) logic. Hence a logic level converter module is used in between using the MAX-232 converter IC. FigureB.3-3 shows the schematic blocks of the PC sub system.

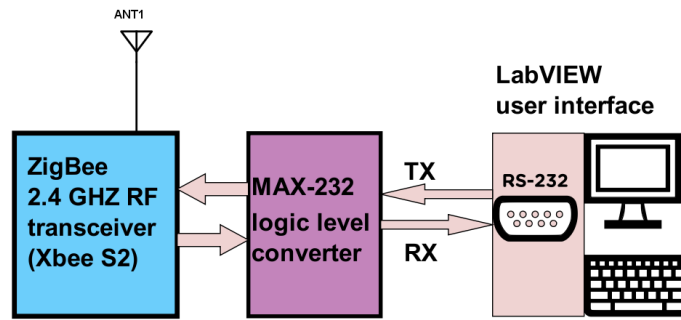


Figure B.3-3 Schematic of the PC based module

The formatted serial data received through the R232 are fed to a LabVIEW based user interface for display, analysis and file storage. The LabVIEW GUI screen shot is shown below.

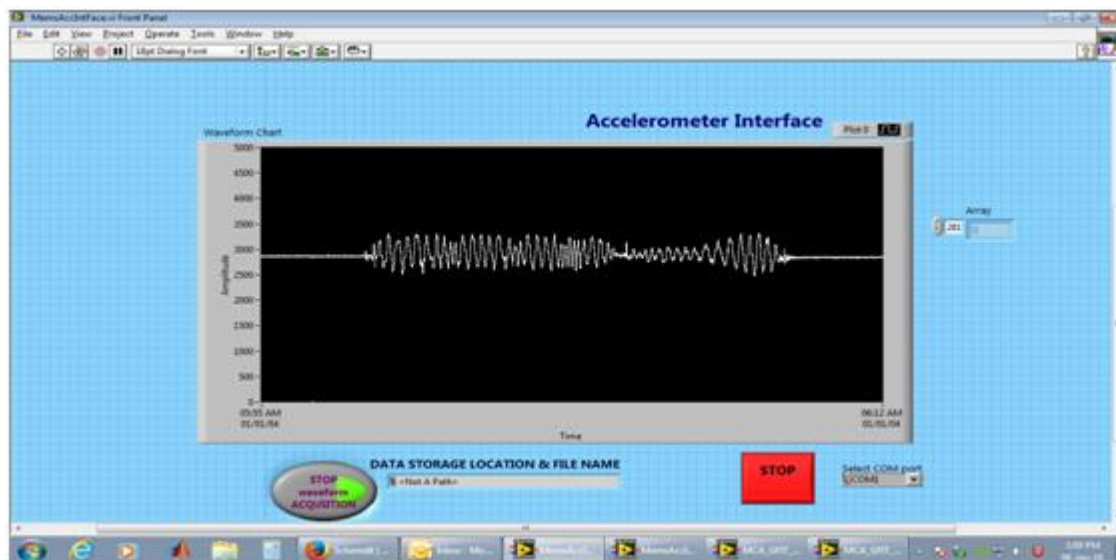


Figure B.3-4 LabVIEW GUI screen shot

The GUI implemented in the PC was found to accurately reproduce minute hand movements of the user with the provision of post analysis of waveform data. The electronic wireless hand tremor monitoring system was successfully designed, implemented and tested using a glove based module.

Bibliography

1. Wehe, D.K., *Current trends in ionizing radiation detection*. Nuclear Engineering and Technology, 2006. **38**(4): p. 311.
2. Tali, M., *Portable Front-End Readout System for Radiation Detection*. 2015.
3. Parnell, K. and R. Bryner, *Comparing and contrasting FPGA and microprocessor system design and development*. White Paper, XILINX Corporation, 2004.
4. Hidvégi, A., *FPGA-based Instrumentation for Advanced Physics Experiments*. 2011.
5. Li, Q.M. *A low-cost configurable PWM controller using programmable system-on-chip*. in *Power Electronics Specialist Conference, 2003. PESC'03. 2003 IEEE 34th Annual*. 2003. IEEE.
6. Hall, T.S. and J.O. Hamblen, *Using system-on-a-programmable-chip technology to design embedded systems*. 2006.
7. Doboli, A., P. Kane, and D. Van Ess. *Dynamic reconfiguration in a PSoC device*. in *Field-Programmable Technology, 2009. FPT 2009. International Conference on*. 2009. IEEE.
8. Sangiovanni-Vincentelli, A. and G. Martin, *Platform-based design and software design methodology for embedded systems*. IEEE Design & Test of Computers, 2001. **18**(6): p. 23-33.
9. Keutzer, K., et al., *System-level design: orthogonalization of concerns and platform-based design*. IEEE transactions on computer-aided design of integrated circuits and systems, 2000. **19**(12): p. 1523-1543.
10. Chakraborty, S., S. Künzli, and L. Thiele. *A General Framework for Analysing System Properties in Platform-Based Embedded System Designs*. in *DATE*. 2003. Citeseer.
11. Becker, E.M., *The MiniSpec: a low-cost, compact, FPGA-based gamma spectrometer for mobile applications*. 2013.
12. Lewellen, T.K., et al., *A Building Block for Nuclear Medicine Imaging Systems Data Acquisition*. Nuclear Science, IEEE Transactions on, 2014. **61**(1): p. 79-87.
13. Ahmad, I., et al., *Nuclear spectroscopy with Si PIN diode detectors at room temperature*. Nuclear Instruments and Methods in Physics Research Section A: Accelerators, Spectrometers, Detectors and Associated Equipment, 1990. **299**(1): p. 201-204.
14. Jach, T. and P. Cowan, *PIN diodes as detectors in the energy region 500 eV–10 keV*. Nuclear Instruments and Methods in Physics Research, 1983. **208**(1): p. 423-425.
15. Salewski, F. and S. Kowalewski, *Hardware platform design decisions in embedded systems: a systematic teaching approach*. ACM SIGBED Review, 2007. **4**(1): p. 27-35.
16. Salewski, F., D. Wilking, and S. Kowalewski, *Diverse hardware platforms in embedded systems lab courses: A way to teach the differences*. ACM SIGBED Review, 2005. **2**(4): p. 70-74.
17. Cypress Semiconductor. *PSoC® 5LP* 2015 [cited 2015 27 Jul]; Available from: <http://www.cypress.com/products/psoc-5lp>.
18. Densmore, D., *Platform Based Reconfigurable Architecture Exploration via Boolean Constraints*. 2004, Department of Electrical Engineering and Computer Sciences, University of California at Berkeley.
19. Lakshmanan, S.K., *Towards Dynamically Reconfigurable Mixed-Signal Electronics for Embedded and Intelligent Sensor Systems*. Kaiserslautern: Technische Universität Kaiserslautern, 2008.
20. Watanabe, T., *A computational analysis of intrinsic detection efficiencies of Geiger–Mueller tubes for photons*. Nuclear Instruments and Methods in Physics Research Section A: Accelerators, Spectrometers, Detectors and Associated Equipment, 1999. **438**(2): p. 439-446.

21. Gooda, P. and W. Gilboy, *High resolution alpha spectroscopy with low cost photodiodes*. Nuclear Instruments and Methods in Physics Research Section A: Accelerators, Spectrometers, Detectors and Associated Equipment, 1987. **255**(1): p. 222-224.
22. Ramírez-Jiménez, F., L. Mondragón-Contreras, and P. Cruz-Estrada. *Application of PIN diodes in Physics Research*. in *Particles and Fields: X Mexican Workshop on Particles and Fields Part B(AIP Conference Proceedings Series)*. 2006.
23. McGregor, D., et al., *Microstructured semiconductor neutron detectors*. Nuclear Instruments and Methods in Physics Research Section A: Accelerators, Spectrometers, Detectors and Associated Equipment, 2009. **608**(1): p. 125-131.
24. McGregor, D.S., S.L. Bellinger, and J.K. Shultis, *Present status of microstructured semiconductor neutron detectors*. Journal of Crystal Growth, 2013. **379**: p. 99-110.
25. Bellinger, S., et al. *High efficiency dual-integrated stacked microstructured solid-state neutron detectors*. in *Nuclear Science Symposium Conference Record (NSS/MIC), 2010 IEEE*. 2010. IEEE.
26. Bellinger, S.L., et al., *High-efficiency microstructured semiconductor neutron detectors that are arrayed, dual-integrated, and stacked*. Applied Radiation and Isotopes, 2012. **70**(7): p. 1121-1124.
27. Solomon, C., J. Shultis, and D. McGregor, *Reduced efficiency variation in perforated neutron detectors with sinusoidal trench design*. Nuclear Instruments and Methods in Physics Research Section A: Accelerators, Spectrometers, Detectors and Associated Equipment, 2010. **618**(1): p. 260-265.
28. McGregor, D.S., et al., *Design considerations for thin film coated semiconductor thermal neutron detectors—I: basics regarding alpha particle emitting neutron reactive films*. Nuclear Instruments and Methods in Physics Research Section A: Accelerators, Spectrometers, Detectors and Associated Equipment, 2003. **500**(1): p. 272-308.
29. McGregor, D.S., et al. *Designs for thin-film-coated semiconductor thermal neutron detectors*. in *Nuclear Science Symposium Conference Record (2001 IEEE)*. 2001.
30. McGregor, D.S., et al. *Recent results from thin-film-coated semiconductor neutron detectors*. in *International Symposium on Optical Science and Technology*. 2003. International Society for Optics and Photonics.
31. L'Annunziata, M.F., *Radioactivity: introduction and history*. 2007: Elsevier.
32. Knoll, G.F., *Radiation detection and measurement*. 2010: John Wiley & Sons.
33. Howell, W., et al., *A historical review of portable health physics instruments and their use in radiation protection programs at Hanford, 1944 through 1988*. 1989, Pacific Northwest Lab., Richland, WA (USA).
34. Kemmer, J., *Fabrication of low noise silicon radiation detectors by the planar process*. Nuclear Instruments and Methods, 1980. **169**(3): p. 499-502.
35. Kemmer, J., *Improvement of detector fabrication by the planar process*. Nuclear Instruments and Methods in Physics Research Section A: Accelerators, Spectrometers, Detectors and Associated Equipment, 1984. **226**(1): p. 89-93.
36. Mishra, V., *Study of silicon detectors*. 2002, PhD thesis (Mumbai University).
37. Bjerke, H., et al., *Radiation survey meters used for environmental monitoring*. 2012, Nordisk Kernesikkerhedsforskning.
38. *Ludlum Model 2242 operations manual*. 2005 [cited 2012 May 12]; Available from: www.drct.com/dss/.../Ludlum/Ludlum_Manuals/Ludlum-Model-2242-manual.pdf.
39. *WB Johnson DSM-500 manual*. 2012 [cited 2012 may 12]; Available from: www.drct.com/images/Survey_meters/DSM-500_SURVEY_METER-manual.pdf.
40. *PRSM-1 manual*. 2011 [cited 2012 May 12]; Available from: www.eeipl.in/DataSheets/PRSM1_Datasheet.pdf.
41. Kwak, S.-W., et al., *Development of a portable α -particle spectrometer*. Journal of Instrumentation, 2015. **10**(06): p. C06013.

42. Cheng, Y., et al., *Development of the portable alpha-ray spectrometer based on the PIPS detector*. Nuclear Electronics and Detection Technology, 2011. **31**(4): p. 444-446, 450.
43. Sánchez, A.M. and J. de la Torre Pérez, *Portable alpha spectrometer*. Applied Radiation and Isotopes, 2012. **70**(9): p. 2267-2269.
44. Drndarević, V., *A very low-cost alpha-particle spectrometer*. Measurement Science and Technology, 2008. **19**(5): p. 057001.
45. Selwood, M. and S. Monk, *Evolution of a neutron detector for the purpose of portability and resolvability*. Nuclear Instruments and Methods in Physics Research Section A: Accelerators, Spectrometers, Detectors and Associated Equipment, 2012. **680**: p. 18-26.
46. Oakes, T.M., et al., *An accurate and portable solid state neutron rem meter*. Nuclear Instruments and Methods in Physics Research Section A: Accelerators, Spectrometers, Detectors and Associated Equipment, 2013. **719**: p. 6-12.
47. Cho, A., *Helium-3 shortage could put freeze on low-temperature research*. Science, 2009. **326**(5954): p. 778-779.
48. Kouzes, R.T., *The 3He supply problem*. 2009, Pacific Northwest National Laboratory (PNNL), Richland, WA (US).
49. Bellinger, S.L., *Advanced microstructured semiconductor neutron detectors: design, fabrication, and performance*. 2011, Kansas State University.
50. Wall, B., et al., *Dead layer on silicon p-i-n diode charged-particle detectors*. Nuclear Instruments and Methods in Physics Research Section A: Accelerators, Spectrometers, Detectors and Associated Equipment, 2014. **744**: p. 73-79.
51. Meric, I., et al., *Enhancement of the intrinsic gamma-ray stopping efficiency of Geiger-Müller counters*. Nuclear Instruments and Methods in Physics Research Section A: Accelerators, Spectrometers, Detectors and Associated Equipment, 2012. **696**: p. 46-54.
52. RAJAN, G. and J. IZEWSKA, *Radiation Monitoring Instruments*. Podgorsak EB, Radiation Oncology Physics: a Handbook for teachers and students. Vienna: International Atomic Energy Agency (IAEA), 2005.
53. Kumar, D.K. and N. Kotnana, *Design and implementation of portable health monitoring system using PSoC mixed signal array chip*. International Journal of Recent Technology and Engineering (IJRTE), 2012. **1**(3): p. 59-65.
54. Lynch, B.T. *Under the hood of a DC/DC boost converter*. in *TI Power Supply Design Seminar, Dallas, TX, USA*. 2008.
55. Ghazali, A., T. Ahmad, and N. Abdullah. *Characterization of a pulsed mode high voltage power supply for nuclear detectors*. in *IOP Conference Series: Earth and Environmental Science*. 2013. IOP Publishing.
56. Raviraj, V. and P.C. Sen, *Comparative study of proportional-integral, sliding mode, and fuzzy logic controllers for power converters*. IEEE Transactions on Industry Applications, 1997. **33**(2): p. 518-524.
57. Jisha, N., et al., *Development of autonomous gamma dose logger for environmental monitoring*. Review of Scientific Instruments, 2012. **83**(3): p. 035112.
58. Ess, D.V. *Approximating an Opamp with a Switched Capacitor Integrator* 2011 [cited 2012 11 Dec 2012]; Available from: <http://www.cypress.com/file/37256/download>.
59. Pease, R.A. *The design of band-gap reference circuits: trials and tribulations*. in *Bipolar Circuits and Technology Meeting, 1990., Proceedings of the 1990*. 1990. IEEE.
60. Centronic. *Geiger Muller Tubes*. [cited 2012 may 2012]; Available from: http://qa.ff.up.pt/radioquimica/Bibliografia/Diversos/geiger_tube_theory.pdf.
61. Lee, J., I. Kim, and H. Choi, *On the dead time problem of a GM counter*. Applied Radiation and Isotopes, 2009. **67**(6): p. 1094-1098.
62. Cypress Semiconductor. *PSoC Designer 5.4 IDE*. 14 Mar 2016 [cited 2014 1 May 2014]; Available from: <http://www.cypress.com/products/psoc-designer>.

63. Turner, J.E., *Atoms, radiation, and radiation protection*. Atoms, Radiation, and Radiation Protection, 2nd Edition, by James E. Turner, pp. 576. ISBN 0-471-59581-0. Wiley-VCH, April 1995., 1995: p. 576.
64. Bøtter-Jensen, L. and P.H. Jensen, *Determination of scattered gamma radiation in the calibration of environmental dose rate meters*. Radiation protection dosimetry, 1992. **42**(4): p. 291-299.
65. Laurus Systems Inc. *DRM Radiation Area Monitors* 18 Feb 2016 [cited 2013 29 Nov 2013]; Available from: <http://www.laurussystems.com/DRM-Radiation-Area-Monitoring-Systems.htm>.
66. Mazur Instruments. *PRM-9000 Specifications*. 15 Dec 2015 [cited 2013 29 Nov 2013]; Available from: http://www.mazurinstruments.com/PRM-9000_detail.html.
67. Im, J.-P., et al., *A 40 mV transformer-reuse self-startup boost converter with MPPT control for thermoelectric energy harvesting*. IEEE Journal of Solid-State Circuits, 2012. **47**(12): p. 3055-3067.
68. Carlson, E.J., K. Strunz, and B.P. Otis, *A 20 mV input boost converter with efficient digital control for thermoelectric energy harvesting*. IEEE Journal of Solid-State Circuits, 2010. **45**(4): p. 741-750.
69. Goldader, J.D. and S. Choi, *An Inexpensive Cosmic Ray Detector for the Classroom*. The Physics Teacher, 2010. **48**(9): p. 594-597.
70. Wibig, T., et al., *Educational studies of cosmic rays with a telescope of Geiger–Müller counters*. Physics education, 2006. **41**(6): p. 542.
71. Rahman, M.M. and M.A. Istiaq. *Variable HVDC supply using fly back transformer with several protective features to the output power BJT/MOSFET*. in *Electrical Engineering and Informatics (ICEEI), 2011 International Conference on*. 2011. IEEE.
72. Islam, M.N., K. Asaduzzaman, and M. Hoq, *Design and Development of a Microcontroller Based Nuclear Counting System*. Journal of Engineering and Applied Sciences, 2012. **7**(3): p. 246-248.
73. Spieler, H., *Semiconductor detector systems*. Vol. 12. 2005: Oxford university press.
74. Rao, D., V. Sudheendran, and P. Sarkar, *Optimization of parameters of alpha spectrometry with silicon detector for low level measurements of actinides in environmental samples*. Applied Radiation and Isotopes, 2012. **70**(8): p. 1519-1525.
75. Prasanna, G. and J. Jayapandian, *An embedded read-out for GM counter*. International Journal of Instrumentation Technology, 2014. **1**(3): p. 228-240.
76. Kumar, R., et al. *High voltage power supply development for INGA facility at IUAC*. in *Proceedings of the DAE symposium on nuclear physics*. V. 52. 2007.
77. García-Toraño, E., *Current status of alpha-particle spectrometry*. Applied radiation and isotopes, 2006. **64**(10): p. 1273-1280.
78. Nakhostin, M., et al., *Use of commercial operational amplifiers in a low cost multi-channel preamplifier system*. Radiation Physics and Chemistry, 2013. **85**: p. 18-22.
79. Asensio, L., et al., *Evaluation of a low-cost commercial mosfet as radiation dosimeter*. Sensors and Actuators A: Physical, 2006. **125**(2): p. 288-295.
80. Födisch, P., et al., *Charge-Sensitive Front-End Electronics with Operational Amplifiers for CdZnTe Detectors*. arXiv preprint arXiv:1603.05098, 2016.
81. Takahashi, T., et al., *High-resolution Schottky CdTe diode detector*. Nuclear Science, IEEE Transactions on, 2002. **49**(3): p. 1297-1303.
82. Cerizza, A., A. Fazzi, and V. Varoli. *Performances of operational amplifiers in front-end electronics for nuclear radiation detectors*. in *Nuclear Science Symposium Conference Record, 2004 IEEE*. 2004. IEEE.
83. Fagionato, E.A., F.A. Genezini, and G.S. Zahn, *Development of a charge-sensitive preamplifier using commercially available componentes*. 2013.

84. Texas Instruments. *OPA656 Wideband, Unity-Gain Stable, FET-Input Operational Amplifier*. 2015 Sep 2015 [cited 2016 10 Apr 2016]; Available from: <http://www.ti.com/lit/ds/symlink/opa656.pdf>.
85. Ortec. *Introduction to amplifiers*. 5 Feb 2016 [cited 2016 5 Feb 2016]; Available from: www.ortec-online.com/download/amplifier-introduction.pdf.
86. Scoullar, P.A. and R.J. Evans. *Maximum Likelihood Estimation Techniques for High Rate, High Throughput Digital Pulse Processing*. in *Proceedings of the IEEE Nuclear Science Symposium and Medical Imaging Conference and 16th International Workshop on Room-Temperature Semiconductor X-ray and Gamma-ray Detectors*. 2008.
87. Landis, D., et al., *Pulsed Feedback Techniques for Semiconductor Detector Radiation Spectrometers*. Nuclear Science, IEEE Transactions on, 1971. **18**(1): p. 115-124.
88. Kandiah, K., A. Smith, and G. White, *A pulse processor for X-ray spectrometry with Si (Li)-detectors*. Nuclear Science, IEEE Transactions on, 1975. **22**(5): p. 2058-2065.
89. Landis, D.A., *Energy-dependent losses in pulsed-feedback preamplifiers*. Lawrence Berkeley National Laboratory, 1979.
90. Landis, D., et al., *Transistor reset preamplifier for high rate high resolution spectroscopy*. Nuclear Science, IEEE Transactions on, 1982. **29**(1): p. 619-624.
91. Britton, C., et al., *Characteristics of high-rate energy spectroscopy systems using HPGe coaxial detectors and time-variant filters*. Nuclear Science, IEEE Transactions on, 1984. **31**(1): p. 455-460.
92. Texas Instruments. *MAX 4594 SPST analog switch datasheet*. 6 Jan 2016 [cited 2016 6 Jan 2016]; Available from: <http://www.ti.com/lit/ds/symlink/max4594.pdf>.
93. Ahmad, I., et al., *Nuclear spectroscopy with Si PIN diode detectors at room temperature*. Nuclear Instruments and Methods in Physics Research Section A: Accelerators, Spectrometers, Detectors and Associated Equipment, 1990. **299**(1): p. 201-204.
94. Ashokkumar, P., et al., *An improved silicon PIN diode based portable radon monitor*. Indian Journal of Physics, 2013. **87**(5): p. 471-477.
95. Mimura, M., et al., *Ultraviolet-sensitive windowless silicon PIN photodiodes for alpha-ray spectrometry*. Japanese Journal of Applied Physics, 2008. **47**(3R): p. 1740.
96. Warren, G.H. and C. Jungo. *Noise, crosstalk and distortion in mixed analog/digital integrated circuits*. in *Custom Integrated Circuits Conference, 1988., Proceedings of the IEEE 1988*. 1988. IEEE.
97. Warburton, W., et al., *Digital pulse processing: New possibilities in portable electronics*. Journal of Radioanalytical and Nuclear Chemistry, 2001. **248**(2): p. 301-307.
98. Shultis, J. and D. McGregor, *Design and performance considerations for perforated semiconductor thermal-neutron detectors*. Nuclear Instruments and Methods in Physics Research Section A: Accelerators, Spectrometers, Detectors and Associated Equipment, 2009. **606**(3): p. 608-636.
99. Guardiola Salmerón, C. and L. Fantoba, *Novel silicon sensors for neutron detection*. 2013.
100. Guardiola, C., et al., *Geant4 and MCNPX simulations of thermal neutron detection with planar silicon detectors*. Journal of Instrumentation, 2011. **6**(09): p. T09001.
101. TableCurve 2D. [cited 2014 10 August]; Available from: <http://www.sigmaplot.co.uk/products/tablecurve2d/tablecurve2d.php>.
102. Raman, S., et al., *Thermal-neutron capture by silicon isotopes*. Physical Review C, 1992. **46**(3): p. 972.
103. Hardell, R. and A. Hasselgren, *Thermal neutron capture in ¹⁹F*. Nuclear Physics A, 1969. **123**(1): p. 215-224.
104. Shultis, J. and D. McGregor, *Calculation of ion energy-deposition spectra in silicon, lithium-fluoride, boron, and boron carbide*. Engineering Experiment Station Kansas State University, 2004(299).

105. Shultis, J. and D. McGregor, *Calculation of ion energy-deposition spectra in silicon, lithium-fluoride, boron, and boron carbide*. Kansas State University, Engineering Experiment Station, 2004. **299**.
106. Barclay, D., *Improved response of geiger muller detectors*. IEEE Transactions on Nuclear Science, 1986. **33**(1): p. 613-616.
107. Storm, E., D.W. Lier, and H.I. Israel, *Photon sources for instrument calibration*. Health physics, 1974. **26**(2): p. 179-189.
108. Shao, Q., et al., *High aspect ratio composite structures with 48.5% thermal neutron detection efficiency*. Applied Physics Letters, 2013. **102**(6): p. 063505.
109. Li, Y. and Q. Xu, *A totally decoupled piezo-driven XYZ flexure parallel micropositioning stage for micro/nanomanipulation*. IEEE Transactions on Automation Science and Engineering, 2011. **8**(2): p. 265-279.
110. Gollakota, A. and M. Srinivas. *Agribot—a multipurpose agricultural robot*. in *India Conference (INDICON), 2011 Annual IEEE*. 2011. IEEE.
111. Sivakumar, N., et al., *Development of an ion mobility spectrometer for detection of explosives*. Instrumentation Science & Technology, 2013. **41**(1): p. 96-108.